Optical Links for the ATLAS Pixel Detector

Ingrid-Maria Gregor

Juli 2001
WUB DIS 2001–03

FACHBEREICH PHYSIK
BERGISCHE UNIVERSITÄT
WUPPERTAL

Optical Links for the ATLAS Pixel Detector

Ingrid-Maria Gregor

This work was supported by the German Ministerium für Bildung, Wissenschaft, Forschung und Technologie (BMBF) under contract No. 05 HA8PXA/2 and by the Ministerium für Schule, Wissenschaft und Forschung (MSWF) des Landes Nordrhein–Westfalen under contract no. IV A5-10601798.

Diese Arbeit wurde unterstützt durch das Bundesministerium für Bildung, Wissenschaft, Forschung und Technologie (BMBF) unter der Fördernummer 05 HA8PXA/2 und durch das Ministerium für Schule, Wissenschaft und Forschung (MSWF) des Landes Nordrhein–Westfalen unter der Fördernummer IV A5-10601798.

Contents

Überblick

In der vorliegenden Dissertation wird eine strahlentolerante optische Datenstrecke mit hoher Datenrate für den Einsatz in dem Hochenergiephysikexperiment ATLAS am LHC Beschleuniger entwickelt. Da die LHC-Experimente extremen Strahlenbelastungen ausgesetzt sind, müssen die Komponenten spezielle Ansprüche hinsichtlich der Strahlentoleranz erfüllen. Die Qualifikation der einzelnen Bauteile wurde im Rahmen dieser Arbeit durchgeführt.

Die zu erwartenden Fluenzen im ATLAS Inner Detector für Silizium und Gallium Arsenid (GaAs) wurden berechnet. Siliziumbauteile werden einer Fluenz von bis zu $1.1{\cdot}10^{15}\mathrm{n}_{eq}/\mathrm{cm}^2$ in 1 MeV äquivalenten Neutronen ausgesetzt sein, wohingegen GaAs Bauteile bis zu $7.8{\cdot}10^{15}\mathrm{n}_{eq}/\mathrm{cm}^2$ ausgesetzt sein werden.

Die Strahlentoleranz der einzelnen benötigten Komponenten wie z.B. der Laserdioden sowie der jeweiligen Treiberchips wurde untersucht. Sowohl die Photo- als auch die Laserdioden haben sich als strahlentolerant für die Fluenzen an dem vorgesehenen Radius erwiesen. Aus den Tests der Treiberelektronik ließ sich eine Empfehlung für den Neudesign der Schaltungen in einer 0.25 μm Technologie ableiten. Aufgrund der geometrischen und umgebungsbedingten Anforderungen müssen die optoelektronischen Elemente in ein spezielles Gehäuse mit direkter Faserankopplung integriert werden. Nach der Qualifizierung dreier verschiedener Kandidaten für dieses Gehäuse wurde das sogenannte Taiwan-Package ausgewählt.

Eine Studie der Einzelereignisse aufgrund ionisierender Teilchen gab Aufschluß über das Verhalten der optischen Links innerhalb einer Umgebung, wie sie für LHC-Experimente erwartet wird. Fehler werden durch hochenergetische Teilchen in der Photodiode induziert. Es zeigte sich, daß die Anzahl der Fehler pro Zeiteinheit und Datenrate minimiert werden kann, wenn der von dem Lichtsignal erzeugte mittlere Photostrom größer als 65 μA ist.

Aus diesen Ergebnissen folgend, wird eine Integration von sieben optischen Links auf einer speziellen Platine für das entgültigen Design des optischen Links für den ATLAS Pixeldetektor vorgeschlagen.

Chapter 1

Introduction

In order to gain new experimental insight and to enhance the understanding of elementary particle physics at the TeV scale, the European Organisation for Nuclear Research (CERN[1]) approved in 1994 the Large Hadron Collider LHC [1]. This novel collider will mainly run in proton-proton mode with a centre-of-mass energy of 14 TeV and become operational in 2006. The 10^{11} particles per second typically created in this environment bring new challenges for detector design, both in terms of the speed of response and the radiation resistance of the used components required.

The detector systems of the SemiConductor Tracker (SCT) and Pixel Detector in the ATLAS Inner Detector are highly granular to cope with the many charged particles produced on average from every LHC proton–proton collision. Fast data readout from the detectors is one of many important technical issues. The large number of electronic channels makes the use of copper links unfeasible due to the amount of material which would be introduced into the detector volume and problems from cross-talk and ground loops. Optical data transmission is a very attractive technology to employ in these detector systems as it offers very fast transfer rates while needing only small components. It is therefore proposed to use custom optical data links to transmit data from the detector to the acquisition electronics over a distance of up to 100 m. It will also be used to distribute the Timing, Trigger and Control (TTC) data from the counting room to the front-end electronics.

Fibre optics has become the core of our telecommunications and data networking infrastructure. Optical fibre is the preferred means of transmission of any data with rates of a few tens of megabits per second and distances of anything from a meter to many hundreds of kilometres. But the special application of an optical data link in the area of high energy physics makes the use of industrial standard products unfeasible.

The data link has to comply a list of requirements in order to meet the demands of a high energy physics environment: The components of the system must be able to withstand high level of ionising radiation and neutron radiation. The components for the optical data link should be of non-magnetic material to avoid perturbations of the Inner

[1] Conseil Europeénne Pour la Recherche Nucleaire

Detector magnetic field. Additionally, the material must have a low mass to present a small radiation-length to the produced particles.

This thesis is concerned with the design of the optical link for the Pixel Detector of the ATLAS experiment. A part of the studies presented in this report has been performed with the SCT optical link components as pre-studies for the optical link system of the Pixel Detector. Due to much higher fluences within the Pixel Detector and a different readout rate as well as a different geometry a new design of an optical link is required.

After this introduction a short visit to the Higgs physics potential of the ATLAS detector and a summary of the subsystem is given. The innermost Pixel Detector, consisting of hybrid Pixel modules, is described in Chapter 3. An overview of radiation damages in semiconductors such as Silicon (Si) and Gallium Arsenide (GaAs) and the radiation environment expected within the Inner Detector is given in Chapter 4. The components essential for the optical links, the opto-electronic devices and optical fibres, are described in Chapter 5. In Chapter 6 radiation tolerance and accelerated lifetime studies of Vertical Cavity Surface Emitting Lasers (VCSELs) are discussed. Chapter 7 summarises the qualification of three candidate optical packages and the reason for the choice of one of these packages. The electronics required to drive the optical link is described in Chapter 8. Single Event Studies are presented in Chapter 9 along with a discussion of the implications on the performance on the optical link for the Pixel Detector. In Chapter 10 the relevancy of this results for the optical link for the ATLAS Pixel Detector are recapitulated and a possible design is given. A summary of the results and an outlook on future optical links for high energy physics experiments closes this thesis.

Chapter 2

Higgs Physics at LHC and the ATLAS Experiment

At the LHC physicists from all over the world will have the opportunity to invest a variety physics areas including the search for the Higgs boson as most prominent topic. The ATLAS Detector is one of two general purpose 4π detectors necessary to explore the fundamental structure of matter. The requirements for LHC and the discovery potential for the Higgs boson are discussed along with a description of the role of the ATLAS Pixel Detector in Higgs–Physics. An overview of the ATLAS Detector is given at the end of this chapter.

2.1 Physics at LHC

The experiments at the LHC offer a large range of physics opportunities. Major topics are the investigation of the origin of the electroweak symmetry breaking and the search for physics beyond the Standard Model of particle physics. In the last century the present Standard Model (SM) has been defined and proven to be the most exact model particle physicists ever delivered. The Large Electron Positron Collider LEP at CERN has collected enough data in order to test the SM and to make precision measurements of fundamental parameters, but the SM has not been proven inshakably and further aspects of the SM and models beyond the SM must be explored [6]:

- Detailed studies of the physics of B–hadrons and of the CP–violation in the B–hadron system.
- Search for the Standard Model Higgs boson over the full allowed mass from the experimental limit set by LEP (113.5 GeV [7]) and Tevatron up to the theoretical upper bound of 1 TeV. A closer look at the Higgs search will be given in 2.1.2.
- Precise measurements of the W mass, of WWγ and WWZ Triple Gauge Couplings, and of the mass, the couplings and the decay properties of the top quark.
- Several QCD measurements need to be performed, such as running of the strong coupling constant α_s over an unprecedented range of Q^2.

- Search for super symmetry particles (SUSY) and other physics beyond the Standard Model, such as leptoquarks or additional leptons, quarks and gauge bosons.

2.1.1 The Standard Model

The Standard Model (SM) of elementary particle physics describes the elementary structure of matter and its interactions. This theory is based upon a gauge theory; its predictions are in excellent agreement with the precision measurements of the high energy experiments as for example DELPHI at LEP. The SM has become the most important particle physics theory of the 20th century.

In the Standard Model all matter is made of three kinds of elementary particles: fermionic leptons and quarks, and bosonic force mediators. The leptons and quarks are further grouped into three families as shown in Table 2.1. According to the Standard

Family	**Leptons**			**Quarks**		
	Flavour	Charge (e)	Mass (GeV)	Flavour	Charge (e)	Mass (GeV)
1st	ν_e	0	$< 3 \cdot 10^{-9}$	u	2/3	1 to $5{\cdot}10^{-3}$
	e	-1	$511{\cdot}10^{-6}$	d	$-1/3$	3 to $9{\cdot}10^{-3}$
2nd	ν_μ	0	$< 0.19 \cdot 10^{-3}$	c	2/3	1.15 to 1.35
	μ	-1	$105.6{\cdot}10^{-3}$	s	$-1/3$	75 to 170 $\cdot 10^{-3}$
3rd	ν_τ	0	$< 18.2 \cdot 10^{-3}$	t	2/3	174.3±5.1
	τ	-1	1.777	b	$-1/3$	4.0 to 4.4

Table 2.1: *The elementary fermions (spin 1/2) in the Standard Model, with their charge and mass [8].*

Model of physics, the fundamental forces comprise of the gravitational force, the electromagnetic force, the strong force and the weak force. Each interaction type has its mediator: the photon for the electromagnetic force, two W's and a Z for the weak force, the graviton (presumably) for gravity and gluons for the strong force. Table 2.2 lists the relevant parameters of the fundamental force interactions, not including the gravity. A complete

Interaction	Strength	Boson	Charge (e)	Mass (GeV)
Electromagnetic	$\alpha = 1/137$	γ	0	0
Weak	$\alpha_w \sim 1/29$	$W^{\pm}$	± 1	80.419 ± 0.056
		Z	0	91.1882 ± 0.0022
Strong	$\alpha_s \sim 0.1...1$	8 gluons	0	0

Table 2.2: *Interactions and the corresponding gauge bosons in the Standard Model. The strength of each interaction can be parameterised by its dimensionless coupling constant [8].*

quantum theory of gravity has yet to be clearly detailed. At present, it is assumed that gravity is too weak to play a significant role in elementary particle physics [9].

On another front, two forces previously thought to be distinct, the electromagnetic and the weak force, are now described as a single electroweak theory. The electroweak theory was derived from efforts to produce a theory for the weak force analogous to quantum electrodynamics (QED), the quantum theory of the electromagnetic force. The weak force fails to meet a requirement for that theory: it does not behave the same way at different points in space and time, it acts only across distances smaller than an atomic nucleus. Nevertheless it was shown that the electromagnetic force, which can extend across interstellar distances, and the weak force are only different manifestations of a more fundamental force, the electroweak force. This made it possible to formulate a unified model that predicted the existence of mediating, or messenger, particles. The electroweak theory, for which Sheldon Glashow, Abdus Salam, and Steven Weinberg shared the 1979 Nobel Prize in Physics, was confirmed in 1983 by the discovery of the W and Z particles, two of a number of elementary particles it predicted.

The mass of the weak mediators is another question to be solved; this mass was not forseen in the Standard Model (SM). P.W. Higgs et. al [10] delivered in 1964 a way to solve the Lagrangian with massive gauge bosons.

2.1.2 The Search for the Higgs Boson

In the SM the electroweak force is described by a gauge theory. The presence of a mass term violates the $SU(2) \times U(1)$ gauge invariance of the theory, therefore massless gauge bosons are required. The mass term $M^2 A_\mu A^\mu$ is not invariant under $A_\mu \rightarrow A_\mu - \delta_\mu \kappa$, therefore M^2 must be zero. The Higgs mechanism avoids this dilemma by starting with a theory having massless gauge bosons and ending with a spectrum of massive gauge bosons, using an algebraic transformation. In the following example the simple Abelian case is described:
The existence of a complex scalar boson ϕ and a massless gauge boson A_μ is assumed. Additionally, the form of the Lagrangian is assumed to be:

$$\mathcal{L} = (D_\mu \phi)^\star (D^\mu \phi) + \mu^2 \phi^\star \phi - \lambda (\phi^\star \phi)^2 - \frac{1}{4} F^{\mu\nu} F_{\mu\nu} \tag{2.1}$$

The parameters are constrained by $\lambda > 0$ (to assure that the potential is bounded from below) and $\mu^2 > 0$. $F^{\mu\nu}$ is the anti-symmetric tensor of the gauge boson field, $F^{\mu\nu} = \partial^\mu A^\nu - \partial^\nu A^\mu$. Under local gauge transformation

$$\phi \rightarrow \phi\prime = e^{ig\kappa(x)} \phi \tag{2.2}$$

$$A^\mu \rightarrow A'^\mu = A^\mu - \partial^\mu \kappa(x) \tag{2.3}$$

the invariance of the theory is guaranteed if in the Lagrangian the covariant derivative $D^\mu = \partial^\mu + igA^\mu$ is used instead of the ordinary derivative ∂^μ. The potential for the scalar field has its minimum value at $\phi = v/\sqrt{2} = \sqrt{\mu^2/2\lambda}$ (Figure 2.1). It is appropriate to expand ϕ around its minimum to find the spectrum of the theory, thus

$$\phi = [\nu + h(x)]/\sqrt{2}, \tag{2.4}$$

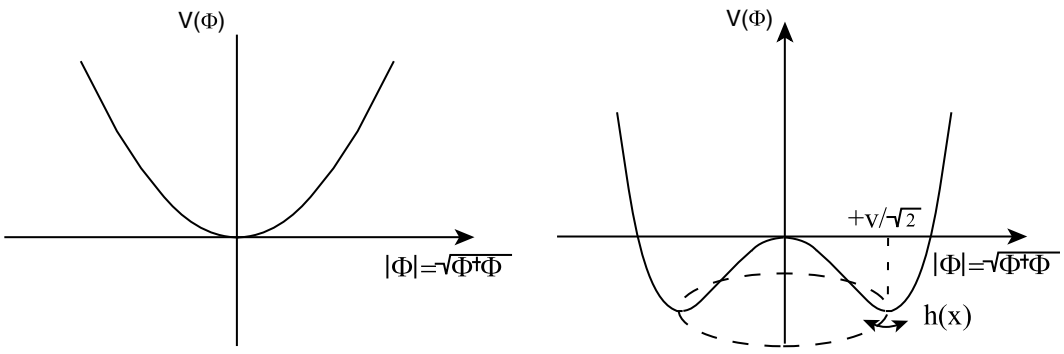

Figure 2.1: *The potential for the scalar field has the minimum value at* $\phi = v/\sqrt{2} = \sqrt{\mu^2/2\lambda}$.

where h(x) is the real field. Substituting this into the Lagrangian $\mathcal{L}$, we explicitly have

$$\begin{aligned}\mathcal{L} &= \frac{1}{2}[(\partial_\mu - igA_\mu)(\nu + h)(\partial_\mu + igA^\mu)(\nu + h)] \\ &\quad + \frac{1}{2}\mu^2(\nu + h)^2 - \frac{1}{4}\lambda(\nu + h)^4 - \frac{1}{4}F^{\mu\nu}F_{\mu\nu} \end{aligned} \tag{2.5}$$

This contains several important terms:

$(\frac{g^2\nu^2}{2})A_\mu A^\mu$	should be interpreted as the mass for the gauge boson,
$-\lambda\nu^2h^2$	is a mass term for the scalar boson, and
h^3,h^4,hAA	are interaction terms, with related strength.

Using this transformation, the theory with a complex scalar boson and a massless gauge boson was reinterpreted as a theory with a real scalar boson H and a massive gauge boson Z. This is because the scalar potential had its minimum at a value ϕ which is non-zero (spontaneaus symmetry breaking). This method of giving mass to the gauge boson is called the SM Higgs mechanism [11, 12].

From the propagator of the Higgs boson quadratic divergences arise due to loop corrections. In SUSY theories, a new symmetry is introduced which assigns a super-symmetric boson to each fundamental fermion (squarks, sleptons), and a super-symmetric fermion to each boson (photino, gluino, etc.). So divergences in bosonic and fermionic loop corrections can cancel each other in a natural way. SUSY theories have several attractive features, including the possibility of unifying fermions and bosons and the fact that local SUSY requires the existence of gravity. A strong indication for the realisation of this picture in nature is the excellent agreement between the theoretical value of the electroweak mixing angle $\sin^2\theta_W = 0.2336\pm0.0017$ and 0.2316 ± 0.0003 from experiments; the difference between two values being only 1% [13].

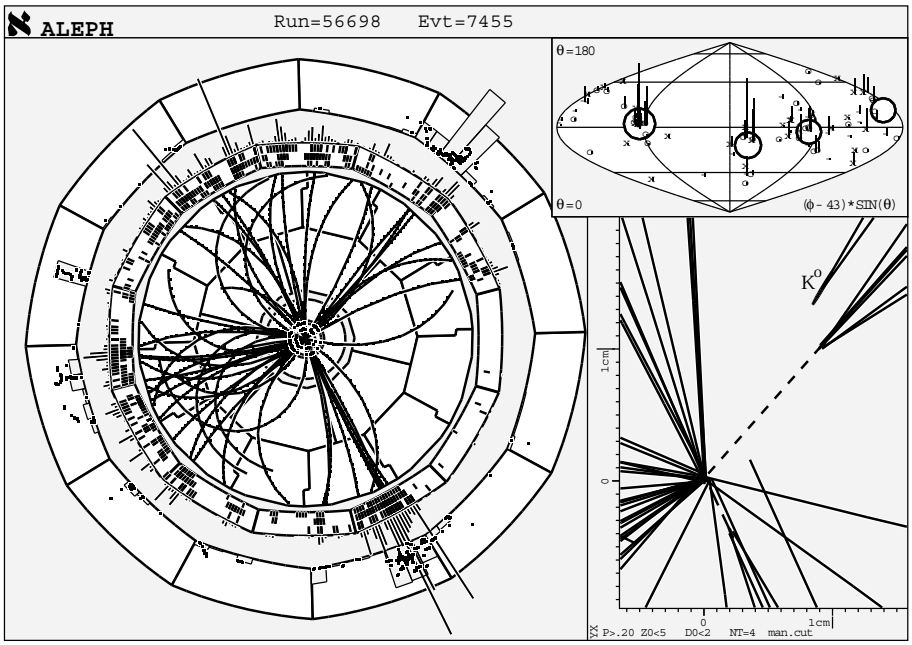

Figure 2.2: *Four-jet Higgs boson candidate with a reconstructed Higgs boson mass of 110.0 GeV/c^2. Three of the four jets are well b–tagged. The event is shown in the view transverse to the beam direction, the $\theta - \phi \sin\theta$ view, and in a closeup of the charged particles in the vertex region of the* ALEPH *Detector [14].*

In the Minimal Supersymmetric Standard Model (MSSM) there are two free parameters, and five physical Higgs bosons; namely two charged (H^+,H^-), a light (h) and a heavier scalar particle (H), and a neutral pseudo-scalar particle (A). According to the predictions of MSSM, the lightest supersymmetric particles should be stable and have a mass below $\sim$ 1 TeV. To date, the Higgs theory is the only theory, giving an explanation for massive gauge bosons, which is in good agreement with all experiments. However, the Higgs boson has yet to be discovered.

In the year 2000, the last year of LEP2, some LEP experiments detected signals indicating a possible Higgs boson discovery. At a centre-of-mass energy above 206.5 GeV, and with a very large signal-to-noise ratio of 4.7, a first event compatible with HZ production at $m_H = 115$ GeV/c^2 was detected in the four-jet channel [15]. Of the four LEP experiments ALEPH has "seen" the largest signal, L3 the second largest, followed by OPAL. The data collected by DELPHI is fully compatible with the background [16]. One of the reconstructed ALEPH events is shown in Figure 2.2.

In addition the precision electroweak data of the past several years have been suggesting that the Higgs boson mass is very close to the present experimental limit of 113.5 GeV/c^2 [16]. The data taken by DELPHI at 200-209 GeV is for all channels compatible with **expectations from the SM background. In combination with Delphi data from pre-**

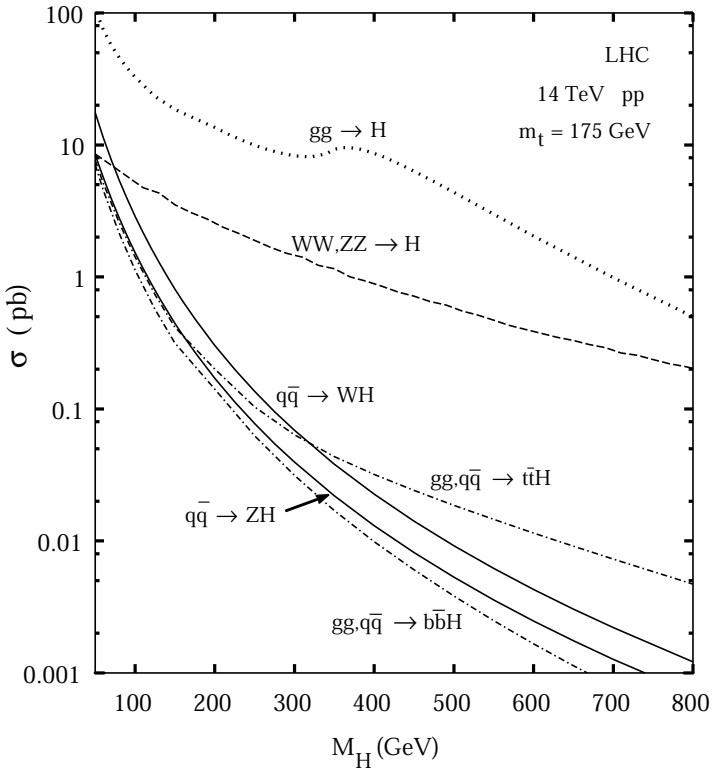

Figure 2.3: *Expected production cross–section for a SM Higgs boson at* LHC *[17].*

vious runs, a lower limit at 95% confidence level on the mass of the SM Higgs boson is set at 114.3 GeV. A new analysis of the forward-backward asymmetry showed a smaller asymmetry than expected. This results in a bigger SM Higgs than is currently assumed [18].

Assuming that the LEP data indicate a Higgs with a mass of 115 GeV, what would be the consequence?
Firstly and most importantly, it would confirm the Standard Model, but it would also indicate evidence for new physics beyond the SM. The reason for this is the shape of the effective Higgs potential, which is determined by the Higgs coupling λ_H. This is subject to renormalisation[1] by the top-quark Yukawa coupling λ_t, as well as by the Higgs coupling λ_H itself. With $m_t \sim 175$ GeV and $m_H \sim 115$ GeV, the renormalisation by λ_t is stronger. Moreover, it tends to decrease λ_H, eventually turning it negative at a scale of $l10^6$ GeV [19]. This results in the effective Higgs potential being unbounded from below, implying that the present electroweak vacuum is unstable – unless there is some new physics introduced at an energy below 10^6 GeV. Therefore, a Higgs of this mass cannot be a SM Higgs. Furthermore, a light Higgs boson, as suggested by LEP is a strong indication for supersymmetry. The

[1] renormalisation is the procedure in quantum field theory by which divergent parts of a calculation, leading to nonphysical infinite results, are canceled leading to a redifinition of couplings and masses which become dependent of the renormalisation scale

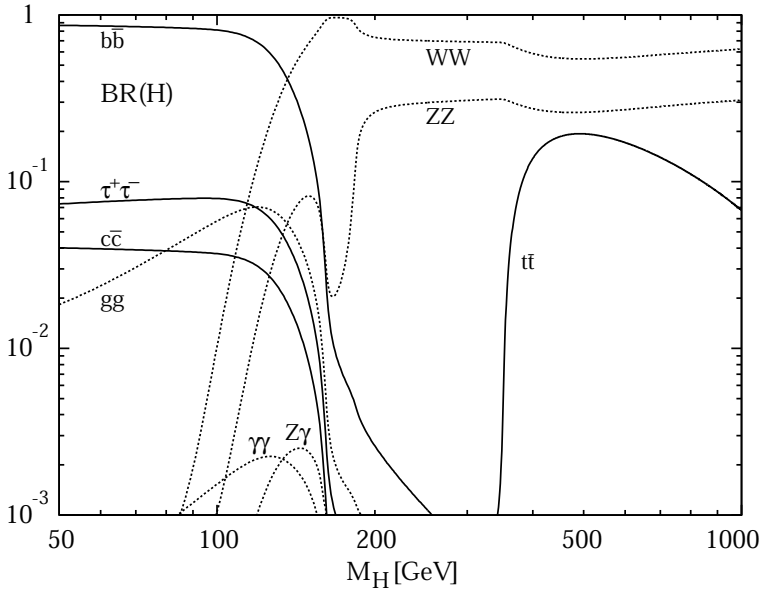

Figure 2.4: *Branching ratios for the decays of a Standard Model Higgs boson into fermions as a function of the Higgs boson mass [17].*

destabilising effects of λ_t are counterbalanced by the stop squarks. In the MSSM, the lightest neutral Higgs boson h is predicted to have a mass of $\leq$ 130 GeV [20].

The following gives an overview of the LHC potential to find the SM Higgs boson in the lower mass region. It can be produced in a variety of processes at the LHC. The machine has sufficient energy to excite heavy quanta, and since the Higgs boson couples to other particles proportional to their mass, this leads to efficient Higgs production modes. For all possible Higgs masses, the main production mechanism will be the gluon fusion process. Other processes such as vector boson fusion are also of interest because of the special signature they can provide for identification of the Higgs. Figure 2.3 shows the expected cross sections of the various production processes as a function of the SM Higgs mass [17].

With the Higgs decaying directly into pairs of all massive particles and through loop diagrams into pairs of massless gluons and photons, the field of Higgs physics is large. The main channels which will be used at the LHC to search for a SM Higgs boson (Figure 2.4), can be classified as follows [6]:

- Low mass region ($m_H \leq$130 GeV): This mass region and the possible Higgs decay channels are discussed below.
- Intermediate mass region (130 GeV $\leq m_H \leq 2m_Z$): The most promising channels for the experimental searches are H $\rightarrow$WW*$\rightarrow l\nu l\nu$ and H$\rightarrow$ZZ*$\rightarrow 4l$.
- High mass region ($m_H \geq 2m_Z$). This is the best mass region to discover a Higgs boson at LHC since the $H \rightarrow ZZ \rightarrow 4l$ channel gives rise to a gold-plated signature: almost no background. For very large masses ($m_H \geq 500\,GeV$), searches for this decay mode

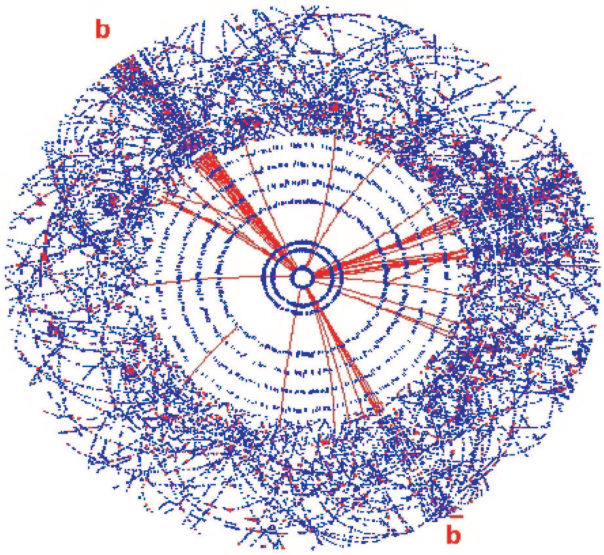

Figure 2.5: $H \to b\bar{b}$ *event in the* ATLAS *detector [4].*

$H \to WW \to l\nu jj$, which have larger branching ratios and therefore can compensate for the decrease in the production cross section.

Higgs Search in the Low Mass Region $m_H \leq$130GeV

Two decay modes are experimentally important in this region, $H \to b\bar{b}$, $H \to \gamma\gamma$.
$H \to b\bar{b}$**:**
A possible $H \to b\bar{b}$ event in the ATLAS detector is depicted in Figure 2.5. This decay mode has a branching ratio of $\geq 90\%$ in most of this mass region, and therefore inclusive Higgs production followed by $H \to b\bar{b}$ has a large cross-section ($\sim$ 20 pb). However since this signal can not be efficiently triggered and the signal-to-background ratio for the inclusive production is less than 10^{-5}, it would be impossible to observe this channel above the QCD background [6]. Associated production $t\bar{t}H$, WH, ZH, with $H \to b\bar{b}$ and with an additional lepton coming from the decay of the accompanying particles, has a much smaller cross section (≤ 1 pb) but gives rise to final states, which allow additional tagging options, and can be extracted from the background. It is triggered by an isolated high-p_t lepton from leptonic decay of the associated boson or semi-leptonic decay of the associated top quark. The background for these channels is quite large. Part of the background is reducible from W+jet or $t\bar{t}$ production with cross section an order of magnitude larger than the signal cross section. Additionally, there is a difficult resonant background from the WZ production. Table 2.3 lists the cross sections for the example of m_H =100 GeV, as simulated for reference [5]. The WH and $t\bar{t}H$ channels are discussed in detail because the ZH contribution does not significantly improve the signal-to background ratio with respect to the WH channel, since it has a similar background level, but a lower production rate [21]. The ATLAS strategy

Final state: $l\nu b\bar{b} + X$	σ**(pb)**
WH ($m_H = 100$ GeV)	0.40
WZ	0.86
$Wb\bar{b}$	70
$t\bar{t}$	247
$W^* \rightarrow tb$	1.4
$qg \rightarrow tbq$	45
Wjj two jets with $p_T > 15$ GeV, $\eta \leq 3.2$	4640
Final state: $l\nu jjb\bar{b}b\bar{b} + X$	
$t\bar{t}H$ ($m_H = 100$ GeV)	0.29
$t\bar{t}Z$	0.02

Table 2.3: *Cross-sections times branching ratios for WH and $t\bar{t}H$ production (m_H =100 GeV) and for various background processes [5].*

to trigger these events is based on some features of the event topology which are common for the WH and the $t\bar{t}H$ channels:

- One trigger lepton with a transverse momentum $p_T > 20$ GeV (electron) or $p_T > 6$ GeV (muon) in the pseudo-rapidity range[2] $|\eta| < 2.5$.
- Jets from $H \rightarrow b\bar{b}$ decay with $p_T > 15$ GeV and $|\eta| < 2.5$.

The latter requires an excellent b-tagging capability. Jets originating from a b-quark must be efficiently discriminated from u-,d-,s-,c-quarks and gluon jets. The method, called b-tagging, is based either on the long lifetime of the b-quark which causes secondary vertices or on the high amount of leptons in B-meson decays. In b-tagging methods the stand alone performance of the precision is important. The sub-detectors with the highest granularity, such as the ATLAS Pixel Detector, are expected to play a major role in pattern recognition inside high-p_T jets. The final state topology and the different background sources for the WH and the $t\bar{t}H$ channel impose different final selection criteria for each one of the two channels.

- WH channel: Extensive simulations [5] show that the extraction of a signal from the $H \rightarrow b\bar{b}$ decay in the WH channel will be very difficult at the LHC. It has a irreducible background from $WZ \rightarrow l\nu b\bar{b}$ and $Wb\bar{b}$ production. The reducible background originates from events with at least two b-quarks in the final state and with jets misidentified as b-jets.

  With further selection criteria the trigger is extended for this decay channel: a lepton veto, i.e. no additional high p_T lepton, a jet veto, i.e. no additional high p_T jet, and an invariant $2\sigma_m$ mass cut on the tagged b-jets around the nominal Higgs mass. In the case of $m_H = 100$ GeV (30 fb^{-1}) and an b-tagging efficiency ϵ_b of 60% the signal

[2] the pseudo-rapidity η is defined as $\eta = -\ln(\tan\theta/2)$ where θ is the polar angle of the produced particle with respect to the beam line

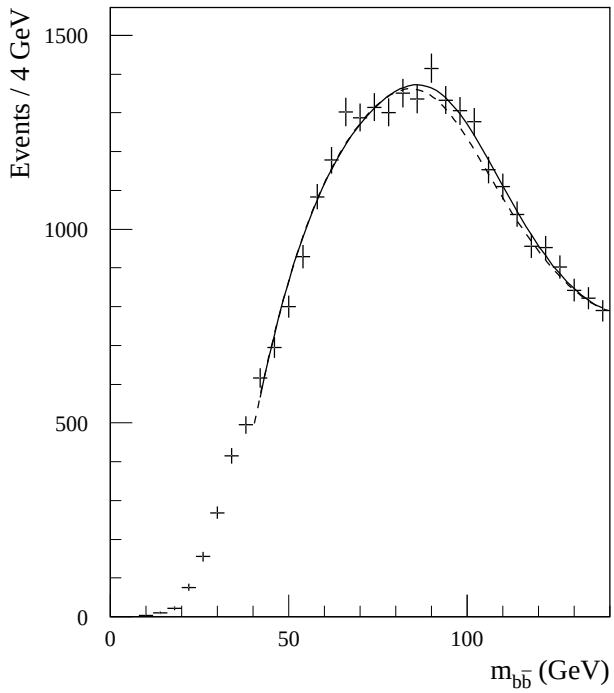

Figure 2.6: *Expected WH signal with $H \rightarrow b\bar{b}$ above the summed background for m_H = 100 GeV and for an integrated luminosity of 30 fb^{-1}. The dashed line represents the shape of the background [5].*

significance $\frac{S}{\sqrt{B}}$ is 3.3*. For m_H =120 GeV this is reduced to 2.4 [21]. An example of the expected $H \rightarrow b\bar{b}$ signal is shown in Figure 2.6 for m_H = 100 GeV. The difficulty in extracting a resonant signal from the $b\bar{b}$ pairs is well illustrated here.

- $t\bar{t}H$ channel: The extraction of the $t\bar{t}H$, $H \rightarrow b\bar{b}$ channel appears to be feasible due to the more complex final state (2Ws and 4 b-jets). The irreducible background is due to $t\bar{t}Z$ production and the continuum $t\bar{t}b\bar{b}$ production. The reducible background is due to jets misidentified as b-jets.

  In this channel the request of at least six high p_T jets and of exactly four tagged b-jets is added to the trigger. By fully reconstructing the top quark, the combinatorial background in the invariant Higgs mass evaluation is reduced. With small changes this method can be used at high luminosity as well. Considering an integrated luminosity of 100 fb^{-1}, the signal significance $\frac{S}{\sqrt{B}}$ is 6.4 for m_H =100 GeV and 3.9 for m_H =120 GeV (with ϵ_b = 50%). The invariant mass distribution of the signal over the integrated background in Figure 2.7 shows the signal visibility.

*S is the number of signal events and B the number of background events

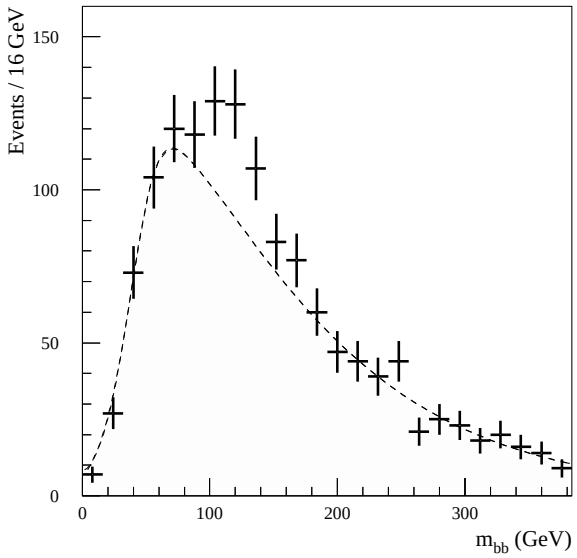

Figure 2.7: *Invariant mass distribution $m_{b\bar{b}}$ of tagged b-jet pairs in fully reconstructed $t\bar{t}H$ signal events with a Higgs-boson mass of 120 GeV above the summed background for an integrated luminosity of 100 fb^{-1} [5].*

$H \to \gamma\gamma$:
This channel has a branching ratio in the order of 10^{-3} and therefore a small cross-section ($\sim$50 fb)[†], but this channel is more accessible than the $b\bar{b}$ channel because of the better signal-to-background ratio ($\sim 10^{-2}$). The final state consists of two high-p_T photons with invariant mass that is compatible with the Higgs mass. The detection of this decay mode requires excellent mass resolution, superior photon identification, and reconstruction efficiency with an excellent rejection power against jets. This is the most challenging channel for the performance of the electromagnetic calorimeters and has driven the design and technology for these ATLAS subdetectors. The reason for these requirements is the background of two other reactions: direct $\gamma\gamma$ production and γj and jj production, where one or both jets fake a photon. By definition the $\gamma\gamma$ irreducible background can not be reduced. Since the Higgs width is only a few MeV in this low mass region, it would appear as a narrow resonant peak in the $\gamma\gamma$ invariant distribution [17]. Direct production and associated production (WH,ZH and $t\bar{t}H$) with the decay $H \to \gamma\gamma$ were studied to evaluate their significance [5, 23]. For a Higgs mass of 120 GeV, the expected significances $\frac{S}{\sqrt{B}}$ are 6.5 for direct production, 4.3 for associated production, where W,Z, $t\bar{t} \to leptons + X$, and 5.2 for $H + jet$ production. Figure 2.8 depicts the $\gamma\gamma$ invariant mass distribution for $H \to \gamma\gamma$ signal and background before and after background subtraction.

In conclusion, we conclude that for a Higgs boson in the low mass region the ATLAS discovery potential relies on the $t\bar{t}H$ ($H \to b\bar{b}$) channel, and thus the b-tagging abilities of the ATLAS Inner Detector are crucial.

[†] $H\gamma\gamma$ is forbidden at tree level and therefore $H \to \gamma\gamma$ decay occurs through top quark or W loops

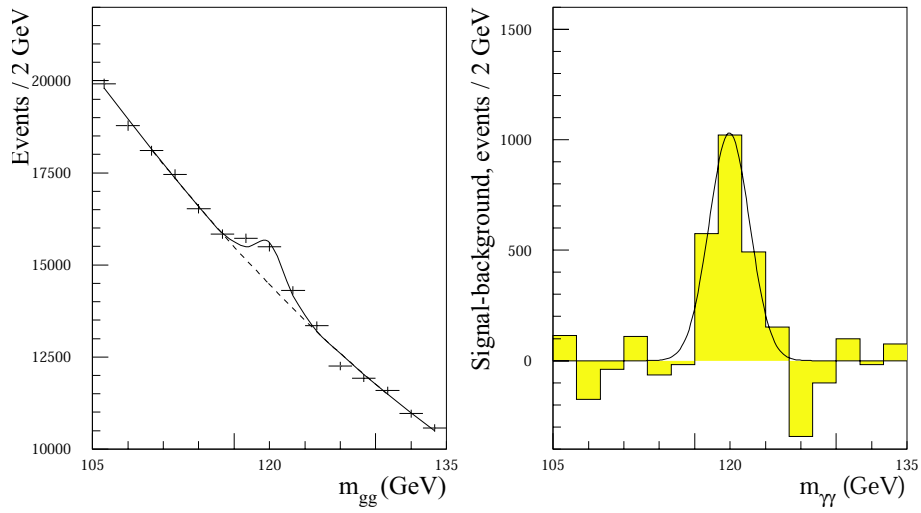

Figure 2.8: *$\gamma\gamma$ invariant mass distribution for the $H \rightarrow \gamma\gamma$ signal and background before (left) and after (right) background subtraction [5].*

2.1.3 Requirements for LHC

The above discussion of the possible physics performance shows that there are strong reasons to expect very compelling physics at the TeV energy scale. To produce quark and gluon interactions at the TeV energy scale, the centre-of-mass energy in a hadron collider must be considerably higher than 1 TeV, as in a hadron each of the constituent quarks and gluons carries only a fraction of the hadron´s momentum. In order to compete with other experiments, the reaction rate R must be high. R depends on the cross section σ of all processes and the collider parameters. It is given by

$$R = \sigma \cdot \mathcal{L} \tag{2.6}$$

where the *luminosity*, $\mathcal{L}$ is defined as

$$\mathcal{L} = B \cdot \frac{n_1 n_2 f}{A} \tag{2.7}$$

with

	n_1, n_2	particle number in both bunches,
	B	number of bunches per beam,
	A	cross section of colliding bunches,
	f	circulation frequency.

The de-Broglie–wavelength decreases with increasing energy with $\frac{1}{E}$ and therefore the cross section is reduced by $\frac{1}{E^2}$. Thus, it is necessary to have high luminosity to achieve acceptable reaction rates of physically intersting processes. The Large–Hadron–Collider LHC at CERN is presently under construction. This new accelerator will be located in the existing LEP tunnel and will provide pp collisions and heavy–ion (e.g. Pb–Pb) collisions [1].

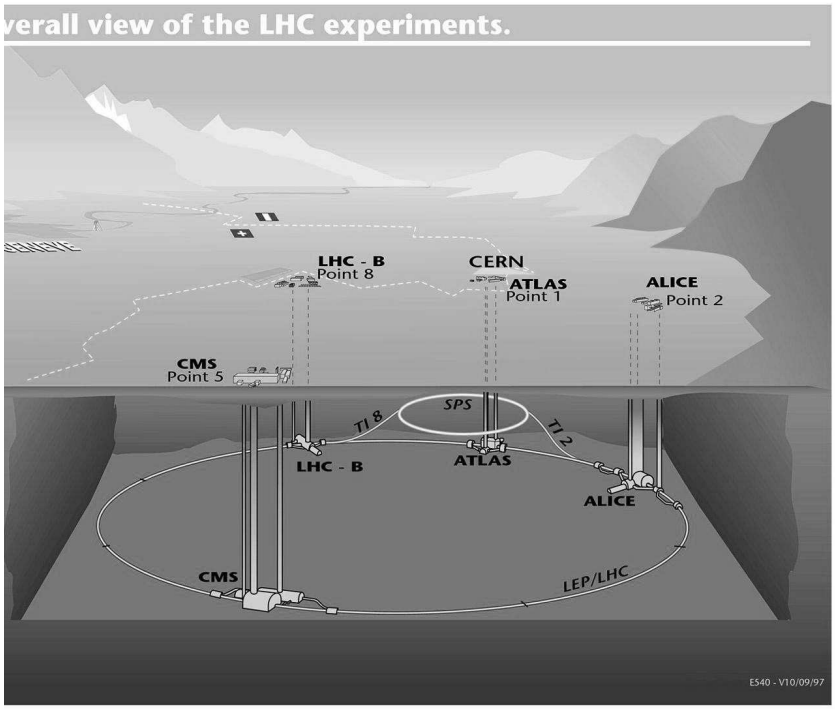

Figure 2.9: *The upcoming* LHC *experiment at CERN [1].*

When running in proton–proton mode, the centre of mass energy will be $\sqrt{s} = 14$ TeV and the design luminosity $10^{34}\text{cm}^{-2}\text{s}^{-1}$. With its unprecedented performance this will open the window to a yet unexplored range of particle physics. LHC is at the end of an acceleration chain. This chain consists of four steps, starting with a linear accelerator which gives the protons an energy of 50 MeV. They are further accelerated by the PS Booster, the proton synchrotron and the super proton synchrotron. Before the protons are injected into the LHC they reach an energy of 450 GeV. The accelerator structure ties the particles up into bunches. 2835 of these bunches will circle in the LHC for a couple of hours. At four interaction points these bunches are focused. Every 25 ns a collision of bunches will occur and the particle processes will be monitored by the experiments. The LHC accelerator with its experiments is illustrated in Figure 2.9.

LHC at CERN will be working at an energy of an order of magnitude above the energy of Tevatron (Fermi–Lab) and two orders above LEP. During the first three years with low luminosity, LHC runs with a number of particles per bunch $N = 0.17 \times 10^{11}$, which gives a luminosity of $L_{low} = 1 \times 10^{33}\text{cm}^{-2}s^{-1}$. The accelerator is also able to run at a higher luminosity, where the number of particles per bunch will be increased up to $N = 1.67 \times 10^{11}$ and resulting in a luminosity of $L_{high} = 1 \times 10^{34}\text{cm}^{-2}s^{-1}$. More details about the machine can be found in [1].

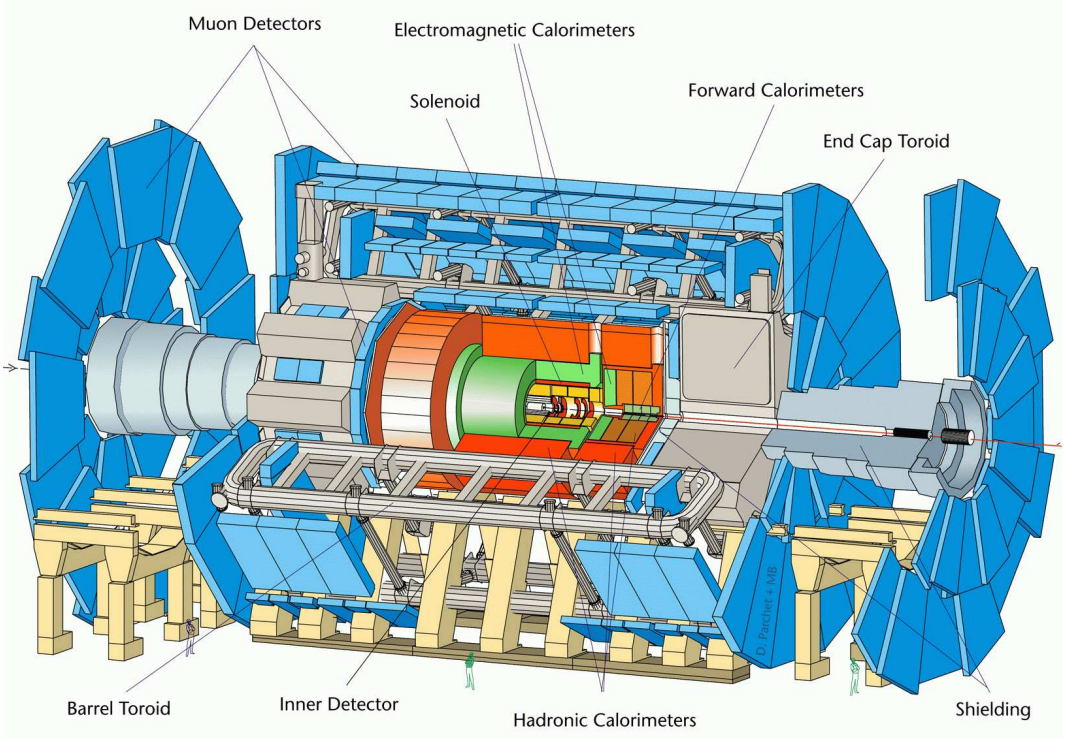

Figure 2.10: *The* ATLAS *Detector [3]*

2.2 The ATLAS Detector

The basic design considerations for the ATLAS detector are motivated by the goal to exploit the full LHC physics potential as partly described above. The detector is optimised simultaneously for a range of many known and hypothetical processes. The ATLAS detector will have a total length of 44 m, a height of 22 m and a weight of 7000 tons. Several subsystems are arranged cylindrically around the beam axis; additional disks of each subsystem facilitate a better coverage of the forward and backward area at large pseudo-rapidity. Figure 2.10 gives an overall view of the ATLAS detector.

2.2.1 Magnets

The configuration of the magnet system used for the momentum measurements greatly influences on how well the performance goals can be met. ATLAS uses two different magnet systems: the superconducting solenoid for the Inner Detector (in front of the electromagnetic calorimeter) and large superconducting air-core toroid outside the calorimeter. This solution has the advantage of almost not constraining the calorimetry and the Inner Detector while providing a high resolution, large acceptance, and a robust stand-alone muon spectrometer. The superconducting solenoid with a magnetic field of 2T is integrated into the cryostat of the liquid argon barrel calorimeter. The total thickness of the solenoid

amounts to 0.67 radiation lengths [24]. The design aims to minimise the material in front of the calorimeter, different from most other detector designs where the magnet is placed outside the EM calorimeter. The advantage of this design is its compactness. Additionally the small magnetic field in the EM calorimeter also reduces the transverse spread of showers. The disadvantage is, that a lot of material is inserted in front of the calorimeter and therfore a high percentage of the particles start to shower before they reach the calorimeter. The magnetic field along the z-direction drops from 2T at the interaction point to around 0.5T at the end of the Inner Detector.

The superconducting air core toroid provides the magnetic field for the muon spectrometer. It consists of a large barrel toroid and two end-cap toroids, each formed of eight coils. With a toroidal field, particles will cross the complete pseudo-rapidity range, almost perpendicular to the field. This means that the field integral $\int Bdl$, which is an important factor for the momentum resolution, can be kept high even in the forward direction.

2.2.2 Muon System

The identification of leptons is important for an experiment working at a high energy proton-proton collider as described above. The ATLAS muon system serves a double purpose: as a trigger to select events with high energy muons and as a precision muon spectrometer. The muon chambers are mounted in three layers at the outside of the ATLAS Detector.

The concept of the muon spectrometer aims for an excellent momentum resolution over all pseudo-rapidities, taking advantage of the open air core geometry of the toroids. Each chamber has an intrinsic resolution of ~ 60 μm. The two multilayers of detectors provide a track segment as well. The muon trigger is based on a separate set of trigger chambers, which are also used for the bunch crossing identification and measurement.

Monitoring Drift chambers (MDT) are used for the precision measurements covering most of the acceptance. They are supplemented by Cathode Strip Chambers (CSC) in the very forward region. With the muon spectrometer, the pseudorapidity range up to $|\eta| = 3$ is covered and a momentum resolution of $\sim 10\%$ at $p_T = 1$ TeV is achieved. At $p_T = 100$ GeV the momentum resolution is $\sim 2\%$. Triggering capability is provided up to $|\eta| = 2.2$ for various muon p_T thresholds between about 6 GeV and 35 GeV.

2.2.3 Calorimeter System

The main task of the calorimeter system is the precise measurement of the energy and (to a lesser extent) the direction of single particles and jets. It is divided into two subsystems, the electromagnetic and the hadronic calorimeter. These are sampling calorimeters, combining an active medium and a passive absorption material. Most parts of the calorimeter use liquid argon as the active medium because of its intrinsic radiation hardness. The whole system is located inside the muon spectrometer in a 11 m long support cylinder with a diameter of 8.5 m. It consists of several liquid argon (LAr) calorimeters surrounded by a large hadronic scintillating tile calorimeter. In the barrel a cryostat around the Inner Detector cavity encloses, at its innermost radius, the coil of the ID solenoid, followed by

a LAr pre-sampling layer (which is needed to recover the energy lost in the material in front of the calorimeter), and by an electromagnetic LAr accordion calorimeter. Each end-cap consists of an electromagnetic LAr accordion calorimeter, a hadronic end-cap LAr calorimeter and a forward LAr calorimeter.

The electromagnetic calorimeter absorbs of electrons and photons using accordion shaped lead sheets. Liquid argon between these absorption sheets serves as sensitive detector material. The secondary particles originating from the lead are used for the energy determination. The electromagnetic calorimeter has three longitudinal samplings and a transverse segmentation of about 0.025×0.025 in $\delta\eta \times \delta\phi$ over most of the pseudo-rapidity coverage. The design resolution of the EM cal is $10\%/\sqrt{E/GeV} \oplus 0.7\%$.

The hadronic scintillating tile calorimeter is based on iron absorbers with scintillating plates read out by wavelength shifting fibres in three longitudinal samplings with a transverse granularity of $\delta\eta \times \delta\phi = 0.1 \times 0.1$. This part covers the pseudorapidity range up to $|\eta|$=1.6. In the region from $|\eta|$=1.6 to 3.2 the calorimeter is complemented by an end-cap LAr calorimeter using parallel copper plates as the absorber. The dense forward calorimeter, covering $3.2 < |\eta| < 4.9$, is made of copper and tungsten as absorbers, providing both, electromagnetic and a hadronic calorimeter. The design resolution for the jet and missing E_T calorimetry is $50\%/\sqrt{E/GeV} \oplus 3\%$ for $|\eta| < 3$, and $100\%/\sqrt{E/GeV} \oplus 10\%$ for $3 < |\eta| < 5$ [5].

2.2.4 The Inner Detector

Close to the interaction point is the Inner Detector (ID), composed of three types of tracking systems: the Pixel Detector, the SemiConductor Tracker (SCT), and the Transition Radiation Tracker (TRT). The expected event rate is 23 interactions every 25 ns bunch crossing for a luminosity of $10^{34}\text{cm}^{-2}\text{s}^{-1}$ [22]. To facilitate momentum measurements of charged particles, the Inner Detector is immersed in a 2T magnetic field which runs axially along the proton beam direction. Due to the high bunch crossing frequency, it is essential that the detectors run with fast front-end electronics and fast signal processing. The Pixel Detector assists in measurering the vertex, where three points in space for each particle track are needed; the radius R, the azimuthal angle ϕ, and the pseudo-rapidity η. The Pixel Detector is essential for the tracking of short living particles as the B–mesons. A more detailed description of the Pixel Detector is given in Chapter 3.

The SCT is made of silicon modules which are mounted on a four-layer barrel with nine disks on either side for the end-cap coverage. There are 2112 identical barrel modules for a total detector area of 34 m^2 and 1976 forward modules for a total detector area of 27 m^2. The total number of channels is, thus $6.2 \cdot 10^6$. Each module is made of two single-sided strip detectors rotated by 40 mrad with respect to each other, in order to provide a measurement of the dimension along the strips – z in the barrel and R in the forward region. The SCT is designed to fulfill the following requirements:

- Four space-points up to a pseudo-rapidity of 2.5 and three points in the forward area.
- Small angle stereo to avoid ambiguities.
- A resolution capability of 20 μm in each detector.

- Better than 1 mm effective z resolution of space-point.
- Two-hit resolution on the order of 200 μm.
- Detectors of at least 97% efficiency.
- All layers fully operational for the lifetime of LHC.

All four barrel layers are built from identical modules, each consisting of two pairs of identical detectors mounted back-to-back on a VHCPG[3] baseplate, and with a hybrid holding the FE chips and control-logic. The individual silicon wafers are cut to be 64 mm long by 63.6 mm wide and have n-implanted read-out strips at a pitch of 80 μm. Two detectors are daisy-chained together for each side of a module to give a total length of approximaltely 13 cm. The detectors consist of high resistivity reverse biased diodes.

The detectors for the forward modules are shaped like a sector of a pie, i.e. vary in size with distance from the beam line, and range from approximately 7 cm $\times$ 5 cm to 12 cm $\times$ 6 cm. The SCT readout electronics are purely binary and provide no pulse height information beyond the 0/1 answer with respect to a threshold. The threshold is common for each 128-channel chip, but the offset is corrected individually. The $R\phi$ resolution of the SCT is around 22 μm in the barrel and 24 μm in the forward. The SCT uses bi–directional optical links for the data transfer, similar to the Pixel Detector (Chapter 3.4).

Both semiconductor trackers are supplemented by the TRT, which is composed of wire chambers (straws) in order to give a measurement of R and Φ. By measuring the transition radiation, is also possible to identify electrons.

The TRT is designed using straws of 4 mm diameter. The gas mixture filling these straws is 70% Xenon, 20% CF4, and 10% CO_2. The barrel part extends from 56 to 107 cm in radius. The $\sim$ 50000 straws for the barrel are laid along the z direction and their length is 2 $\times$ 74 cm, with readout of the separated halves at both ends. The $\sim$ 320000 straws in the end-cap TRT disks are radial, extending from R = 64 to 103 cm. The straws are surrounded by materials in which the electrons produce transition radiation (TR). The TR photons will then be absorbed and produce large signals on the straws. The TRT readout electronics provides two thresholds, a lower threshold for detecting signal from ionisation in gas and a higher threshold for detecting the TR. The electronics will also give the Time over Threshold (ToT) for the lower threshold. This additional information has been shown to help in particle identification [25]. The occupancy of the TRT at the high luminosity can reach almost 40% in the innermost parts, whereas it does not exceed 10 to 15% in the rest of the system. The TRT electronics will also measure drift time to improve the spatial resolution. This measurement is affected if the straw is crossed by two tracks. A strong point of the TRT, is the large amount of hits on the individual tracks. While the silicon detectors provide in average seven space points on a track with 10-30 μm precision in the $R\phi$ coordinate, the TRT gives above 35 hits with a resolution from 170 μm to 240 μm per hit.

The impact parameter resolution of the Inner Detector has to be high to enable good b-tagging performance. The B-Layer was added to the Inner Detector in order to alow

[3] very high thermal conductivity pyrolytic graphite

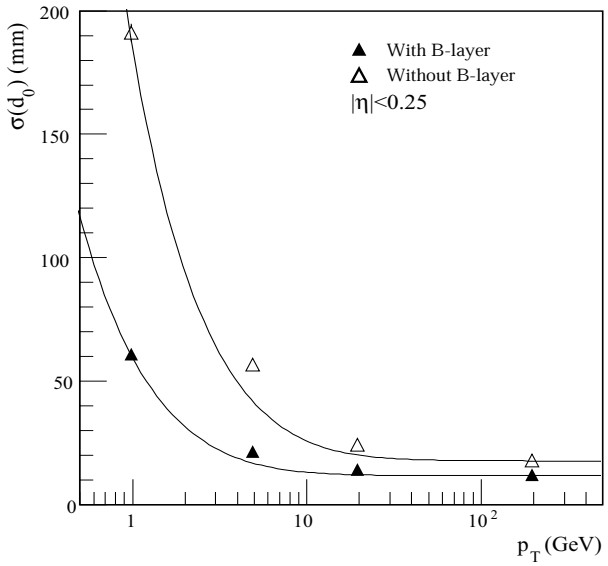

Figure 2.11: *Impact parameter resolution with and without B-Layer [2].*

better impact parameter resolution. Figure 2.11 depicts the difference between these two layouts. The resolution $\sigma(d_0)$ without the B-Layer for $p_T > 10$ GeV is 35 μm instead 23 μm and the difference becomes more pronounced at low p_T [2].

2.2.5 Trigger, Data Acquisition and Computing

Combining the LHC bunch crossing frequency of 40 MHz with the large number of channels ($\sim 10^8$) it is apparent, that the anticipated data rate of ATLAS will be too high for offline storage and thus must be reduced to about 10 MB/s to 100 MB/s before being recorded for the offline analysis. This will be performed with a three-level trigger system as shown in Figure 2.12.

The first level trigger (LVL1) accepts data from the muon and calorimeter trigger chambers at the full bunch crossing rate (40 MHz). During the LVL1 latency[4] of about $\sim$ 2 μs the data from all subsystems is stored in pipeline memories. These are located within the front-end electronics of each detector. In the case of a positive LVL1 decision the full event data is transferred from the pipeline memories to the LVL2 buffers. The LVL1 trigger decision rate is limited by the capabilities of the readout systems to a maximum rate of 100 kHz. The LVL2 trigger further reduces the trigger rate to $\sim$1 kHz by analysing the regions of interest (ROI), which are identified by the LVL1 trigger. ROI are, for example, high-p_T electromagnetic clusters, jets, and muons. Most of the sub-detectors and the full granularity of the data is used. The up to 10 ms latency is sufficient to perform the complicated processing to find for example tracks in the Inner Detector, to measure their p_T and to compare the energies of the corresponding cluster in the electromagnetic calorimeter.

[4]the time required to collect and process the data and to distribute the trigger decision

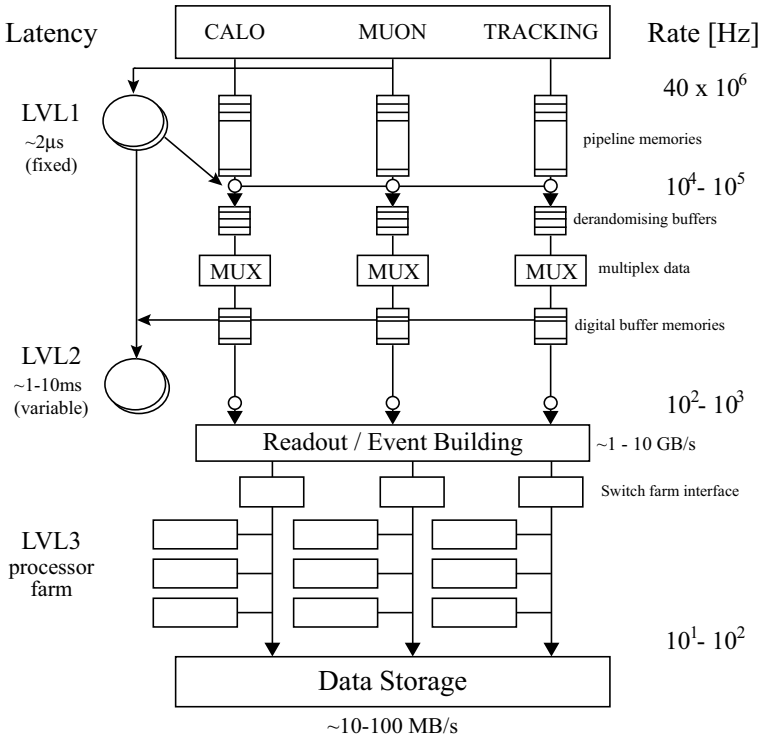

Figure 2.12: *The* ATLAS *three-level trigger architecture [3].*

The events accepted by the LVL2 trigger are sent to the LVL3 processor farm for complete event reconstruction with a decision time of ∼1 s. This requires a computing performance on the order of $\sim 10^6$ MIPS. The selected events are written into storage at a rate of about 10 to 100 events per second, resulting in a data rate of 10 MB/s to 100 MB/s for an event size of ∼ 1 MB. In this way, about 10^6 GB are accumulated in one ATLAS year.

Chapter 3

The Pixel Detector for the ATLAS Experiment

This chapter gives a detailed description of the Pixel Detector for the ATLAS experiment. The main elements of the Pixel system are summarised with a focus on the front-end side of the detector. At the end of this chapter a general overview of the optical links system is given.

3.1 Requirements and General Description

Short living particles, such as B–mesons or τ–leptons, travel only a short distance before they decay. A highly granular detector system is needed to cope with the many charged particles produced, on average, from every LHC proton–proton collision. The secondary vertices reconstructed out of the particle tracks is identified as the decay point. For the high precision reconstruction of the secondary vertices, the following requirements must be fulfilled:

- High number of channels,
- high resolution,
- high signal to noise ratio,
- digital read-out,
- and sensitivity during read-out.

The Pixel Detector provides a minimum of three spacial points within the pseudo-rapidity of $|\eta| \leq 2.5$ with an efficiency of at least 95%. These hits must be clearly assigned to one bunch crossing. In order to register these hits with a high resolution, the pixel cells have to be realised as small as possible. Additionally the detector has to maintain its integrity within a harsh radiation environment for 10 years of LHC, up to $\sim 1{\cdot}10^{15}\mathrm{n}_{eq}/\mathrm{cm}^2$ for Silicon and $\sim 7{\cdot}10^{15}$ n_{eq}/cm^2 for Gallium Arsenide (GaAs). The calculation of this radiation level is described in Chapter 4.3.

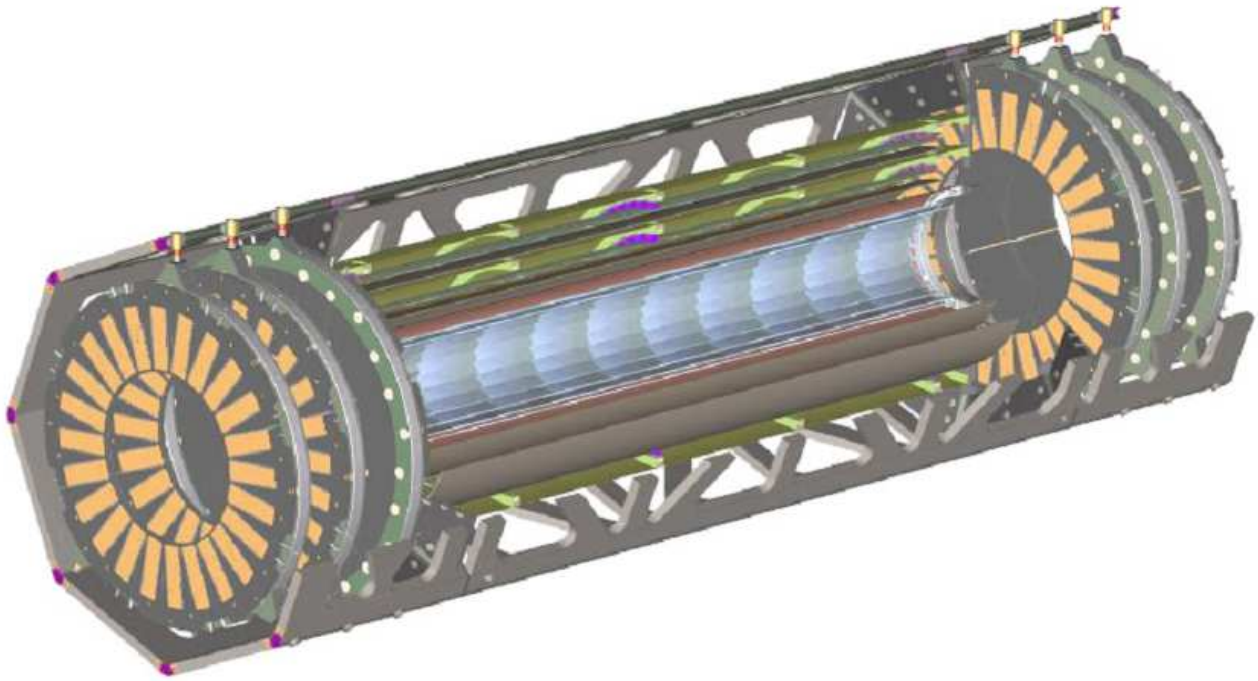

Figure 3.1: *The* ATLAS *Pixel Detector with three barrel layers and three forward and backward disks [4].*

The ATLAS Pixel Detector contains 1744 modules. It consists of a barrel area cylindrically arranged around the beam axis, and a forward region to facilitate a better coverage of the forward – and backward area at large pseudo-rapidity. The barrel cylinders are situated at radii of 50.5 mm (B-Layer), 88.5 mm (Layer 1) and 122.5 mm (Layer 2). The barrel modules are in groups of 13, which are mounted on identical longish supporting structures (staves). Similarly, all the disk modules are located on identical support sectors that are joined to form disks. Figure 3.1 depicts the total view of the Pixel Detector. Some of the geometrical values are summarised in Table 3.1.

Barrel	radius (mm)	staves	modules	chips	channels	active area (m^2)	tilt angle (°)
B-layer	50.5	22	286	4576	$1.8{\cdot}10^7$	0.28	-20
Layer 1	88.5	38	494	7904	$3.0{\cdot}10^7$	0.48	-20
Layer 2	122.5	52	676	10816	$4.2{\cdot}10^7$	0.65	-20
Subtotal		112	1456	23296	$9{\cdot}10^7$	1.41	
Disks Z(mm)	inner r (mm)	outer r (mm)	modules	chips	channels	active area(m^2)	sectors
495	88.1	148.9	48	768	$2.2{\cdot}10^6$	0.04	8
580	88.1	148.9	48	768	$2.2{\cdot}10^6$	0.04	8
650	88.1	148.9	48	768	$2.2{\cdot}10^6$	0.04	8
Subtotal			288	4608	$1.3{\cdot}10^7$	0.27	48
TOTAL			1744	27904	$\sim 1.0{\cdot}10^8$	1.68	

Table 3.1: *Geometrical values of the* ATLAS *Pixel Detector*

A stave is 78 cm long and supports 13 modules. On each side six modules are declined by 1° towards the centre. This enables an overlap of the module ends in that way, that there are no gaps between the modules. The middle module is parallel to the beam pipe. Since the mechanical support structure needs an extreme stiffness, even within an area with a high temperature gradient, the development of this part is demanding. Within the support structure, the so-called stave, the cooling is situated. Cooling is necessary to prevent radiation damages and to transport the thermal energy out of the detector system. A "omega" piece incorporates the cooling pipe and provides the required stiffness with a simple geometry. The Carbon-Carbon (C-C) structure (very stiff) tested gives good thermal properties in all directions: About 1200 W/(mK) in plane, about 40 W/(mK) in transverse. Furthermore, the structure is low mass to reduce production of secondary particles. To prevent leaking through the porous material a tube is placed into the omega piece.

3.2 Pixel Modules

A hybrid pixel detector consists of a fine segmented sensor area, where each segment (pixel cell) is connected via a bump bond to a readout cell. In order to get larger building blocks, modules are formed. The total number of the Pixel Detector modules is 1744 with about 10^8 single hybrid pixel cells and a total area of 1.7 m^2. Each module consists of following components:

- the sensor with an active area of 16.4 mm x 60.4 mm, which also serves as support for the remaining components (Section 3.2.1),
- 16 electronic chips, the front-end chips (Section 3.2.2),
- a chip to drive in parallel the input and output of the front-end chip, the module controller chip (MCC) (Section 3.2.4),
- a temperature sensor to monitor the cooling of the module, connected to an interlock system,
- passive components.

The passive components are for example decoupling capacitors attached to the read-out chips. The main components of a detector module (sensor, front-end chips and module concepts) are described in greater detail.

3.2.1 The Sensor

A particle sensor is, in principle, made of a basic depleted pn-junction. Charged particles passing through the detector produce electron-hole pairs in the depleted n-type silicon, which results in signals in the front-end electronics connected to each sensor cell. The energy loss per pathlength, due to ionisation is given by the Bethe-Bloch formula:

$$-\frac{dE}{dx} = 4\pi\alpha^2 \frac{(\hbar c)^2}{m_e c^2} n_0 \frac{z^2}{\beta^2} \cdot \ln\left(\frac{2m_e c^2 \beta^2}{(1-\beta^2)I} - \beta^2\right) \tag{3.1}$$

$\frac{dE}{dx}$	energy loss per pathlength
α	$= \frac{e^2}{4\pi\epsilon_0\hbar c} \sim \frac{1}{137}$, fine structure constant
$m_e c^2$	$= 511$ keV
n_0	$= N_A \cdot \rho \cdot Z/A$
N_A	Avogadro´s number
ρ	density of Silicon
$z \cdot e$	particle charge
β	$= v/c$, normalised velocity of particle
$A = 28, Z = 14$	mass and charge number of silicon
$I \sim 140$ eV	mean ionisation potential of silicon

The ATLAS Pixel collaboration successfully developed a radiation hard sensor design which meets the challenging requirements of the ATLAS Pixel Detector. At the same time the hardening of the silicon itself was followed within the ROSE collaboration, which developed the radiation tolerant DOFZ-silicon[1] with oxygen enrichment by diffusion [26].

The design of the sensor for the ATLAS Pixel detector takes advantage of the fact, that a n-type Silicon bulk converts at room temperature at a fluence of $\sim 10^{13}$ n_{eq}/cm^2, to a p-type behaviour [42, 31]. The n^+-in-n has the advantage, that the complete n-side of the sensor is at ground potential, therfore sparking from the sensor bias into the FE-electronics does not occur (up to 600 V). Furthermore, a n^+-in-n sensor can detect particles even when not fully depleted, because the depletion area builds up from the n-side (after type conversion).

Of course, p-isolation is required for the n^+-in-n sensor structure to interrupt the low resistive contact between the n^+-implantations in the n-bulk . This can be achieved by two different isolation techniques: p-stop and p-spray. Figure 3.2 illustrates these two processes.

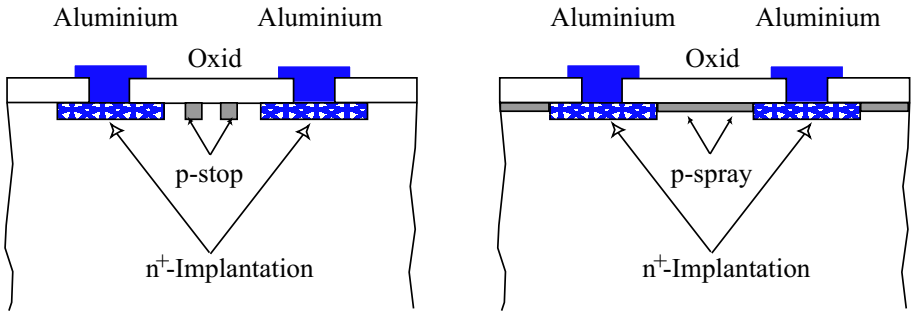

Figure 3.2: *P-stop and p-spray isolation technique [26]*

In the case of p-stop, the n-structure of each pixel is surrounded by p^+-implantations, whereas in the p-spray technique the complete n-side is covered with a p-implantation of medium dotation. In the p-stop design, the electric eld increases under ionising irradiation; in the p-spray design it decreases. The advantage of this is that a p-spray sensor can be

[1] diffused oxygenated float zone

tested with the highest expected electric field before the wafer is further processed. P-spray has a number of advantages, for example, the design is simpler and therefore smaller structures is achievable. Additionally, a bias-grid structure is possible. This is necessary in order to test the sensor, already on wafer level for the quality assurance requirements. The bias grid structure foresees a connection of every pixel via punch through and therefore allows to test the quality of the whole pixel array with only two contacts. A summary of the sensor requirements and the chosen design features to meet these requirements is given in Table 3.2 [26].

	Requirements	Design Features
Module Issues	small pixel cell fitting the readout cell	50 μm $\times$ 400μm (B-Layer: 50 μm $\times$ 300μm)
	small sensor thickness	250 μm (B-layer: 200 μm)
	no dead area between FE-chips	elongated resp. ganged pixels
	compatible with bump bonding	silicon nitrite passivation with 12 μm diameter opening
Quality Assurance	testability on wafer level	bias grid with punch-through connection to every pixel cell
	coping with missing bumps	bias grid with punch-through connection to every pixel cell
	edges on ground potential after type conversion	n-in-n sensor with guard rings only on the p-side
Radiation Tolerance	increase of oxide charge without excess current or noise	p-spray isolation
	high breakdown voltages before and after irradiation	moderated p-spray isolation

Table 3.2: *Overview of the sensor requirements and chosen design features for the* Atlas *Pixel Detector [26].*

3.2.2 The Front–End Read Out

Each front-end (FE) readout chip serves 18 columns and 160 rows of pixel cells. The main function of each cell is to register the (negative) charge collected at the n+ implantation in the sensor after a particle passes through one of the 2880 pixel cells. Figure 3.3 schematically describes the readout of one pixel cell. The charge signal is fed through the bump-bond connection into a charge sensitive, low noise preampli er with a parallel feed back capacitor and integrated leakage current compensation. The feed back capacitor is charged by the signal and, due to the parallel constant current source, quasi linearly discharged. Because of an additional capacitor it is possible to inject a known charge in order to test the chip without a radioactive source. The amplified signal is led from the preamplifier, over the AC coupling, to the discriminator with an externally set threshold. In the case of a signal

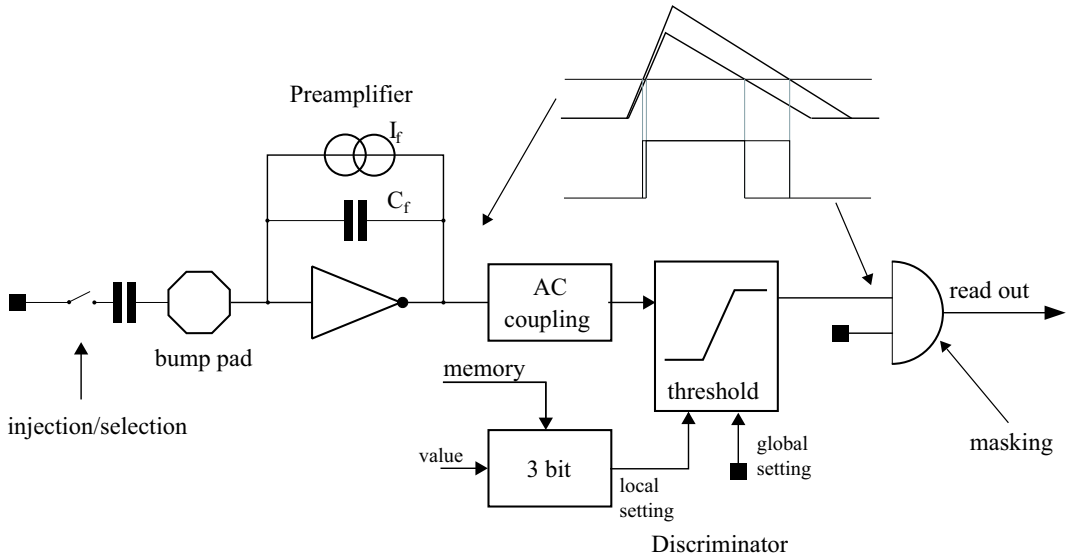

Figure 3.3: *Schematic overview of a front-end cell [28].*

larger than this threshold the signal is digitised. The discriminator threshold is globally set, but additional tuning with external bits makes individual fine tuning possible, and thus, the spread of the threshold over one chip can be minimised. The step size of this fine tuning is globally set. The information leaving the discriminator is purely binary, and therefore does not contain information about the charge of the particle responsible for the hit. In order to extract this desired information the Time over Threshold (ToT) is used. By taking advantage of the linear discharge, the duration of the signal above the threshold in units of 25 ns, is obtained. The principle of this ToT is illustrated in Figure 3.3. The time information of the identified rising and falling edge is fed into the read out and the End of column (EoC) logic calculates the ToT value. The particles from a multi-hit can be better determined using the weighted mean of the ToT values, therefore efficiently increasing the resolution [32].

A series of different front-end chips was used in order to develop a radiation hard FE-chip for the ATLAS Pixel Detector. One of the first prototype chips was the FE-A, a BiCMOS chips with shift register readout, developed by the Marseilles/Bonn cooperation. Bipolar transistors were only used for the discriminator to optimise its speed. In parallel the same logic was implemented in CMOS (FE-C) with a different discriminator. A further chip with the a time stamp readout was the FE-C, also a CMOS chip. These chips showed promising results, but all processes were not radiation hard. In order to get the best possible chip, the more simple and better analog part of the FE-A/C and the time stamp readout of the FE-B were merged into the DMILL chip FE-D. Due to a very low yield and general problems of this chips, this chip development was stopped. Since other collaborations presented good results with deep submicron (DSM) technologies the present development is a DSM version of the same logic. First functionality tests and irradiation tests show very promising results.

3.2.3 Flex Hybrid Module and MCM–D Module

The chip dice are attached via flip-chip assembly[2] to the sensor diodes. An important consideration is to ease module interconnections to the data and control lines. Power distributions are routed to the periphery of the module and subsequently to a module controller chip and a power distribution cable. For the Pixel Modules there are two different designs under study, the Flex-Hybrid and the MCM–D module. The more conservative option of

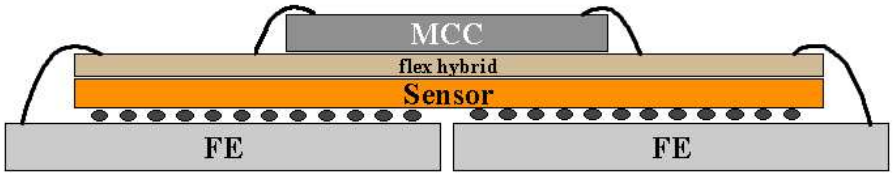

Figure 3.4: *Cross section of a flex hybrid module.*

these two approaches is the Flex-Hybrid design. As illustrated in Figure 3.4, a thin flexible kapton foil is attached to the backside of the sensor. On this foil the necessary tracks for the signals and power are integrated. Additional area is available to house further components, such as the module controller chip MCC (Section 3.2.4) or passive components. This is the so-called "chip-down" arrangement where the readout chips are connected to the mechanical support (staves), providing a good thermal exchange. The readout chips protrude the sensor by about 1 mm. The connection between kapton foil (flex hybrid) and the chips is established with wire-bonds. The MCC is also connected via wire-bonds. Due

[2]bump-bonding process where the bumps are placed onto the sensor and the chips are flipped on top

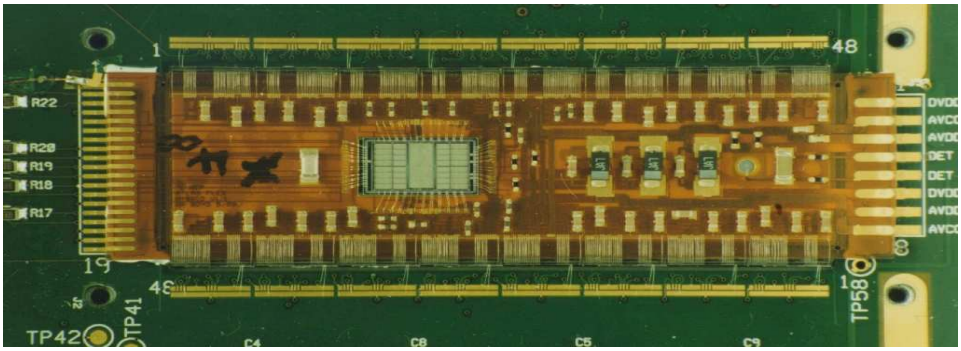

Figure 3.5: *Total view of a flex hybrid module. A flexible kapton with a module control chip and some passive components is glued onto the top of the sensor. The necessary routing is done on the flex and the corresponing lines are wire-bonded to the front-end chips (visible on the long sides of the Flex-Hybrid).*

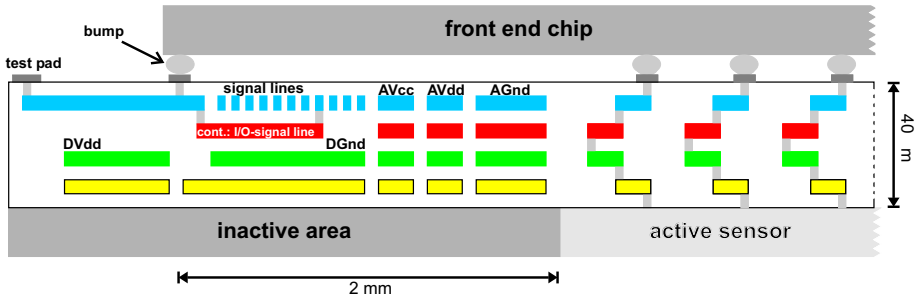

Figure 3.6: *Schematic cross section of the four layer bus and signal system. On the right–hand side the feed through connections from the detector to the read out chip are illustrated [27, 28].*

to the approximately 640 highly delicate wires (10 μm thickness), handling during assembly might be difficult. Potting is not forseen since this would add radiation length. This approach is, at present, the baseline design for the ATLAS Pixel detector. A total view of a flex hybrid module is shown in Figure 3.5.

An alternative approach for the innermost layer modules (B–physics layer) is the MCM–D technology. To avoid complicated wiring and different interconnection technologies, all lines in this proposal are deposited directly onto the detector substrate. The interconnection lines are thus located between the sensor silicon and the electronic chips. Figure 3.7 shows a MCM–D module with outer dimensions of 24.6×78.8 mm^2. This design is the "chip-up" arrangement where the modules are attached with the sensor side facing the mechanical support. This technology is called MCM–D as the chip interconnections are formed by *depositing* dielectric material and conductors onto a base substrate. In the case of the Pixel modules, the substrate is high-resistive, active, fully depleted silicon sensor (section 3.2.1). All sensor elements are connected to their corresponding read-out cells by small pitch, via connections through the four dielectric layers. This is only achievable with a multilayer metallisation scheme, using a thin film Copper/ Photo-BCB[3] process on the pixel sensor array. The bumping of the read out chips is accomplished using electroplating PbSn. All dice are then attached by flip-chip assembly to the sensor diodes and the local busses. Figure 3.6 shows a schematic cross section of this layout. A minimum of 25 μm for the diameter of these so-called vias is allowed by the design rules. A minimum of 3 μm thick isolation between the metal layers is demanded. The four copper layer system for the signal and power bus is situated below the end-of-column logic of the chips within the outermost 2 mm on both long sides of the sensor substrate. This thin film technology has been described in [30, 29] and is under further development at Fraunhofer-IZM in Berlin in close cooperation with the University of Wuppertal. A prototype module is depicted in Figure 3.7.

[3]Benzocyclobutene

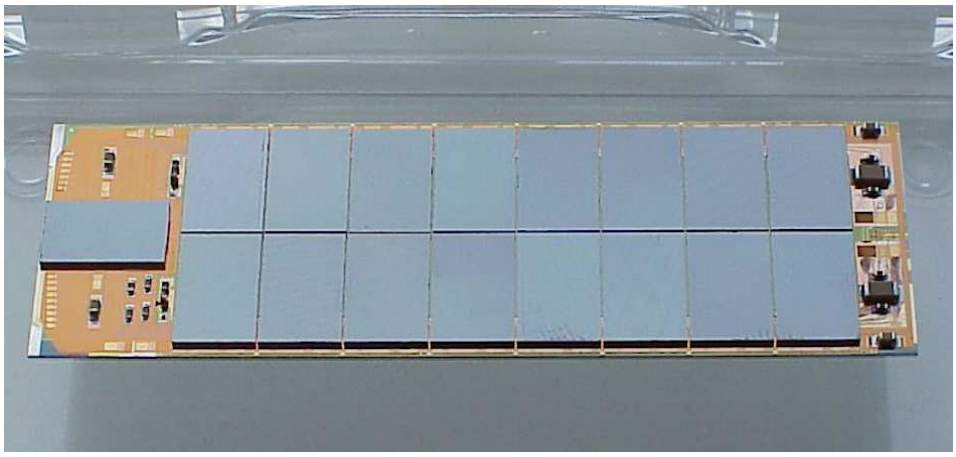

Figure 3.7: *MCM-D prototype module where all interconnection lines are located between the sensor silicon and the electronics chips. The single chip on the left-hand side is the module controller chip MCC.*

3.2.4 The Module Controller Chip

The data transfer to and from the 16 FE-chips is coordinated by the module controller chip (MCC). The MCC fulfils some basic tasks:

- upload of the FE-chips configuration at startup,
- distribution of the timing signals (40 MHz clock) and the level 1 trigger (LVL1),
- read-out of the front-end chips and generation of the hit events ("event builder").

Figure 3.8 illustrates the main functions of the MCC [33]:

- Front-End Port: the interface between the 16 FEs and the MCC. All signals are transmitted in LVDS[4] levels.
- Receiver Channel: for each of the 16 FEs exists one receiver channel with a FIFO, which stores and derandomises the incoming data. This block also contains all FIFO control logic, dealing with read/write pointers and possible overflows. The error or warning conditions are flagged and introduced in the data stream processed by the Event Builder.
- Event Builder: it fills an event scoreboard with the End of Event (EoE) flags to keep track of all the incoming events. In the case of a LVL1 trigger, the Level 1 trigger counter (LVL1 CNT) copies the trigger number into a LVL1 FIFO. Once all 16 FE chips have sent a complete event (terminated by an EoE flag) the Event Scoreboard in the MCC triggers the Event Builder to extract the hits from the FIFOs, to format them in an event and to transmit it to the Read Out Driver (ROD, section 3.3).

[4]Low Voltage Differential Signal for Scalable Coherent Interface (SCI) Draft 1.3 IEEE P1596.3 - 1995

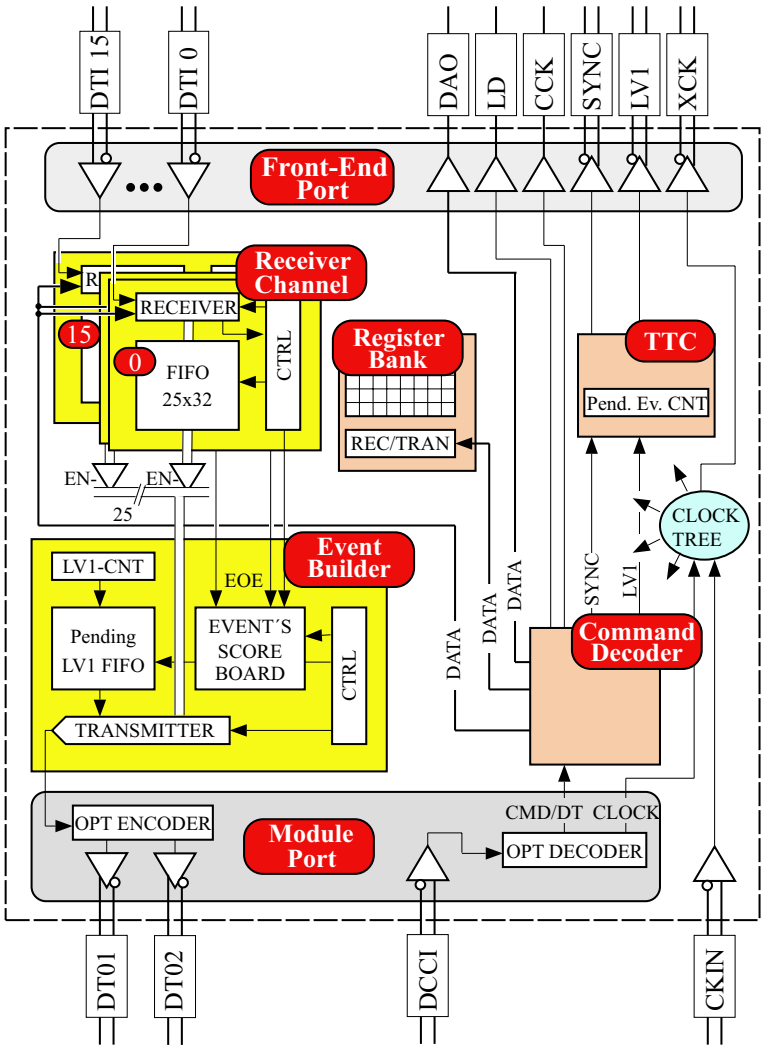

Figure 3.8: *Module controller chip block diagram [33].*

- Register Array: 16 general purpose, 16 bit wide registers are situated inside the MCC. The MCC has a configuration mode, a run mode and a transparent mode to access directly the FE chips. These different operating modes of the MCC can be selected by setting the appropriate register. Registers are divided into Status and Control registers.

- Command Decoder: the serial commands sent to the MCC are decoded and organised into two main categories: fast and slow commands. Slow commands automatically set the MCC out of data acquisition mode and are meant for configuration and test purposes only. Fast commands can be issued during data acquisition (for example the LVL1 trigger command).

- Trigger and Timing Control: in case of too many events still to be reconstructed, the LVL1 sent to the FE chips is blocked; this is necessary in the FE/MCC data push architecture to avoid synchronisation loss.
- Module Port: the interface between the MCC and the ROD, using LVDS drivers.
- Clock Tree: in order to minimise clock skew on the module, the clock signal received by the MCC is buffered inside the chip and re-distributed to the FE-chips. This buffered clock signal is also fed-back to the MCC itself to synchronise data from the FE chips and to clock the chip core.

The MCC receives the data collected from all 16 FE-chips in a special parallel format, which is illustrated in Figure 3.9. After a starting bit (always "1") the information follows.

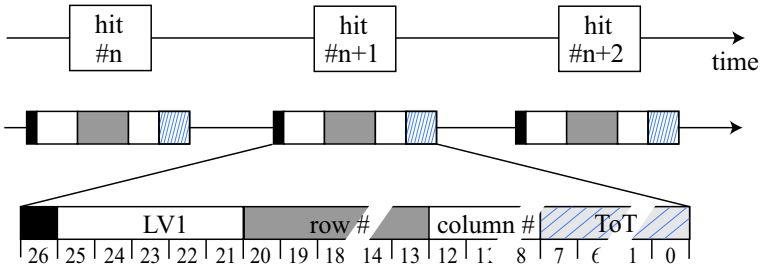

Figure 3.9: *Data format of the collected data from the FE-chip to the MCC.*

This information includes the level 1 trigger (5bits), the row-number (8bit) and the column number (5bit) of the hit cell. The last 8 bits are allocated for the ToT-value. This sequence always has a length of 26 bits. If multi hits occur for one chip, the hit data is read out in series.

The MCC generates a data stream which summarises all hit information belonging to a certain LVL1-signal (Figure 3.10). The sequence starts with the LVL1-signal, followed by the number of the first chip which registered hits with this LVL1, and the ToT values. Then all other chips which registered a hit with the same information sequence follow. The end of the complete sequence is defined by 22 consecutive zeros as the length of the data sequence is not constant [33].

The MCC is also designed in different processes, from the non radiation hard AMS process over DMILL to a deep submicron process. The DMILL chips showed the same low yield as the FE-chips. The module control chip (MCC) was developed at the INFN in Genova, Italy.

3.3 Read Out Driver

The Read Out Driver (ROD) is the key element of the SCT/Pixel Off-detector electronics system. It contains the primary functions for the readout and control of the SCT/Pixel

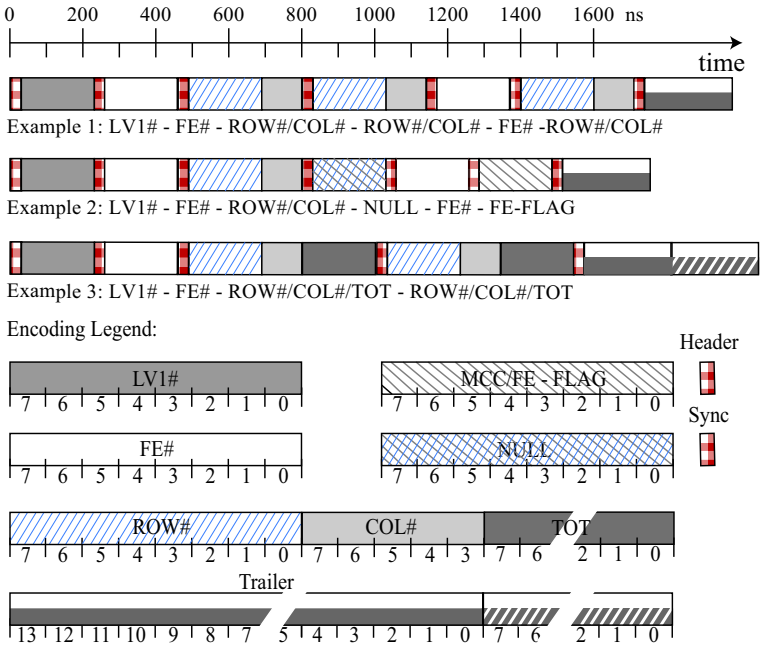

Figure 3.10: *Event data output of the MCC*

subsystem and interfaces this system with the ATLAS-wide systems which provide timing, trigger, and control signals. In addition to detector readout and ATLAS interfacing, the ROD manages electronics calibration, diagnostics, and detector monitoring. The ROD interfaces with its neighbouring components which all reside in standardised VME data acquisition crates. For each VME crate, the ROD Crate Controller (RCC) provides local supervision of all readout and control operations in the crate. The ROD receives commands from the RCC via VME. All RCCs in the system are linked by local area networks to the ATLAS data acquisition system.

The ROD receives signals from the ATLAS-standard timing, trigger, and control (TTC) system via a custom VME module called the TTC Interface Module (TIM). The TIM communicates with the ROD via a custom backplane on the VME crate. The ROD processes and formats detector data and merges data streams. It buffers data until it transfers the data on a $\approx$ 1 Gbps fibre optic Readout Link (ROL) to its Readout Buffer (ROB) in the ATLAS Trigger/DAQ System. The whole ROD is positioned about 100 m distant from the Inner Detector.

3.4 Optical Links System Architecture

The Timing, Triggering and Control (TTC) has to be transported from the ROD to each detector module and the collected data has to travel the reverse path. The large number of channels in the ATLAS detector makes the use of copper links unfeasible due to the large

amount of material which would be introduced. Also problems with cross talk and ground loops would appear. Therefore most of the subdetector communities decided to use optical links for the transport of these informations.

This section describes the principle architecture of the optical links of the SCT and the Pixel Detector. Both detector subsystems use a similar bi-directional optical data transmission for the provision of timing and control information to the detectors, and transfer of the collected data to the acquisition system situated up to 100 m away. The control data links use Bi-Phase Mark (BPM) encoding to combine the 40 MHz machine clock with control information. BPM encoding sends transitions corresponding to clock leading edges only with extra transitions at clock trailing edges to indicate data 1's. The Clock has to be regenerated from leading edge transitions and data from the extra transitions. Figure 3.11 illustrated the BPM encoding and decoding taking place in the electronics of the optical link.

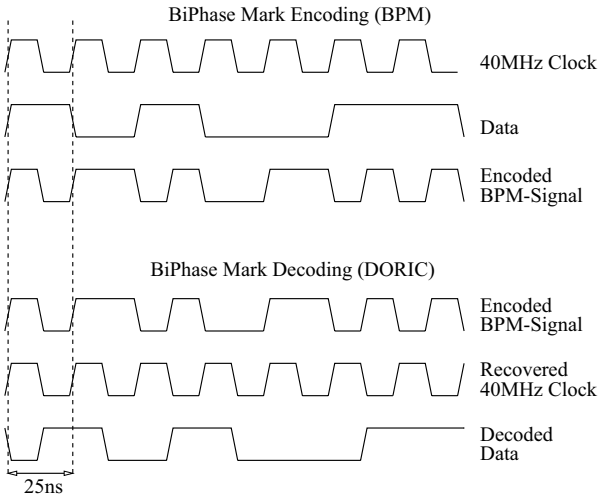

Figure 3.11: *The BiPhase Mark encoding: BPM encoding sends transitions corresponding to clock leading edges only with extra transitions at clock trailing edges to indicate data 1's.*

The data links of the SCT operate at 40 Mbit/s and use Non Return to Zero (NRZ) coding of the digital readout data. In NRZ code a "0" is transmitted as low level signal, a "1" is transmitted as high level signal, not returning to the low level between successive "1" bits. Due to the higher data rate in the Pixel Detector, a higher transmission rate is necessary. In case of the outer layers and the disks of this subsystem the data link a transmission of 80 Mbit/s NRZ is forseen. The B-layer in the centre of the Pixel detector will use 160Mb/s transfer. This is accomplished with two links of 80 Mbit/s NRZ each.

The principle architecture of the optical data links for the ATLAS SCT and Pixel Detector is shown in Figure 3.12, divided into a on-detector and off-detector side. The on-detector side includes all devices placed within the ATLAS Detector, whereas the off-detector side consists off all parts placed onto the read out driver (ROD) outside the detector. Different

locations for the on-detector optical link are possible, one of them is the patch panel PP0 at the end of the barrel close to the outer radius. Therefore the flux and fluences for different radii including the PP0 radius are calculated from simulation outputs in Chapter 4. In the following chapters the choice of emitters, receivers, opto-packages and electronics is described in detail, including radiation tolerance and lifetime studies.

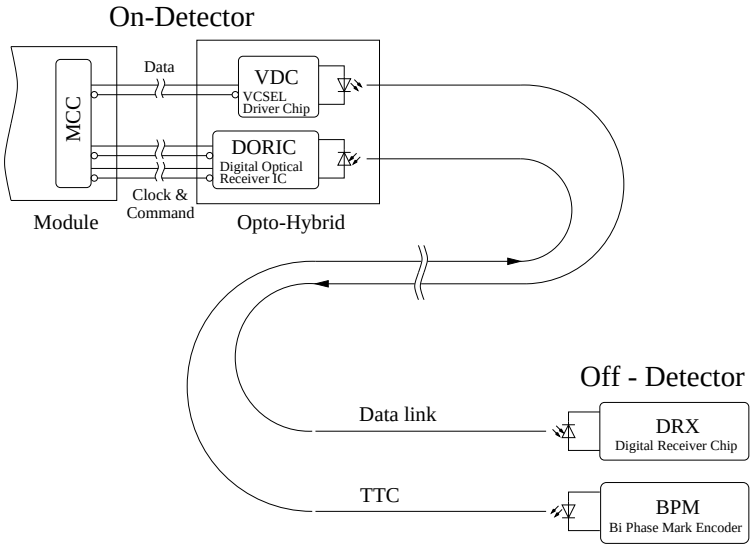

Figure 3.12: *The principle architecture of the optical links for the* ATLAS SCT *and Pixel Detector. Clock, Trigger and Control (TTC) are transmitted from the Read Out Driver (ROD) to the detector modules while the collected data signals follow the reverse path.*

Chapter 4

Radiation Environment of the Atlas Inner Detector

The high rate at which particles are produced in the proton-proton collisions at Lhc result in a large amount of radiation inside the detector, leading to radiation damage of detector elements and the electronics, and to the activation of detector material. All parts of the detector, including the optical link, are affected by radiation damages. In this chapter the radiation damages, occurring in a semiconductor device, are described. The NIEL hypothesis is introduced and flux and fluence numbers for the Atlas Inner Detector are calculated.

4.1 Radiation Induced Damages in Semiconductors

The effects of radiation on semiconductors can be classified into two groups: ionisation and displacement damage. Ionisation causes surface damages, whereas displacement is responsible for bulk damages.

The ionisation is mainly caused by charged particles and photons, and can lead to radiation induced photo-currents (single event effects, Chapter 9) or to space-charge-buildup, if the generated charges are trapped in localised trapping centres. These space-charge buildup is a long-term ionisation effect and is mainly a problem if the device contains insulating layers like SiO_2 thin films used in MOS[1] devices. Defects induced by these space-charge buildup can lead to a number of defects in a complex circuit [34]:

- The speed of a circuit is decreases due to the decrease of the conductivity.
- The dynamic current consumption rises, the rise and fall time of the signals increase.
- The threshold characteristic of transistors change and the transistor might stop to switch.

The device degradation due to ionisation scales approximately with the total energy deposited by irradiation (total dose). Damages in circuits can vary quite strong. They are

[1] metal-oxide-semiconductor

depending on dose, radiation duration, applied voltage, layout and size of the devices. It is hard to make predictions for the behaviour of a chip. Therefore radiation studies are essential for chips which are designed for a radiation harsh environment as the ATLAS Pixel Detector.

Bulk damages may be caused both by neutral and charged particles, although for the charged particles ionisation is the primary effect. If a high energy particle interacts with an atom in the semiconductor lattice enough kinetic energy may be transfered to dislodge the atom from its position in the lattice (primary knock atom, PKA). The PKA will rapidly loose its kinetic energy due to ionisation or displacement of further atoms until it stops. A cascade of collision processes will be produced. Displacement of particles results in different local point-defects (i.e. vacancies, interstitial). A high energy particle can build up large defect complexes of local point-defects. These complexes can in general not be repaired completely. Usually smaller stable defect complexes will remain. The defects induce several energy-levels in the bandgap of the semiconductor. These additional energy-levels have consequences on the physical behaviour of devices such as the PiN diodes or the laser diode:

- In cases with a flat energy-band the majority carrier might be trapped and de-trapped with a delay. This can result in a partial loss of the signal charge because of the decrease in the charge collection efficiency (cce). The cce is indirectly depending on the depletion voltage. By increasing the depletion voltage it is possible to increase the cce up to a certain degree. However, this effect is small against the following two [81, 35].

- Energy-level in the middle of the forbidden bandgap act as *generation* and *recombination* centres. Thus, this effect can cause a change of the carrier density and is detectable as a higher leakage current. This rise is mainly due to radiation induced defect clusters of vacancies and interstitials, and less due to point defects. The current rise is proportional to the fluence of the damaging particles and the depleted volume V. It is particularly independent of the particle kind and the initial material. It is possible to parametrise the current rise [36, 35]

  $$\Delta I = \alpha \cdot \phi_{eq} \cdot V \tag{4.1}$$

  where the proportional factor α describes the damage constant, which is, without considering the annealing, approximately $8 \cdot 10^{-17}$ Acm^{-1}. The leakage current is also depending on the temperature:

  $$I_{leak} \sim T^2 \exp(-\frac{E_g}{2k_B T}) \tag{4.2}$$

  Cooling of the devices is necessary to keep the leakage current low.

- Compensation of donators or acceptors. This results in a change of the majority carriers and the effective doping concentration. A change in the effective doping concentration has a direct impact on the depletion depth and therefore on the sensitive volume of a pn-junction. Donator- and acceptor-like defects are deactivated and at

the same time acceptor-like levels are created proportional to the fluence. These two effects lead to a typical fluence behaviour as depicted in Figure 4.1 [37]. The effective doping concentration is decreased at small fluences, at higher fluences the linear increase of acceptors dominates and the material changes to p-type. This has a great impact on the electrical behaviour of the devices, e.g the diode. The field gradient in the pn-junction inverses and with this the spreading direction of the depletion area is inversed as well [37]. Furthermore the rise in the effective doping concentration leads to a necessary increase of the voltage to gain full depletion.

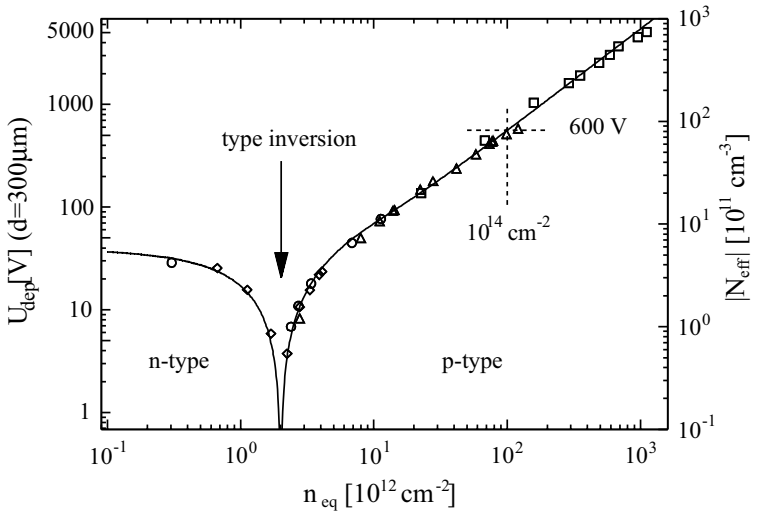

Figure 4.1: *Change in the effective doping concentration depending on the 1 MeV equivalent neutron fluence [37].*

The last two effects are important for the understanding of radiation damages in the PiN photodiode summarised in Section 5.1. The total energy loss due to non-ionising interactions is described as *non-ionising energy loss*.

4.2 NIEL scaling hypothesis

The NIEL (non-ionising energy loss) hypothesis offers a possible way of correlation and unification of the experimental data in radiation hardness studies on semiconductor detectors. According to NIEL scaling, any particle fluence can be reduced to an equivalent 1 MeV neutron fluence producing the same bulk damage in a specific semiconductor. The scaling is based on the hypothesis, that generation of bulk damage is due to non-ionising energy transfers to the lattice.

Given an arbitrary particle field with a spectral distribution $\phi(E)$ and of fluence Φ, the 1 MeV equivalent neutron fluence is:

$$\Phi_{eq}^{1MeV} = \kappa\Phi \tag{4.3}$$

κ is called the hardness parameter and is defined as:

$$\kappa = \frac{EDK}{EDK(1MeV)} \tag{4.4}$$

with EDK the energy spectrum averaged displacement KERMA (kinetic energy in matter).

$$EDK = \frac{\int D(E)\phi(E)dE}{\int \phi(E)dE} \tag{4.5}$$

where ϕ is the differential flux, and

$$D(E) = \sum_k \sigma_k(E) \int dE_R f_k(E, E_R) P(E_R) \tag{4.6}$$

with

$D(E)$	the displacement KERMA or the damage function for the energy E of the incident particle,
σ_k	the cross-section for reaction k,
$f_k(E, E_R)$	the probability of the incident particle to produce a recoil of energy E_R in reaction k
$P(E_R)$	and the partition function (the part of the recoil energy deposited in displacements) [38].

$EDK(1MeV) = 95$ MeVmb [39]. The integration is done over the whole energy range. Figure 4.2 shows the displacement damage functions in silicon recommended by Angela Vasilescue in [41]. The damage function can be converted into NIEL values with following conversion:

$$NIEL = \frac{N_A}{A} D(E) \tag{4.7}$$

For silicon A =28.086 g/mol and consequently

$$100 \text{ MeV mb} = 2.144 \text{ keVcm}^2/\text{g} \tag{4.8}$$

The damage functions of high energy particles in GaAs are not as well experimentally determined as for silicon. In [40] the NIEL for fast neutrons, protons and pions in GaAs has been deduced from published calculations. There is a strong correlation between the observed reduction of charge collection efficiency with radiation dose from NIEL. The results are summarised in Figure 4.3 and Figure 4.4. The calculated and experimentally established results indicate, that GaAs has a greater radiation hardness to neutron irradiation than Silicon. This is due to the fact that the 1 MeV neutron cross sections are similar for the two materials whilst the number of atoms in GaAs per unit mass is lower due to the larger atomic weight. On the other hand the NIEL for fast protons and pions is

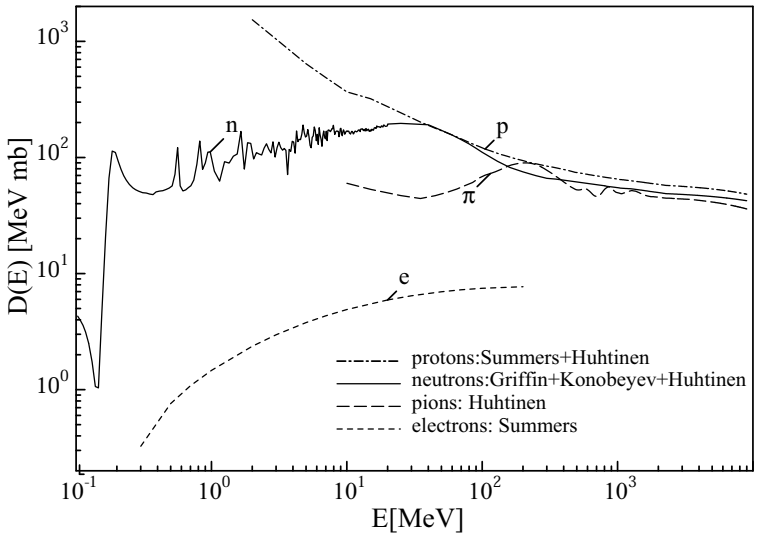

Figure 4.2: *Recommended displacement damage functions for NIEL scaling in silicon [41].*

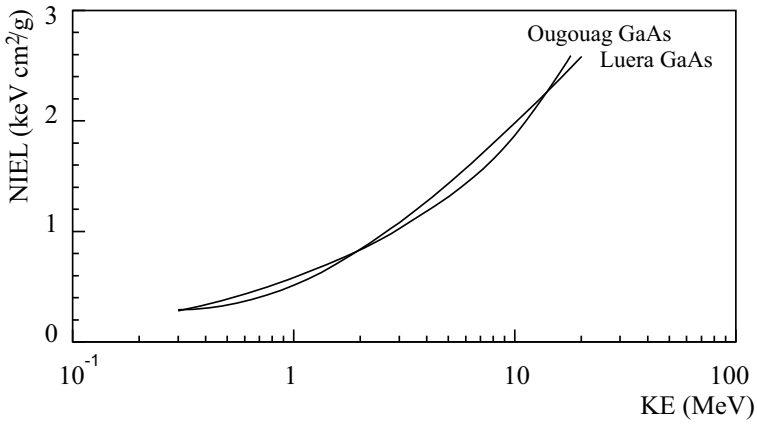

Figure 4.3: *Calculations of the NIEL stopping power for neutrons in GaAs as a function of neutron kinetic energy [40].*

larger in GaAs than in Silicon. This can be understood from the Lindhard factors for the two materials. The Lindhard factors give the total fraction of the energy which appears as ionisation energy [42]. Figure 4.5 shows the Lindhard factors as a function of the energy for Silicon and GaAs. The threshold energy above which the ionisation becomes dominant is about 7 times higher in GaAs than in Silicon due to the lower velocities of the heavier ions in the former. As a result the average NIEL deposited by a fast recoil in GaAs is higher than that in silicon [40].

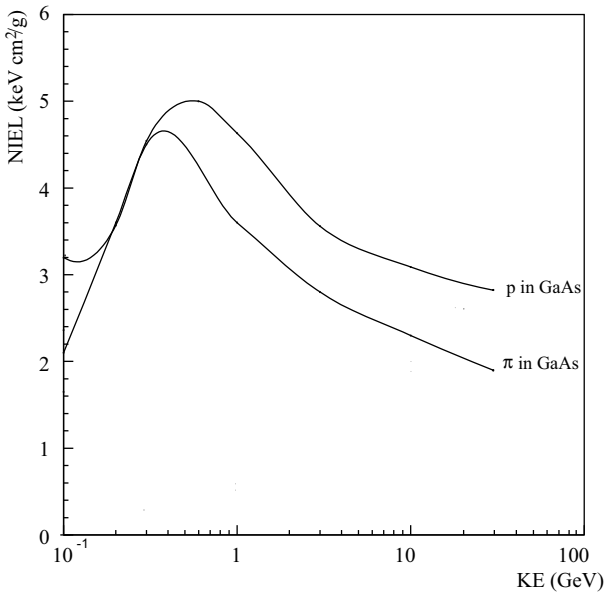

Figure 4.4: *Calculations of the NIEL stopping power for pions and protons in GaAs as a function of kinetic energy [40].*

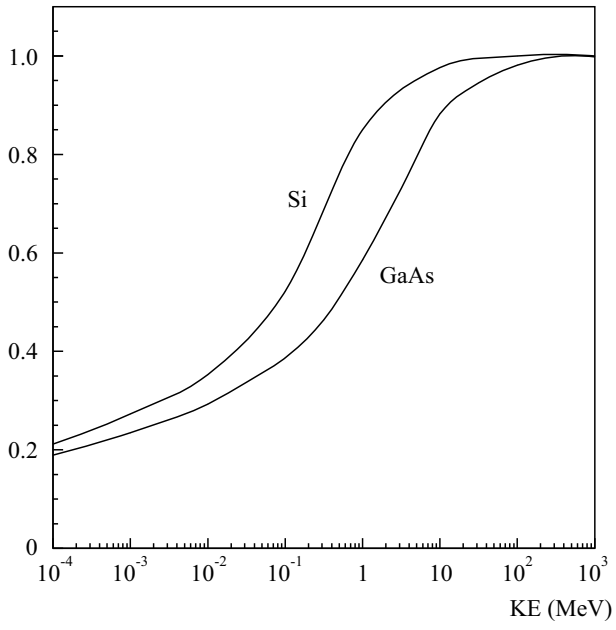

Figure 4.5: *The total fraction of the energy appearing as ionisation energy due to interactions with atomic electrons for GaAs ions in GaAs and Si ions in Si calculated according to the formulae of Lindhard et al [42, 40].*

4.3 Flux and Fluence calculations

The simulations of the expected radiation levels for the ATLAS Inner Detector were performed by A. Ferrari [43], constructing a detector model which produces the location and quantity of the material in the Inner Detector and calorimeter regions, including the supports and services. A Monte Carlo program for hadronic multi-particle production has been used to generate minimum bias particles. This DTUJET code is based on the two-component dual parton model which includes the dual topological unitarisation of soft and hard cross sections [44]. The generated particles have been passed through the detector simulation and their subsequent decays or interactions were treated with the FLUKA transport code. At the radii of the Inner Detector, the dominant source of radiation is the direct proton-proton interaction, with typically 23 interactions per BCO[2] (every 25 ns) at the full luminosity of 10^{34} cm^{-2}s^{-1} [4].

The cross sections used by the DTUJET program for the particle flux are $\sigma_{Inelastic}$ =81 mb and σ_{NSD} =67 mb[3] [45]. The ATLAS assumption is σ_{NSD} = 70 mb. Therefore this number has to be corrected for this difference in the cross section σ_{NSD}. The total number of interactions per LHC year ($1{\cdot}10^7$ sec) is calculated for all layers:

$$N_{int} = \sigma_{inelastic} \int \mathcal{L} dt \tag{4.9}$$

$$= (81 \cdot 10^{-27}) \cdot (70/67) \cdot (1 \cdot 10^{41}) \tag{4.10}$$

$$= 8.5 \cdot 10^{15} \tag{4.11}$$

The expected flux and fluence numbers of charged and neutral particles quoted in this report are calculated for different positions in the Inner Detector, using the FLUKA output as input. For all calculations the so-called ATLAS luminosity scenario is assumed: For the first and the second pixel layer and all SCT layers this means three years of low luminosity operation (10^{33}cm^{-2}s^{-1} for 10^7 s/year) followed by seven years of high luminosity operation (10^{34}cm^{-2}s^{-1} for 10^7 s/year) (section 2.1.3). For the Pixel B-layer three years of low luminosity operation followed by two years of high luminosity operation are assumed.

4.3.1 Flux results

The fluxes are also necessary to define the fluxes needed during single event effect studies at test beams. The particle flux f, the number of particles per second and cm^2, is needed to estimate the behaviour of the device under test in such an environment. At high fluxes single event effects (SEE, Chapter 9) are expected. The output of the FLUKA code is the number of particles per cm^2, interaction and energy bin. From this output the flux in the the ATLAS Inner Detector was calculated using:

$$f = \int \frac{dN}{dE} \cdot dE \tag{4.12}$$

[2]Bunch Cross-Over
[3]NSD = non single diffractive

The radii of all Pixel layers have changed since the TDR [4]. In order to calculate the fluxes for the new radii, the calculated fluxes for the old radii were plotted versus the radii and fits were applied. The charged particles were fitted with an inverse quadratic function, the neutrons with an ansatz with a free but negative exponent. The fit parameter were also used to determine the flux for the PP0 area at a radius of 18 cm, which was not included in the original simulation. Table 4.1 lists the results for all barrel layers of the SCT and Pixel Detector. The flux for the forward disks is always below the lowest flux for one barrel subsystem and is therefore not included in the table.

	pions ($1/cm^2sec$)	neutrons ($1/cm^2sec$)	total ($1/cm^2sec$)
B-Layer	$2.57 \cdot 10^7 \pm 3.2 \cdot 10^4$	$1.78 \cdot 10^6 \pm 9.5 \cdot 10^3$	$2.75 \cdot 10^7 \pm 3.3 \cdot 10^4$
1st-Layer	$8.57 \cdot 10^6 \pm 1.3 \cdot 10^4$	$7.88 \cdot 10^5 \pm 5.1 \cdot 10^3$	$9.36 \cdot 10^6 \pm 1.4 \cdot 10^4$
2nd-Layer	$3.87 \cdot 10^6 \pm 6.6 \cdot 10^3$	$4.79 \cdot 10^5 \pm 5.4 \cdot 10^3$	$4.35 \cdot 10^6 \pm 8.5 \cdot 10^3$
PP0	$2.01 \cdot 10^6 \pm 3.4 \cdot 10^3$	$3.08 \cdot 10^5 \pm 3.5 \cdot 10^3$	$2.32 \cdot 10^6 \pm 4.9 \cdot 10^3$
SCT 1	$9.88 \cdot 10^5 \pm 1.9 \cdot 10^3$	$1.90 \cdot 10^5 \pm 1.6 \cdot 10^3$	$1.18 \cdot 10^6 \pm 2.5 \cdot 10^3$
SCT 2	$6.84 \cdot 10^5 \pm 1.3 \cdot 10^3$	$1.46 \cdot 10^5 \pm 8.9 \cdot 10^2$	$8.30 \cdot 10^5 \pm 1.6 \cdot 10^3$
SCT 3	$4.99 \cdot 10^5 \pm 9.8 \cdot 10^2$	$1.28 \cdot 10^5 \pm 8.0 \cdot 10^2$	$6.27 \cdot 10^5 \pm 1.3 \cdot 10^3$
SCT 4	$3.78 \cdot 10^5 \pm 7.7 \cdot 10^2$	$1.17 \cdot 10^5 \pm 7.3 \cdot 10^2$	$4.95 \cdot 10^5 \pm 1.1 \cdot 10^3$

Table 4.1: *Flux numbers and statistical error for all barrel layers of the* ATLAS *Inner Detector, separated between pions and neutrons, and the total number of particles per* cm^2.

4.3.2 Fluence results

Particle fluence F is defined as the number of particles traversing a unit area in a certain point in space for a given period of time weighted with a particle- and material-specific damaging factor. Most frequently, it is measured in cm^{-2}. In particular, neutron fluence in high-energy physics applications is of interest in the context of the radiation environment around the interaction regions of colliders; it serves as a measure for potential radiation damage for the detector systems to be used. It is common practice to express charged and neutral particle contributions to radiation in terms of dose and 1 MeV neutron equivalent fluence (also NIEL scaling), respectively.

The annual fluences at high luminosity were calculated as following [46]:

$$F_{neq} = \int \frac{dN}{dE} \cdot dE\left(\frac{NIEL(E)}{NIEL(n_{1MeV})} \cdot N_{Int}\right) \tag{4.13}$$

$$F_{peq} = \int \frac{dF}{dE} \cdot dE\left(\frac{NIEL(E)}{NIEL(p_{24GeV})} \cdot N_{Int}\right) \tag{4.14}$$

F_{neq} gives the fluence of neutral particles whereas F_{peq} is used for the calculation of the charged particles. By assuming that the damages in Silicon and in GaAs scales with the

NIEL, the NIEL values for Silicon and GaAs were taken from Figure 4.2, 4.3, and 4.4 [40] respectively. For particle energies between the given values, the NIEL value was interpolated. Commonly the total fluence is given in 1 MeV equivalent neutrons. Therefore the fluence calculated for the charged particles has to be converted with a conversion factor, i.e. for GaAs:

$$\frac{NIEL(\mathrm{p}_{24GeV} \text{ in GaAs})}{NIEL(\mathrm{n}_{1MeV} \text{ in GaAs})} = \frac{2.9}{0.55} = 5.27 \tag{4.15}$$

The annual fluences for the new radii, including PP0, were also calculated by applying the same fitting strategy as in 4.3.1. The total fluence was calculated by adding the 1 MeV annual fluences for charged particle and neutrons and scaling to the full LHC lifetime. A +50% safety margin has been added to allow for the uncertainties; this is a common procedure agreed on within the ATLAS collaboration. Table 4.2 lists all annual fluences for charged particles and neutrons for all barrel layers of the Inner Detector. For all radiation studies one should refer to the total numbers, also listed in Table 4.2. Since the B-Layer will be removed after 5 years the quoted fluences are higher for the 1st-Layer.

4.3.3 Conclusions

The expected fluxes have been calculated from simulation outputs for the TDR radii and interpolated to the radii of the present design. Similarily the fluences have been calculated giving an estimated fluence of $1.1{\cdot}10^{15}\mathrm{n}_{eq}/\mathrm{cm}^2$ for the Silicon and $7.8{\cdot}10^{15}\mathrm{n}_{eq}/\mathrm{cm}^2$ for GaAs. This demonstrates a very hazardous environment for the detector components and makes radiation damage studies to the core of device evaluation.

		Silicon n_{1MeV}/cm^2	GaAs n_{1MeV}/cm^2
neutrons (1 year)	B-Layer	$4.39 \cdot 10^{13}$	$1.23 \cdot 10^{14}$
	1st-Layer	$2.69 \cdot 10^{13}$	$6.01 \cdot 10^{13}$
	2nd-Layer	$1.99 \cdot 10^{13}$	$3.89 \cdot 10^{13}$
	PP0	$1.55 \cdot 10^{13}$	$2.79 \cdot 10^{13}$
	SCT 1	$1.15 \cdot 10^{13}$	$1.93 \cdot 10^{12}$
	SCT 2	$9.78 \cdot 10^{12}$	$1.58 \cdot 10^{12}$
	SCT 3	$9.14 \cdot 10^{12}$	$1.44 \cdot 10^{12}$
	SCT 4	$8.53 \cdot 10^{12}$	$1.33 \cdot 10^{12}$
charged (1 year)	B-Layer	$2.28 \cdot 10^{14}$	$1.96 \cdot 10^{15}$
	1st-Layer	$7.58 \cdot 10^{13}$	$6.53 \cdot 10^{14}$
	2nd-Layer	$3.33 \cdot 10^{13}$	$2.67 \cdot 10^{14}$
	PP0	$1.86 \cdot 10^{13}$	$1.55 \cdot 10^{14}$
	SCT 1	$9.22 \cdot 10^{12}$	$7.07 \cdot 10^{13}$
	SCT 2	$6.43 \cdot 10^{12}$	$4.77 \cdot 10^{13}$
	SCT 3	$4.73 \cdot 10^{12}$	$3.41 \cdot 10^{13}$
	SCT 4	$3.52 \cdot 10^{12}$	$2.45 \cdot 10^{13}$
total (LHC)	B-Layer	$9.4 \cdot 10^{14}$	$7.2 \cdot 10^{15}$
	1st-Layer	$1.1 \cdot 10^{15}$	$7.8 \cdot 10^{15}$
	2nd-Layer	$5.8 \cdot 10^{14}$	$3.3 \cdot 10^{15}$
	PP0	$3.7 \cdot 10^{14}$	$2.0 \cdot 10^{15}$
	SCT 1	$2.3 \cdot 10^{14}$	$9.9 \cdot 10^{14}$
	SCT 2	$1.8 \cdot 10^{14}$	$6.9 \cdot 10^{14}$
	SCT 3	$1.5 \cdot 10^{14}$	$5.3 \cdot 10^{14}$
	SCT 4	$1.3 \cdot 10^{14}$	$4.1 \cdot 10^{14}$

Table 4.2: *Annual fluences for the barrel layers of the* SCT *and Pixel detector in 1 MeV equivalent neutrons and the total fluences, including a 50% headroom.*

Chapter 5

Optical Components

Essential parts of an optical link, such as the optical link for the ATLAS Pixel Detector, are the opto-electron devices and the waveguide. This chapter describes the principle functionality of the PiN photodiode and the VCSEL, and gives an overview of radiation hardness studies for the on-detector PiN photodiode and the optical fibres.

5.1 PiN Photodiode

A photodiode is a semiconductor photodetector which generates an electrical current proportional to the incident optical power. Photons incident on a semiconductor are absorbed by electrons in the valence band. As a result, these electrons acquire higher energy and are excited into the conduction band, leaving behind a hole in the valence band. When an external voltage is applied to the semiconductor, these electron–hole pairs give rise to the photocurrent. The energy of the incident photon must be at least equal to the bandgap energy in order for a photocurrent to be generated. This gives the following constraint on the wavelength λ at which a semiconductor material with bandgap E_g can be used as a photodetector:

$$\frac{hc}{\lambda} \geq E_g \tag{5.1}$$

with c the velocity of light. The bandgap energy E_g for Silicon is 1.17 eV. The efficiency η of the photodetector is given by

$$\eta = \frac{P_{abs}}{P_{in}} = 1 - e^{-\alpha L} \tag{5.2}$$

where α is the absorption coefficient and L the thickness of the active area. Typical values of α, for Silicon and a wavelength of 840 nm, are in the order of 10^3 cm^{-1}.

Photo-detectors are commonly characterised by their responsivity R, the ratio between the current I_p and the incident optical power, and with Equation 5.2:

$$R = \frac{I_p}{P_{in}} = \frac{e\eta\lambda}{hc} = \frac{\eta\lambda}{1.24} A/W \tag{5.3}$$

To improve the efficiency of the photodetector, a very lightly doped intrinsic semiconductor is introduced between the p–type and the n–type semiconductor. Such photodiodes are called PiN photodiodes, where the i in PiN stands for intrinsic. In these photodiodes, the depletion region extends completely across the intrinsic semiconductor. The width of the p–type and n–type semiconductors is small compared to the intrinsic region so that much of the light absorption takes place in that region. This increases the efficiency and thus the responsivity of the photodiode [47]. After extensive radiation tests [50, 49, 48, 51] an epitaxial silicon PiN-diode was chosen for the SCT and the Pixel optical links as on-detector receiver. This kind of photodiodes shows a lower, but acceptable responsivity ($R \sim 0.5$ A/W at 850 nm) than other PiN-diodes, but the fast rise and fall times ($\leq$1 ns at -5 V bias) make them suitable for the operation at 80 Mbit/s. The intrinsic region which forms the depletion layer is only $\sim$ 15 μm thick. Therefore the epitaxial devices can be fully depleted at very low bias voltages even after radiation damage has increased the carrier concentration. After irradiating 96 of these PiN-diodes[1] up to the radiation level of the Pixel B-layer (see chapter 4.3), none of the PiN-photodiodes has died, but the responsivity has decreased to 0.3 A/W. The lowest R at 10 V bias is not dependent of the total fluence [48], as illustrated in Figure 5.1. Previous results [50] have shown the responsivity dropping quickly at the beginning of the irradiation, and then remaining constant despite the increase of the total fluence. The decrease of the responsivity can be explained by the change of the doping concentration and majority carriers in the active layer described in section 4.1. The normalised responsivity as a function of the reverse bias at different fluences is depicted in Figure 5.2. The responsivity is normalised to the

[1] manufactured by Centronic, Croydon,UK

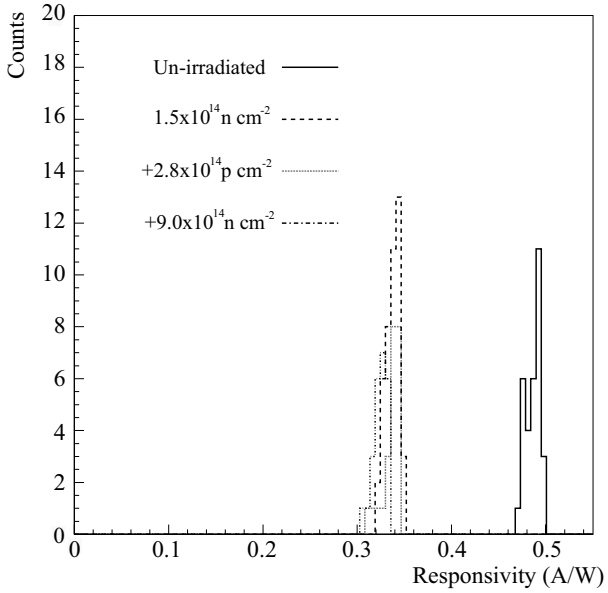

Figure 5.1: *Variation of the silicon PiN photodiode responsivity for different fluences, measured for one sample PiN at 10 V bias voltage [48].*

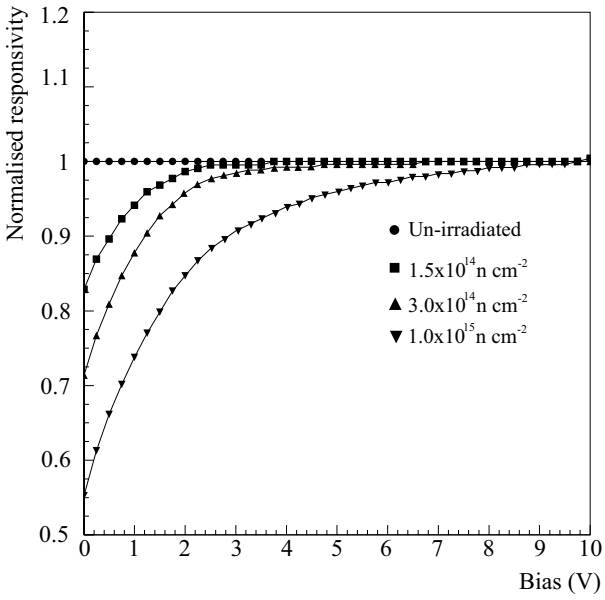

Figure 5.2: *Normalised responsivity as a function of the reverse bias at different fluences [48]. The responsivity is normalised to the mean responsivity at 10 V bias voltage for each fluence sample group.*

mean responsivity at 10 V bias voltage for each fluence sample group. A plateau at the normalised responsivity of one is reached with a bias less than 0.1 V but in the case of irradiated devices, this plateau has been moved toward 2.5 V for low irradiation fluence. For the highest fluence, the bias has increased up to 8 V. A bias voltage of up to 10 V during the experiment is foreseen for the Pixel Detector. It would also be possible to apply 10 V bias from the beginning of the experiment without decreasing the performance; a simple power supply could be used.

For the highest integrated neutron dose of 500 kGy, the dark current is 60 nA at room temperature, decreasing to a negligible value at the cold temperature of the Inner Detector [49]. This is analogous to the described increase of the leakage current in sensor cells due to additional introduced energy-levels in the forbidden bandgap (Section 4.1). Calculating the current increase ΔI according to Equation 4.1 one gets $\sim$ 80 nA for the PiN photodiode. This is slightly higher than the measured value, but of the same order.

An accelerated ageing test[2] was performed with the irradiated and tested lot. This was done by using an elevated temperature of 60°. The estimation of a lower limit to the Mean Time To Failure after 5679 h of ageing, with no failure recorded, is more than 4568 years at 90% Confidence Level [49]. This means less than 1 % failure among 2112 PiN diodes for the SCT barrel modules and less than 4 % for the Forward which has an higher temperature of 15°C for the 10 LHC years.

[2]The Arrhenius relation used can be found in section 6.4

The temperature for the Pixel optical link is not defined yet. If the Pixel optical link is positioned close to the modules onto the stave or disks, the temperature would be -5°C. Using the data above, this would mean less than 1 % failure among the 1744 photodiodes. In case of a higher temperature the maximum failure rate would increase. For a temperature of 5 °C it would amount to 2 % failure, whereas for 20°C up to 6.5% PiN could fail (90% confidence level).

To conclude, these results show, that a higher temperature might limit the lifetime of the PiN photodiodes substantially. A cooling which sets the ambient temperature to (0±5)°C would ensure a long lifetime and limit the dark current of the PiN diodes at the same time.

The off-detector photodiode has to be sensitive at 850 nm since this is the wavelength of choice. A closer look at this device is given in Section 7.2.

5.2 The Laserdiode

Light production using a semiconductor is based on spontaneous and stimulated emission. In equilibrium condition a semiconductor contains a certain number of electrons and holes. By applying a bias voltage the number of electrons is increased by ΔN and the number of holes is increased by ΔP. Electrons and holes are always produced in pairs, therefore is $\Delta N = \Delta P$. When turning off the bias voltage, the number of electrons and holes in the semiconductor decreases until equilibrium is gained back. The decrease ΔN is proportional to $\exp(\frac{-t}{\tau})$ where t is the time since turning off the bias and τ the carrier lifetime [52]. In case of a forward-biased pn-junction the electrons and holes can only recombine with a small probability. The electrons will drift into the p-type and the holes into the n-type. They become minority carriers and recombine with majority carriers. The above mentioned carrier lifetime is the lifetime of the minority carriers. The decrease of the carrier density can be due to radiative and non-radiative transitions. In case of a radiative transition the energy is transferred into a photon; phonons are produced in the non-radiative transition which results in a temperature rise of the device. Radiative transitions are commonly transitions between conduction- and valence-band, whereas non-radiative transition take place between bands within the forbidden band gap. The more level exist between conduction- and valence-band, the faster recombine the carriers and the lifetime decreases. The total lifetime is depending on radiative and non-radiative lifetime

$$\frac{1}{\tau_0} = \frac{1}{\tau_{0_R}} + \frac{1}{\tau_{0_{NR}}} \tag{5.4}$$

with τ_0 the total minority carrier lifetime, and τ_{0_R} and $\tau_{0_{NR}}$ are the lifetimes associated with radiative and non-radiative processes. The decrease in $\tau_{0_{NR}}$ is usually responsible for the reduction in the lifetime τ. The lifetimes are usually written as

$$\frac{1}{\tau_{0_R}} = \sigma_R v_{th} N_R \tag{5.5}$$

and

$$\frac{1}{\tau_{0_{NR}}} = \sigma_{NR} v_{th} N_{NR} \tag{5.6}$$

where σ_R and σ_{NR} are carrier capture cross sections, N_R and N_{NR} are the concentrations of the radiative and non-radiative centres, respectively. Finally v_{th} is the minority carrier thermal velocity [53].

In order to produce lasers, it is necessary to design a system such that some of the light that originates from spontaneous or stimulated emission is not allowed to leave the material. In this way the light would be continually stimulating more identical photons, continually building the intensity of the propagating light in the material. This effect is obtained through the creation of a resonant optical cavity called a Fabry-Perot cavity. The basic form of a Fabry-Perot cavity consists of two parallel mirrors (with reflectivities R1 and R2) separated by a fixed distance D. The first semiconductor lasers consisted of heavily doped p-n junctions with cleaved facets. This construction is inefficient, as there is no defined region in which recombination can take place. Carriers can be lost due to diffusion before recombination occurs. As a result, these early devices required a lot of current to reach threshold. Threshold currents were reduced with the developments of the double-heterostructure laser, which has a thin region of semiconductor with a smaller energy gap sandwiched between two oppositely doped semiconductors with a wide bandgap energy. When forward biased, carriers flow into the active region and recombine more efficiently because of the potential barriers of the heterostructure confining the carriers to the active region.

5.2.1 Vertical–Cavity Surface–Emitting Laser

In the late 1970 s, the Vertical Cavity Surface-Emitting Laser, or VCSEL, was developed at the University of Illinois. Since then, significant research efforts have developed the VCSEL technology to the point where it could become the important semiconductor laser used in optoelectronic systems. The operating wavelength range now extends from 670 nm to 1550 nm. These accomplishments have led this special laser diodes to emerge as potential light wave source for a variety of applications, including high speed optical interconnections, parallel data links, optical recording, and optical signal processing. The application within high energy physics projects was added to this list because of its high radiation hardness compared with common edge emitting diodes [54].

The resonator axis is perpendicular to the plane of the diode which makes the active length of the resonator very short, typically about a μm. Highly reflective mirrors are necessary in order to achieve the needed small threshold currents. Figure 5.3 shows the typical layer structure of a VCSEL diode. The structure consists of a n-doped AlAs-GaAs distributed Bragg reflector (DBR) on a n^+-GaAs substrate, an interlayer with the active un-doped InGaAs zone and an upper p-doped DBR. The Bragg reflectors contain $\lambda/4$ layers of AlAs and GaAs. The maximum reflectivity of these mirrors is $> 99\%$. The quantum well is on both sides surrounded by un-doped GaAs barriers and separated by spacer layers, so that the optical thickness between the DBRs amount to exactly one wavelength [56]. For the short wavelength sector, standards specify the laser wavelength to be

$\sim$ 850 nm to match the working wavelength of GaAs and Silicon photodetectors [58]. The

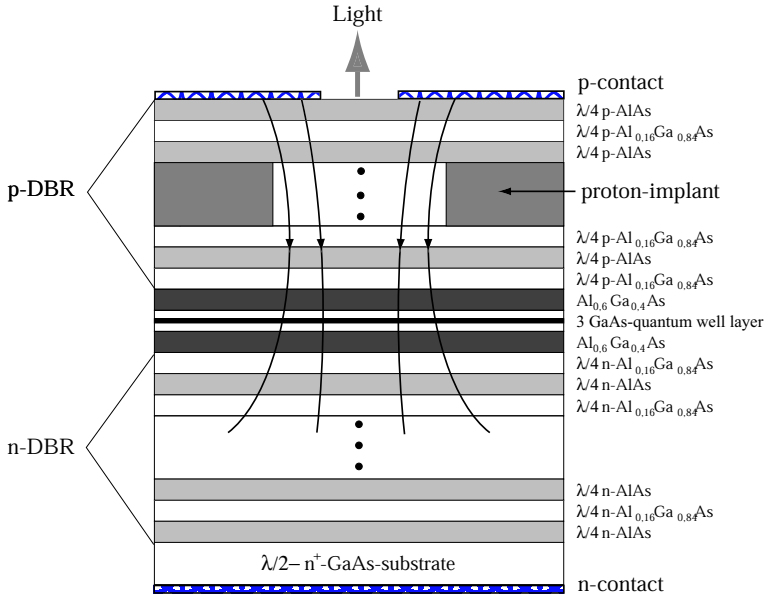

Figure 5.3: *A cross sectional view of a gain-guided surface emitting laser fabricated by proton implantation.*

VCSEL´s planarity allows symmetric transverse cross sections, thereby resulting in circular output beams. This feature, a significant improvement over the elliptical beams exhibited by edge-emitters, is particularly attractive since it improves coupling of the optical output to a fibre. Planarity also results in other important advantages, including support for on-wafer probe testing, two-dimensional (2-D) integration of arrays, and the ability to limit device area to a particular spot size. Finally, because of their small volume, VCSELs have relatively high modulation bandwidths. The most important advantages of incorporating DBRs include epitaxial growth compatibility and the capability of vertical current injection through the semiconductor reflectors. While the index difference between the two media in the DBR structure is responsible for high optical reflectivity, especially in GaAlAs/AlAs heterostructures, the accompanied energy bandgap difference results in potential barriers in the hetero-interfaces. These barriers impede the carriers flowing in the DBR structures and result in large series resistance.

The VCSEL design must provide an optical confinement for the light-wave propagating in the laser and an electrical confinement for the current which drives the laser. The light bounces between the two DBRs on either side of the active layer. The strong feedback from the mirrors leads to an optical intensity within the cavity. For current confinement ion implantation is favoured since this design can be fabricated with a planar process. Deeply implanted protons create a highly resistive layer buried in the top mirror which funnels the laser current into the active area. The implantation damage can effect the reliability of the laser. Nevertheless, proton implanted VCSELs are favoured by a lot of companies due to their relatively easy fabrication process [58].

The proton implanted VCSELs are grown by MOCVD[3], and include three 7 μm-wide, GaAs quantum wells. The distributed Bragg reflector mirrors are made of quarter-wavelength stacks of AlAs and $Al_{.16}Ga_{.84}As$, with 10 nm wide grade regions to minimise resistance. Increased doping is also used in the graded region to lower mirror resistance. The proton implantation confines the current to a 20 μm ring; p-metals are applied with a 15 μm opening for top emission. The resulting laserdiodes have extremely low threshold currents ($\leq$ 4 mA) and high efficiency, which keeps junction temperature and current density low for normal operating conditions.

A disadvantage of VCSELs is their strong thermal dependence. In analogy to edge-emitting laser-diodes the threshold is temperature dependent. Furthermore increases the temperature the injection current; the output power eventually rolls over and begins to decrease and limiting a devices maximum DC output [59].

The lasers used for the studies presented here are proton-implanted and their threshold currents I_{th} are around 4 mA. In order to decide which VCSEL type is appropriate for the use in the ATLAS Detector numerous tests and irradiation studies were performed. The tests performed in the framework of this thesis which led to the selection of the VCSELs are summarised in Chapter 6. The packaging of the chosen emitters is described in Chapter 7.

5.3 The Passive Optical Component – the Fibre

Compared to other media such as copper lines, optical fibres are remarkable communication media. They provide low-loss transmission over a frequency range up to 25 THz, which is orders of magnitude higher than the bandwidth available with common copper cables or any other medium. Optical fibres consist of an inner core with a higher refractive index and an outer cladding. The optical signal is confined to the core of the fibre by total internal reflection. Fibres can be fabricated with a variety of refractive-index profiles.

In a step-index (SI) fibre the core and the cladding are made of homogeneous materials. The core has a constant refractive index n_1, which changes abruptly to n_2 in the cladding. The dimension of the core is typically 5-15 μm for so-called single-mode fibres and 50-200 μm for multi-mode fibres. The cladding has a thickness of 100-400 μm. SI-fibres are usually the right choice for short distances, but the simple geometry of the waveguide leads to a problem for longer distances: Part of the incoming light pulse travels along the shortest ray path, arriving at the time τ. Other parts travel along longer paths, resulting in larger time delays. It is clear that the delay differences cause the received pulse to be broader than the transmitted pulse. This so-called inter-modal dispersion impairs the information transmission capability of the fibre. The modal dispersion can be in the order of 30 ns/km for SI fibre. Where in graded-index fibres (GRIN) the refraction index of the core is lower outside and increases towards the centre of the core; thus it bends the ray inward and allows them to travel faster. This results in a much reduced dispersion of about 2 ns/km.

Each light guide has an acceptance angle, which is the angle off the light guide's axis within which light rays will enter and continue along. Light rays outside the angle of acceptance will enter and then refract immediately out of the light guide and be wasted.

[3]Metal-Organic Chemical Vapor Deposition

The acceptance half-angle (actually a cone of acceptance), is set by the refraction of light going from the air into the light guide and by the critical angle of the core-cladding interface. The acceptance angle is usually expressed in terms of numerical aperture:

$$\mathrm{NA} = n_0 \sin(\theta_c) \tag{5.7}$$

where n_0 is the refractive index of the surrounding medium, usually air, and θ_c is the acceptance angle. Numerical apertures of fibres can vary from 0.5 to 0.66, leading to acceptance half-angles between 25 and 40 degrees.

Furthermore fibres are classified into two electromagnetic categories: single mode and multi-mode. The mode refers to the number of electromagnetic modes that exist in the fibre under certain conditions. For the ATLAS Experiment only multi-mode fibre is forseen.

5.3.1 Radiation Hardness of Optical Fibres

Irradiated optical fibres show an increase in attenuation due to build-up effects, the so-called colour centres, that partly absorb the light in the fibre. Many factors are observed to influence the amount of radiation damage in optical fibres such as impurity content, geometry, dose rate, total dose, type of incident radiation and temperature. A series of radiation tests was performed to select the right fibre for the harsh radiation environment within the Inner Detector [60, 61, 62, 63].

In a study of optical fibres for the use in the Inner Detector and calorimeter system [63] a SI-Fibre[4] with a pure silica core was found to be a clear candidate for the use within the Inner Detector links. The measured attenuation was < 0.1 dB/m at 500 kGy(Si) and $1{\cdot}10^{15}$ n_{eq}/cm^2. Since only the first 10 m are subject to this high radiation level, this performance is acceptable. The attenuation drops to ~ 0.02 at 100 kGy(Si) and $2{\cdot}10^{14}$ n_{eq}/cm^2, which is about the expected radiation level for the SCT innermost layer. At the lower radiation level expected for the outer regions of the ATLAS detector a Ge-doped GRIN[5] fibre was found to be a good choice. The measured attenuation in this case was less than 0.1 dB/m 800 Gy(Si) and $2{\cdot}10^{13}$ n_{eq}/cm^2. The typical coupling loss for an industry standard fibre connector can be up to 0.5 dB. At least two of such connectors per ATLAS link are foreseen, therefore the attenuation due to irradiation is less than the induced irradiation by connectors.

A further important issue is the minimal bending radius of the fibre. When bending the fibre below 20 mm microcracks are induced. At these microcracks the formation of defects is enhanced. Thus the manufacturers strongly recommend that the fibres should not be bended below this 20 mm radius at any point during the handling.

5.3.2 Mixing of SI Multi Mode and GRIN fibres

The connection of a SI fibre to a GRIN fibre is usually not forseen in an optical system. Due to the price difference between the pure silica Fujikura fibre and the Plasma GRIN

[4] manufactured by Fujikura, Tokyo,Japan
[5] Plasma Optical Fibre B.V, Eindhoven, The Netherlands

fibre, it is planned to switch from one fibre type to the other in the outer region of the detector. This has a great impact on the signal size transfered from one side to the other. An attenuation of up to 3 dB has been observed in systems containing such a transition.

A pure ray optic description can be used to explain this effect: The numerical aperture NA of the GRIN fibre is a function of the radial coordinate with the minimum at the core-cladding boundary and the maximum at the centre of the fibre. The value given for one fibre type refers to the maximum value. The NA of a SI fibre is constant within the core radius. If one tries to launch large angle rays that originate near the core radius in the SI fibre, these rays cannot be captured by the GRIN fibre. Thus the GRIN fibre NA goes to zero at the core-cladding boundary, and is much reduced for off-axis rays. The power carried by these high angle rays is completely lost. On the other hand, sending light pulses from the GRIN fibre to the SI fibre, all the bound ray carried by the GRIN fibre are captured by the SI fibre since they are within its NA [64], provided the core diameters and NAs of the two different type fibres are nearly the same. Due to the different shape of the core (elliptically vs. round) the loss can be in the order of 2 dB.

A possible solution to circumvent this problem is the use of a 50 μm core SI fibre for the inner region of the detector and a 62.5 μm GRIN fibre for the outer region. The large angle rays would be captured within the larger core radius of the GRIN fibre. This solution is only applicable for the direction from the Inner Detector to the read-out system. This additional fibre type would make the services more complex, however, an attenuation of up to 3 dB is unacceptable for such sensitive system. The best solution, but most expensive, would be the use of the SI fibre throughout the whole detector system.

Chapter 6

Radiation and Lifetime of Vertical Cavity Surface Emitting Diodes

The performance of the optical link is directly dependent on the performance of the opto-electronic devices. Due to the high radiation environment, degradation of the VCSELs can decrease the light output. Additionally, the usual degradation due to aging takes place. It is necessary to estimate the impact of these effects on the devices. Radiation effects in semiconductors have been studied for space, military and nuclear applications. With the planning of LHC, this topic has been become more important for the high energy physics community. Important studies in the field of radiation and lifetime of optical devices such as LEDs and VCSELs up to a level of $4{\cdot}10^{14}\mathrm{n}_{eq}/\mathrm{cm}^2$ have been performed by J. Beringer et.al [57]. Radiation hardness studies up to a level of $5.75{\cdot}10^{15}\mathrm{n}_{eq}/\mathrm{cm}^2$, performed in the framework of this thesis, are described in this chapter. The results of accelerated lifetime studies of Mitel VCSELs and their implications on the Pixel optical link are discussed at the end of this chapter.

6.1 Radiation Damage in VCSELs

The degradation of VCSELs by irradiation is primarily due to bulk damage (section 4.1). The generally accepted view of the physical mechanism which causes radiation-induced degradation of the light output from laserdiodes is that non-radiative recombination centres are introduced. These centres compete with radiative centres for excess carriers, which results in a decrease in the minority lifetime [54]. As explained in section 5.2, the total initial lifetime is depending on radiative and non-radiative lifetime. After irradiation the total post-irradiation lifetime can be written as:

$$\frac{1}{\tau} = \frac{1}{\tau_0} + \sigma_{NRI} v_{th} N_{NRI} \tag{6.1}$$

The subscript NRI refers to the radiation induced, non-radiative centres. Assuming no significant overlap of the regions where the individual incident particles produce crystal

defects occurs, the resulting initial defect densities N_{NRI} will be proportional to the fluences ϕ [54, 66]. Thus

$$N_{NRI} = C_i \phi \tag{6.2}$$

where the coefficient C_i denotes a constant whose magnitude involves the probability of generating a particular defect per unit fluence. The damage constant K is then defined by

$$K = \sigma_{NRI} v_{th} C_i \tag{6.3}$$

and eq. 6.1 can be rewritten as

$$\frac{\tau_0}{\tau} = 1 + \tau_0 K \phi \tag{6.4}$$

The measurable quantities in an experiment are the total light output and the current as a function of the forward bias (*LIV-curves*). Assuming that the total current density J in the VCSEL junction is dominated by diffusion currents, then

$$L = C \tau^{\frac{2}{3}} J \tag{6.5}$$

and the ratio τ_0/τ can be directly related to the relative light output RLO[1] after irradiation [66]:

$$(\frac{1}{RLO})^{\frac{2}{3}} = \frac{\tau_0}{\tau} = 1 + \tau_0 K \phi \tag{6.6}$$

It is obvious the minority carrier lifetime τ, and thus the light output, is expected to degrade if the term $\tau_0 K \phi$ becomes significant compared to 1. The damage constant K is determined by the composition of the semiconductor material, by the NIEL of the radiation and by the amount of the annealing which has taken place. Therefore it is not possible to tune K in order to obtain more radiation hard devices. However, by increasing the radiative recombinations through heavily doping the optical emitting region and by operating the VCSEL at high current densities, it may be possible to minimise the pre-irradiation minority carrier life time τ_0.

For VCSELs, the minority lifetime in the lasing regime is dominated by stimulated emission. Thus it is several orders of magnitude smaller than for LEDs and much higher fluences are required to produce a substantial change of τ/τ_0. The minority carrier lifetime is determined by spontaneous emission below the lasing threshold. Therefore, the presence of radiation induced non–radiative recombination centres decreases the light yield and higher currents are required to enter the laser regime. The lasing threshold current of VCSELs is expected to increase during the irradiation.

In addition, heating effects due to increased total current flow will affect the VCSEL operation at high currents well into lasing.

[1] The relative light output is the quotient of the light power after the irradiation and the power before the irradiation

6.2 Radiation Facilities

Facilities at different places in the world have been used to study the behaviour of the devices when being irradiated with different particle types and energies.

- The spallation neutron source ISIS at the Rutherford Appleton Laboratory (RAL), UK has an energy spectrum centred around 1MeV. The ISIS Facility provides beams of neutrons and muons that enable the structure and dynamics of condensed matter to be probed on a microscopic scale that ranges from the subatomic to the macromolecular. It is not possible to bias the sample diodes during the irradiation.
- The T7 irradiation facility was developed for testing the radiation hardness of prototype silicon detectors. The main advantage of this facility is the high particle flux which allows irradiations to a level of the B-layer in a reasonable time. It is located in the T7 area of the East Hall section of the CERN PS, which provides a primary beam of 24 GeV protons. The flux of this beam is high enough to accumulate the fluence of 10 years LHC within days. The VCSELs were irradiated in a shuttle system which was accessible throughout the irradiation. Radiation hard fibres can be brought into the irradiation area over a distance of 15 m and therefore a monitoring of the optical output power was possible.
- Some samples were irradiated in Taiwan with 30 MeV protons.

6.3 Radiation Damages and Annealing Studies

In a first study 28 VCSELs from Mitel[2] were irradiated unbiased with neutrons at the ISIS facility. These laser diodes were divided into two groups. Group A (20 VCSELs) was initially irradiated to a level of $4.1 \cdot 10^{14}$ n_{eq}/cm^2, and after an annealing period and accelerated lifetime studies (section 6.4), a second irradiation followed. The total fluence was about $8 \cdot 10^{14}$ n_{eq}/cm^2. Group B (8 VCSELs) received $5 \cdot 10^{14} n_{eq}/cm^2$ in a single irradiation.

After the irradiation, the VCSELs were annealed at room temperature at different forward currents (10 mA and 20 mA) in order to study the effect of the current on the annealing behaviour. The forward current, the voltage and the optical light output were monitored. The light output as a function of the forward current (LI-curves) measured directly after the irradiation showed that the laser threshold had increased from a pre-irradiation value of 4 mA to 7-8 mA. This is in agreement with the expectations mentioned above. Figure 6.1 depicts the average relative light output (RLO) of group A and B at 10 mA and 20 mA forward current as a function of the annealing time in hours. The lower two curves show the RLO for devices annealed at 10 mA, whereas the upper two represent devices annealed at 20 mA [52]. There is clear evidence that annealing at a higher forward current results in faster and better recovery of the VCSEL. More defect recombination sites are annealed when a higher current flows and the resulting light output is higher.

A third group of devices (group C) was irradiated to a level of 3.10^{15} n_{eq}/cm^2 at the same facility and annealed at 20 mA. The optical power was monitored regularly with

[2]Mitel 1A444, manufactured by Mitel Semiconductors in Sweden

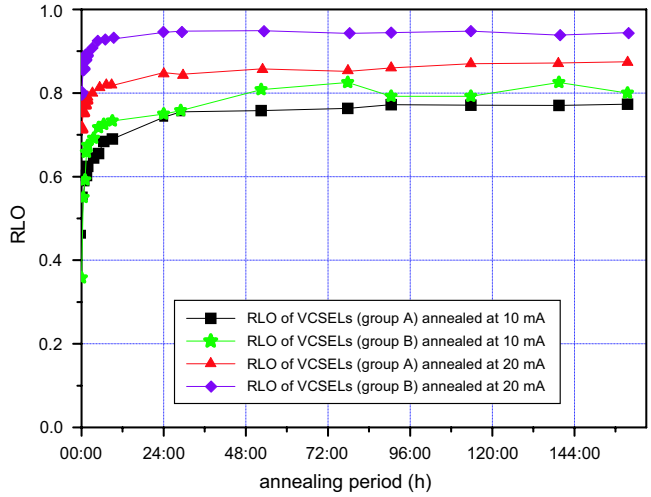

Figure 6.1: *Relative light output (RLO) of* VCSELs *irradiated at ISIS to* $8{\cdot}10^{14}$ n_{eq}/cm^2 *during the annealing period. The* VCSELs *annealed at 20 mA show a better recovery than* VCSELs *annealed at 10 mA.*

an optical power meter[3]. The laser threshold of these laser diodes was >20 mA at the beginning of the annealing period. The diode was never driven with currents above 20 mA in order to avoid damaging the device.

Figure 6.2 shows the optical power of each VCSEL versus the time for 400 hours. Due to the higher fluence, more damages occurred; resulting in a longer annealing period. A group of 15 Truelight VCSELs was irradiated by the PS 24 GeV proton beam at CERN. The laser diodes were positioned in Taiwan packages (section 7.1.4) with radiation hard fibres attached to them. The VCSELs were powered with a forward current of 20 mA during the irradiation and the light output power measured with a hand-held power meter every couple of hours. On each package containing seven or eight laserdiodes an aluminium foil was attached. After the irradiation, ^{22}Na analyses of the Al foils showed a higher accumulated fluence than aimed for. The proton beam during the irradiation period was very stable and the spills contained 50% more protons than expected. The total fluence in 1 MeV equivalent neutrons was $5.75{\cdot}10^{15}$ n_{eq}/cm^2, which is almost a factor 3 more than the expected fluence in for patch panel PP0 ($2.0{\cdot}10^{15}$ n_{eq}/cm^2), at present the baseline position of the optical link.

Figure 6.3 depicts the LI-curves measured before and during the irradiation for one sample VCSEL. As expected, the threshold currents increased with proton fluence. This is due to the increased competition between stimulated radiative recombination, responsible for the laser output, non-radiative recombination at defect recombination sites introduced by the proton-induced displacement damage in the semiconductor lattice of the active region of the laser, and forward bias-induced annealing of defect recombination sites for

[3]Megger OTP 520

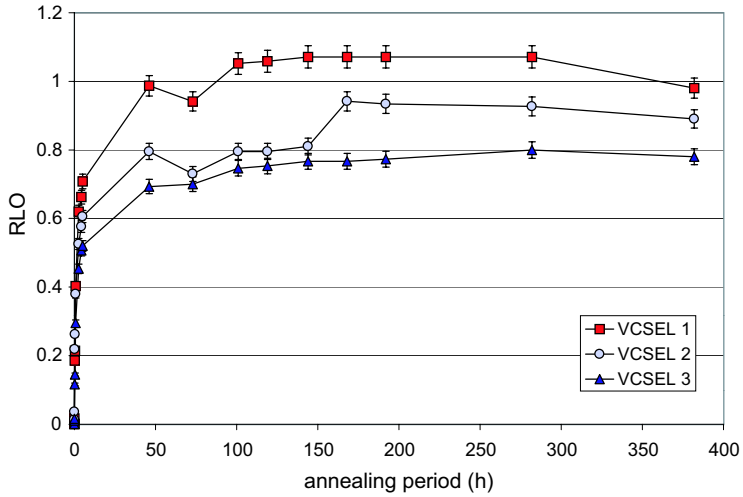

Figure 6.2: *Relative light output (RLO) of* VCSEL *group C which received a level of* $3{\cdot}10^{15}/cm^2$ *during the annealing period. At a drive current, the RLO increases to about 0.5 within a few hours. The RLO* > 1 *for* VCSEL *1 is explained by a poorly polished fibre used with this device for the pre-irradiation measurements.*

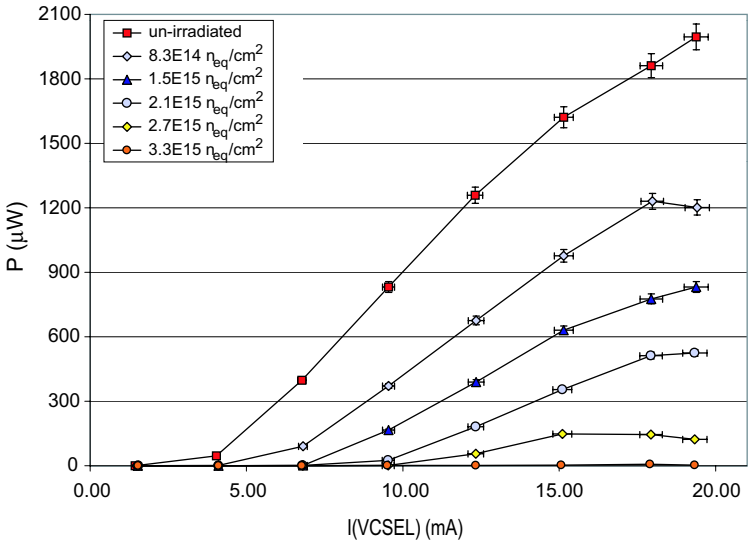

Figure 6.3: *LI curves of one sample Truelight VCSEL in a Taiwan package during the irradiation at T7. The threshold increases during the irradiation to values >20 mA. Only a few points were measured each time in order to keep the time out of the beam short.*

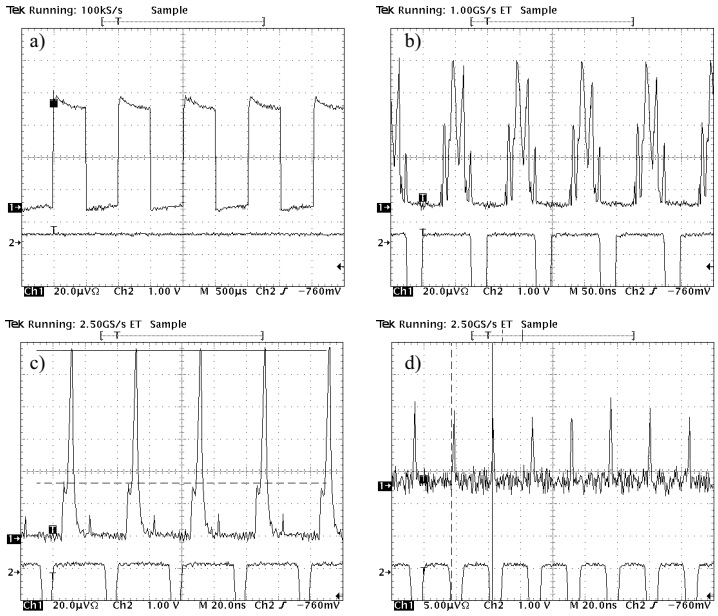

Figure 6.4: *Hardcopies of the light signal of irradiated* VCSELs*: a) 1 kHz, b) 1 MHz, c) 25 MHz, and d) 40 MHz.*

the VCSELs irradiated under bias noted above. The LI-curves measured after a fluence of $2.1{\cdot}10^{15}$ n_{eq}/cm^2, which is about the level expected for PP0, show that the VCSELs are degraded, but still operational. At fluences greater than $2.1{\cdot}10^{15}$ n_{eq}/cm^2 the light output power was at a very low level, indicating that the laser thresholds were shifted to values above 20 mA. Therefore, to avoid damaging the laser, a current of >20 mA was never again applied .

After the irradiation the devices and the supporting structure were highly activated and had to be stored un-powered for about six weeks. First tests in the laboratory showed that annealing due to thermal effects had already taken place during this period. The measured light output at 20 mA DC was initially above 1 mW, but not stable. An exponential decrease within one minute down to a few μW was observed. Whereas when driving the same samples with a pulse generator at 1kHz to 1MHz, very slowly degrading, but significant signals were observed. When the frequency was increased, the signals became unstable and at the 25 MHz the quality of the signals decreased significantly. The hardcopies of the optical signal in Figure 6.4, measured with an optical probe and an oscilloscope, show this behaviour: Hardcopy a) depicts the clear signals at 1 kHz, b) the degraded signal at 1 MHz. The hardcopy taken at 25 MHz (c) shows the described signals of poor quality, however very short spikes exhibit a relatively high light output. At 40 MHz (d) only small spikes appear. The difference between the DC and high frequency measurements could be explained by a device heating effect. At lower frequencies, the amount of time that the VCSEL was off was long enough to allow for cooling and the device is not heated enough to observe this effect; only on a much longer time scale (order of hours). At higher frequencies

and DC measurement this is no longer the case and heating can take place. A heating effect can arise when the current confinement layer is missing or defective. The radiation induced damages could have changed the doping concentration in such a way that the confinement layer becomes partly conducting and the current confinement is lost. The growing disparity between electrical power input and laser power output, due to the reduced efficiency, also leads to greater thermal effects at a given operating current.

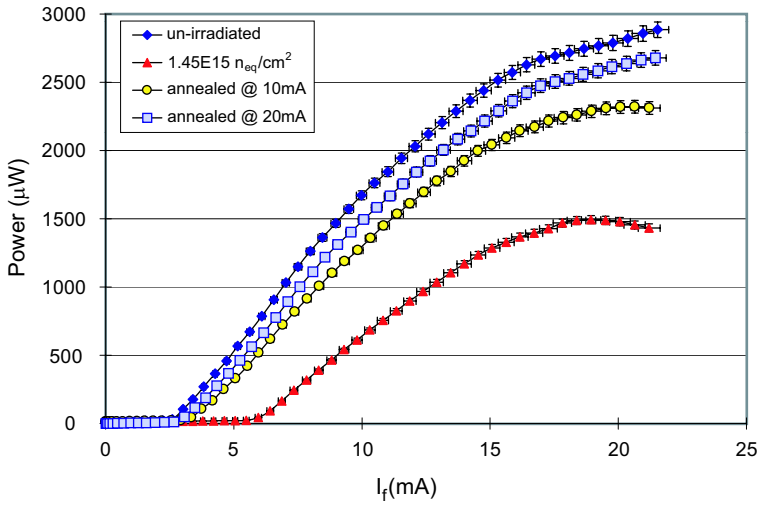

Figure 6.5: *LI curves of one sample Truelight* VCSEL *before the irradiation, after the irradiation and after annealing with 10 mA and 20 mA.*

Comparison of the LI-curves of the VCSELs irradiated with $1.5{\cdot}10^{15} n_{eq}/cm^2$ in the 24 GeV proton beam (triangles in Figure 6.3) to those with the same 1 MeV equivalent fluence in the 30 MeV proton beam in Taiwan (triangles in Figure 6.5) show that in both cases the threshold current rose to about 7 mA and the light output droped to about 50% of the pre-irradiation value. Apparently the VCSELs exhibit the same degree of degradation at this radiation level. This demonstrates, that the radiation damage of VCSELs (mainly GaAs) scales with NIEL. Table 6.1 gives a summary of VCSEL irradiation conducted to estimate bulk damage and the resulting degradation of these devices during 10 years of operation within the LHC environment. Further irradiations with gammas up to 60 MRad proved the radiation hardness regarding ionising doses [70].

6.4 Accelerated Lifetime Studies of VCSELs

In general, high temperature testing is used to determine semiconductor devices lifetimes, even though laser diode failure mechanisms are more sensitive to increases in current density. As a measured parameter of degradation, the current density is of great significance when searching for failure modes in a laser diode. Raising the current density however, is not really indicative of lifetime since it is more likely a situation to be avoided than one

VCSEL type	applied fluence n_{eq}/cm^2	particle source	annealing status
Mitel	$4{\cdot}10^{14}$	1 MeV n	ok
Mitel	$8{\cdot}10^{14}$	1 MeV n	ok
Mitel	$1{\cdot}10^{15}$	30 MeV p	ok
Mitel	$3{\cdot}10^{15}$	1 MeV n	ok
Truelight	$1.5{\cdot}10^{15}$	30 MeV p	ok
Truelight	$5.7{\cdot}10^{15}$	24 GeV p	ok at low freq.

Table 6.1: *Summary of VCSEL irradiations conducted to estimate bulk damages and the resulting degradation.*

that simulates normal lifetime degradation. The reliability of semiconductor sources is very dependent on the degradation modes.

Laser diodes are temperature sensitive when considering overall lifetime. For example, operating a laser diode at 10°C higher than rated will halve the life of the diode. Furthermore, a laser usually will stop functioning at 100°C. The degradation modes that result in failures or gradual degradation of these devices can be modelled using the Arrhenius relationship.

The Arrhenius model is often found to fit well the temperature dependence of the lifetime of semiconductor devices including lasers. Since many physical mechanisms leading to the degradation of lasers, including impurity diffusion and electro-migration, inter metallic component formation, and defect formation, multiplication and propagation, often follow an exponential temperature dependence, the functional form of the Arrhenius model is as follows [71],

$$MTTF(T) = C \exp(\frac{E_A}{kT}) \tag{6.7}$$

where $MTTF$ is the mean-time-to-failure, C is a constant, E_A is the activation energy, and kT is the thermal energy. The higher the value of E_A is, the more sensitive $MTTF$ is to operating temperature. The Arrhenius model is useful in calculating the device lifetime at normal operating temperature from a single extrapolation of data collected at an elevated temperature.

Besides radiation induced damage, the irradiated VCSEL will degrade due to the processes described above, resulting in DLDs (Dark Line Defects), which appear as dark lines in the light spot under strong enlargement. They are generally not observed with irradiated devices. The difference between radiation damages and operation damages can be explained as follows: Radiation damages are produced throughout the bulk and therefore are homogeneously distributed over the entire layer structure. Furthermore, these kind of damages are introduced any time independent of the laser operation condition. DLDs which result exclusively from the operation of the VCSEL are only formed on already existing defects or impurities. Therefore these are competing mechanisms. The operation of the device limits the lifetime but at the same time anneals the radiation induced damages [67- 69].

The growth of DLDs is enhanced by higher temperatures (higher currents). The acceleration model determined from reliability studies [71] is the Arrhenius relation (Equation 6.7) multiplied by a power–law current factor. This current factor is required to account for the effects of the operating current on the reliability. The acceleration model is given in terms of operating current I_{fi}, junction temperature T_i (in K), Boltzmann constant k, and activation energy E_A.

$$AF = \frac{MTTF1}{MTTF2} = \left(\frac{I_{f2}}{I_{f1}}\right)^n \cdot e^{\frac{E_A}{k} \cdot \left(\frac{1}{T_1} - \frac{1}{T_2}\right)} \tag{6.8}$$

The acceleration factor AF gives the ratio of mean-time-to-failure under two different operating conditions. In this relation, index 1 represents the parameters in the ATLAS Pixel Detector and index 2 represents the parameters during the lifetime tests in the laboratory. The activation energy is the energy that is needed to displace a defect in the lattice. For semiconductor lasers, a commonly cited value for E_A is 1.0 eV, which is used as the standard in MIL-STD-883B [72]. Extensive accelerated lifetime studies of un-irradiated devices by two manufacturers [71, 73] showed that the Arrhenius equation consistently describes the ageing of VCSELs.

Accelerated lifetime studies of irradiated lasediodes were performed with Mitel VCSELs which received a fluence of $4{\cdot}10^{14}$ n_{eq}/cm^2 at ISIS (group A). The devices were operated in two groups of 10 VCSELs each with currents of 20 mA and 25 mA at an accelerating temperature of 40°C. In the ATLAS Pixel Detector a nominal forward current of 10 mA and temperatures between -5°C and +20°C are foreseen. The temperature is not defined for the final design. Due to the increased temperature and current during the test the lifetime of the VCSELs is accelerated.

During the test period of 38 days, no VCSEL failed; a failure is defined as a drop in the light output of -3 dB. LI-curves after the tests showed no decrease of the light output. Since no failure was observed, the lifetime cannot be directly derived. A maximum failure rate can be calculated for the VCSELs for the operation in the ATLAS Pixel Detector. In order to calculate the simulated LHC years one has to take into account, that LHC will only operate for approximately a third of a year, the numbers of logical 1s and logical 0s are equally distributed and the VCSEL ages only when operated an additional. Therefore an acceleration factor of 12 is taken into account.

Assuming a Poisson-like failure rate distribution, the maximum failure rate p is ([91]):

$$p = \left(\frac{1}{n}\right) ln \left(\frac{1}{1 - C(0)}\right) \tag{6.9}$$

where n is the number of tested devices and $C(0)$ is the confidence interval around 0. This failure rate must be extrapolated to the ATLAS Pixel Detector operating conditions and the acceleration factor must be taken into account.

The 90% confidence level upper limit of fraction of VCSELs that could fail in 10 years of operation can be calculated with the following equation:

$$M = 10 \cdot VCSELs \cdot \frac{p}{a} \tag{6.10}$$

The term "a" denotes the number of simulated ATLAS years. Table 6.2 summarises the simulated LHC years for different current conditions and the maximal failure rate for the combination of these results.

Ambient temperature [$°C$]	simulated LHC years		maximal failure rate in %
	20 mA	25 mA	
- 5	3100	4850	$\leq$0.1
0	1400	2190	0.2
5	653	1020	0.3
10	312	488	0.7
15	153	239	1.5
20	77	120	2.8
40	6	10	35

Table 6.2: *Simulated LHC years and maximal failure rate (90 % C.L.) for different temperatures. At an ambient temperatures 20°C a maximum of 50 optical links could loose a VCSEL and therefore the data of this module would be lost. In case of no cooling high temperatures as 40°C would easily be possible and this would lead to a failure rate of up to 35%.*

The results of the lifetime study with Mitel VCSELs yield a maximum number of 0.1% of devices which could fail, when the ambient temperature is -5°C. Because the position of the optical link and therefore its temperature is not yet finalised, the data was used to give the failure rate for higher temperatures. For an ambient temperature of 5°C, 0.3% of the VCSELs could fail. In the case of no cooling, or a failing cooling system, temperatures as high as 40°C would easily be possible and this would lead to a failure rate of up to 35%, or more than 700 modules which can not be red out anymore.

6.5 Conclusions

The VCSELs in the ATLAS Pixel Detector will degrade due to normal operation and irradiation induced damages. The radiation tolerance studies of similar proton implanted VCSELs showed that the optical output of devices will decrease while the laser threshold will increase with rising fluence. VCSELs which were irradiated with intermediate annealing periods showed good recovery behaviour if an annealing current of at least 10 mA was applied. In case of a higher current the annealing is faster and a higher light output can be achieved. However, a maximum of 20 mA should not be exceeded to avoid damaging the laserdiode. During LHC operation, intermediate annealing sessions, for example during shut-down, would help to keep the radiation induced damage at a low level. The highest accumulated fluence was about a factor 3 more than the expected fluence at the radius forseen for the positioning of the on-detector optical link components. LI-curves measured during this irradiation at CERN show that, after a fluence comparable to the expected

PP0 fluence, the VCSELs were operating with an increased laser threshold exhibiting a significant light output. A comparison of the behaviour of VCSELs irradiated up to the same fluence with protons of different energies (expressed in 1 MeV equivalent neutrons) proves that the NIEL scaling is also applicable to VCSELs. Accelerated lifetime tests of Mitel VCSELs predict a loss of VCSELs between 0.1% and 35%, strongly depending on the ambient temperature in the experiment cavity. In order to minimise the possible failure rate, a temperature of $(0 \pm 5)°C$ is desirable.

Chapter 7

Optical Packages

In this chapter the different packaging possibilities of the optoelectronic devices for the on-detector and off-detector are described. All three candidate optical packages for the on-detector optical link were qualified.

7.1 The On-detector Optical Package

The chosen emitter (VCSEL) and receiver (PiN photodiode) for the on-detector side must be specially packaged and coupled to the fibres. This optical package must comply the following requirements:

- radiation hardness
- non magnetic materials not to compromise the magnetic field in the Inner Detector
- low Z material to avoid large radiation length
- low cost.

Common industrial VCSEL or PiN packages are not suitable for the ATLAS Detector because most of them include the driver electronics, fabricated in common CMOS processes which are usually not enough radiation tolerant. The extreme lack of space also prevents the use of an industrial standard connector. A custom made package with the fibres directly attached to the optoelectronic components is necessary. Three different designs for this housing were studied. All of these are low mass, non-magnetic and radiation tolerant packages for two (one) VCSEL and one PiN photodiode. Footprint and size are similar. The three candidate packages are the so-called Marconi package, the OSU package and the Taiwan package.

7.1.1 Specifications for the On-Detector Package

Important parameters are defined for the VCSELs, the PiN photodiodes and for the environmental and radiation conditions for the optical package. Table 7.1 summarises the

parameters essential for good performance of an optical package. The complete specifications for the optical links of the SCT and Pixel detector can be found in [74]. The chosen values for the various parameters take into account the expected radiation damages in all components, the attenuation of the signal due to connectors and the speed of the attached electronics. Vital parameters are the VCSEL light output and the responsivity of the PiN photodiode. These parameters are influenced by the alignment of the fibres with respect to the optoelectronic device; therefore, tight alignment tolerances when placing the fibre in respect to the VCSEL are given. Since the core of the fibre and the VCSEL diameter are of the same size ($\sim 50\mu$m), and because of the Gaussian shape of the light cone, a displacement of a few micrometers result in a high signal attenuation. The alignment of the fibre with respect to the PiN photodiode is not as crucial due to the larger size of the photodiode ($\sim$350 μm). Nevertheless, a bad alignment can also result in a low responsivity. The different package designs can be categorised as "active alignment" and "passive alignment" packages. The active alignment needs a positioning of the fibres with respect to the VCSEL and/or PiN during a late stage in the package production, whereas a passive alignment package is machined in such a way that the fibres can be attached to the optoelectronic devices without further adjustment. The following packages represent both types of alignment.

Another important criteria is the device reliability. The device reliability unit is Failure in Time (FIT) and is defined as the number of failures in 10^9 operating hours. The FIT numbers given in Table 7.1 are calculated to allow for up to a 1% failure rate over the lifetime of ATLAS (10^8 seconds). VCSELs are only "on" while sending 1s which is for 1/4 of the LHC time, assuming 50% utilisation of the bandwidth and sending equal numbers of 0s and 1s. The PiN photodiodes will be continually biased.

	Parameter	**Min.**	**Typ.**	**Max.**	**Units**	**Notes**
Packaged VCSEL	Wavelength	820	840	860	nm	
	Optical Output after irradiation	300			μW	@I_f = 10 mA
	Threshold current	2	3	6	mA	
	Device reliability		1400		FIT	FIT=failures in 10^9h
Packaged PiN	Wavelength	820	840	860	nm	
	Input saturation power	3			mW	@I_f = 10 mA
	Responsivity after irradiation	0.25			$\mu A/\mu W$	
	Rise/fall time		≤ 1	2	ns	
	Device reliability		360		FIT	FIT=failures in 10^9h

Table 7.1: *Specification for the* VCSEL *and PiN photodiodes package in the on-detector optical housing [74].*

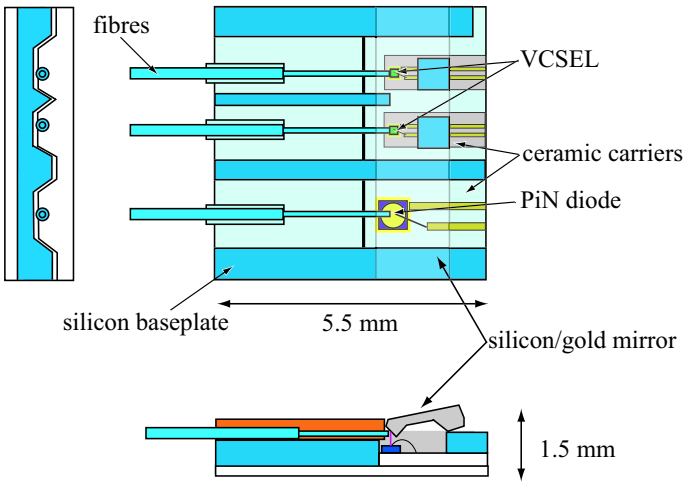

Figure 7.1: *The Marconi Package. Two* VCSEL *emitters and a PiN photodiode are housed in a low mass, radiation tolerant silicon/ceramic package. Fibres attached to the package lid are pigtailed directly to the components with the aid of a gold-coated silicon mirror [75].*

7.1.2 Marconi Package

The Marconi package was developed by Marconi in England[1]. The package is square with sides of 5.5 mm and is 1.5 mm high. The VCSELs and PiN photodiodes are mounted on ceramic carriers, which are placed into a silicon base structure at the necessary heights, considering the height difference of PiN photodiode and VCSEL. The silicon structure also provides a well in order to minimise cross-talk from the VCSELs to the PiN photodiodes. The light is coupled into the fibres over a 45° silicon mirror, which is sputtered with gold to gain better reflectivity. The fibres are located in v-grooves etched into a silicon lid and protrude about 300 μm to stick under the mirror when the lid is placed onto the package. Lenses are unnecessary with this kind of coupling. The v-groove lid fits well into the opposite v-grooves in the silicon base structure; alignment is automatic. This passive alignment package, depicted in Figure 7.1, gave encouraging results in the first tests.

A batch of 66 of this package was assembled of which 60 satisfied the ATLAS specifications. The mean responsivity of the PiN diodes was 0.49 A/W. The distribution of fibre coupled power is shown in Figure 7.2.

7.1.3 OSU Package

The package developed at The Ohio State University (OSU) is a passive alignment package based on a connector concept. It consists of a base which holds the VCSELs and PiNs, and a cap with three holes for the fibres. The cap with the fibres is placed onto the base at a very

[1] produced by Marconi Material Technology Caswell, Towcester, U.K

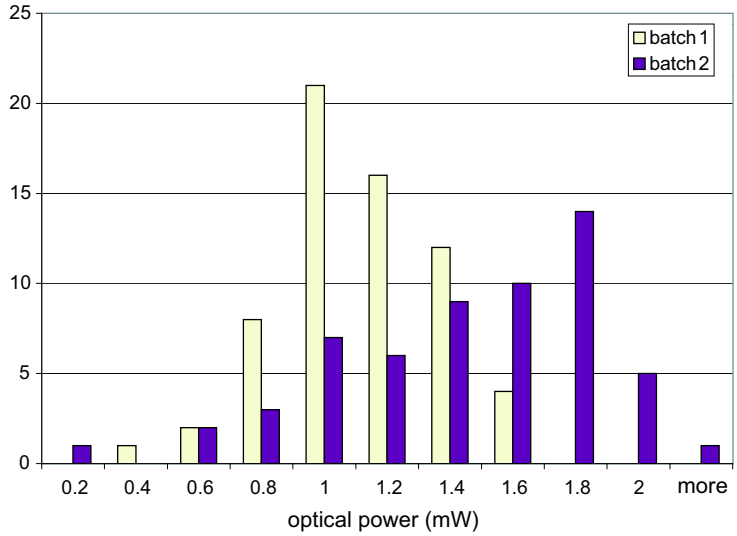

Figure 7.2: *Distribution of fibre coupled power for* VCSELs *driven at 10 mA in the Marconi package [76].*

late stage in the production in order to ease the handling. Figure 7.3 illustrates this design. The base with the VCSELs and PiNs is depicted on the left side. The electrical connection from the optical devices to the driver chips is accomplished via gold tracks and wire bonds. The base material is alumina, which was chosen because of its smooth surface [77]. The cap holds the three fibres in position. The cap functions as a connector which can be taken off after testing the package and placed back onto at a later stage of the Pixel Detector production. The cap material is Ultem (polyetherimide), a mold-injectable plastic with a radiation tolerance of 10 GRad. A different version of this package, which holds only one

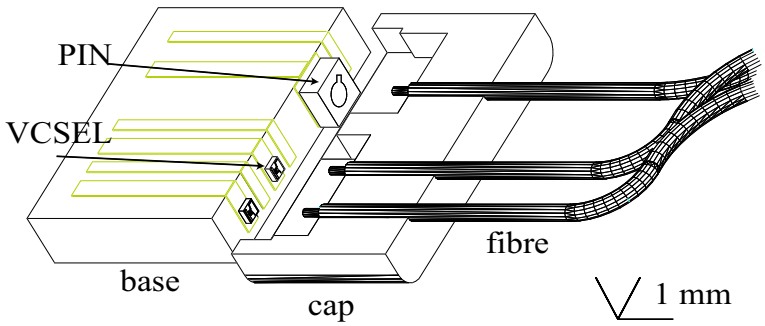

Figure 7.3: *A cut out view of the OSU optical package showing the two* VCSELs *and one PiN photodiode mounted on the base on gold pads which are connected to the gold traces. The cap holds the cleaved fibres into position [77].*

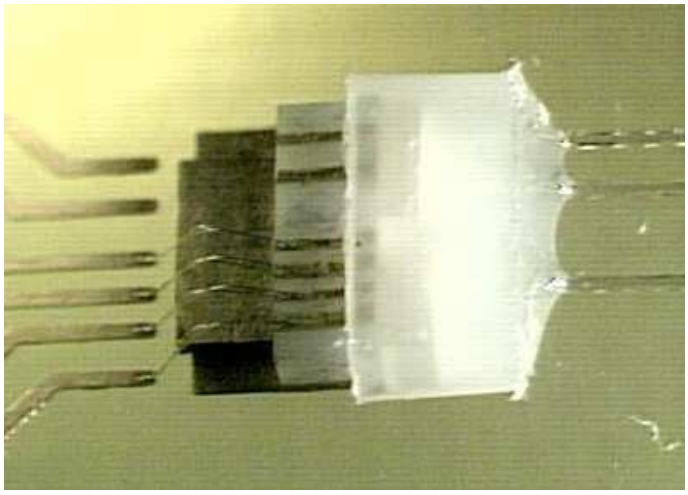

Figure 7.4: *The OSU Package with the cap attached to the base. This version contains 2* VCSELs *and one PiN photodiode.*

VCSEL was also designed. LI-curves of some packages are depicted in Figure 7.5. Three of the five samples meet the specifications. As it turns out, the small cap is not passively aligned. The highest light output can only be achieved by aligning the cap while checking the power. This might be improved by elongating the base and cap to increase the guidance length for the cap.

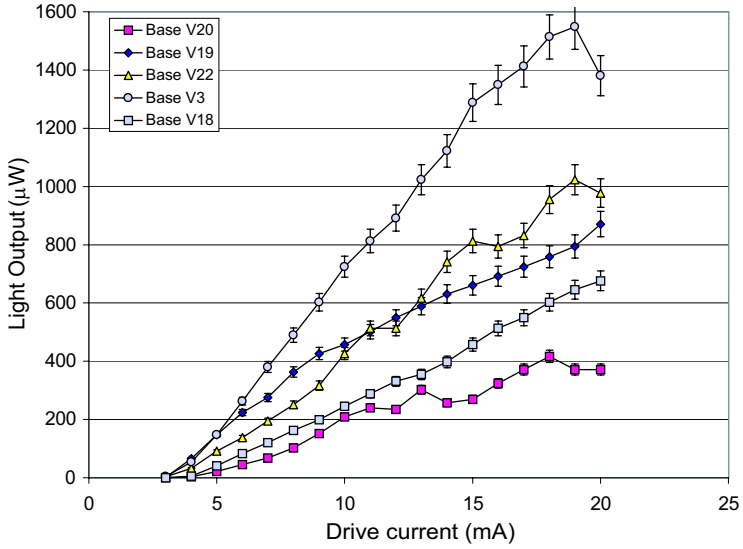

Figure 7.5: *LI-curves of* VCSELs *packaged in an OSU Package. Three of the five samples meet the specifications.*

7.1.4 Taiwan Package

This package was designed at the Academia Sinica (Taipei, Taiwan). Figure 7.6 depicts a schematical drawing of the Taiwan package. The optical coupling design is based on a 45° mirrored direct coupling. Bare fibres are polished to 45° on one end before alignment. The optical power is coupled from the un-polished side and totally internally reflected to the core of the fibre by the 45° polished surface.

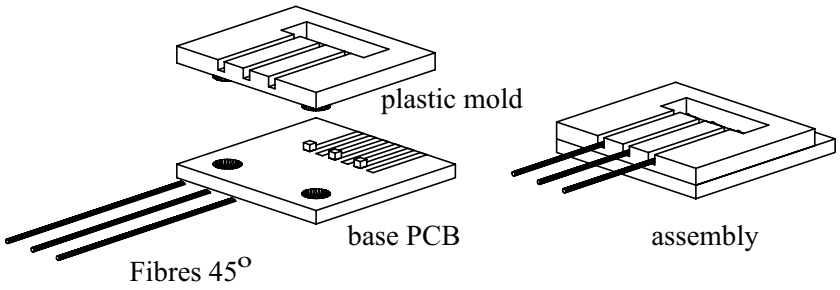

Figure 7.6: *Drawing of the Taiwan Opto-Package in part and assembled ("2+1" version).*

The package is made of two pieces of PCB and molded plastic. The lower PCB, called "base PCB", is used to hold all opto-electronic devices. The copper traces on the base PCB provide mounting pads and the electrical connection for the VCSELs as well as for the PiN photodiode. The top side of the VCSEL or PiN is connected via wire-bonds. The plastic part is used as spacer for holding bare fibres a distance from the base PCB. The difference in height between the VCSEL an the PiN photodiode is considered in the molded plastic. A second thin PCB layer is placed on top of the build up plastic to cover the components [78]. The overall package is approximately square with sides of 5.5 mm and is 1.5 mm high. This version of the package is called "2+1" since two VCSELs and one PiN photodiode are packaged. One sample package, before the cover is placed on, is depicted Figure 7.7. It is forseen for the use in the SCT optical links system. The possibility of making different versions is described later in this section.

Tests of the Taiwan Package

The "2+1" version of this package was used during a barrel harness test of the ATLAS SCT. Six of these packages were received on a test PCB. Short tests of the optical output and the PiN responsivity showed that all packages meet the specifications necessary for good performance during the experiment (Table 7.1). After attaching theses packages and the necessary DORIC4a and VDC to individual flex kapton structure[2], five thermal cycles between +20° and -20° were applied overnight to detect faulty wire bonds. The wire-bonds remained intact.

[2]kapton support structure for the SCT optical link, also carrying the power and control voltages for the module and optical link

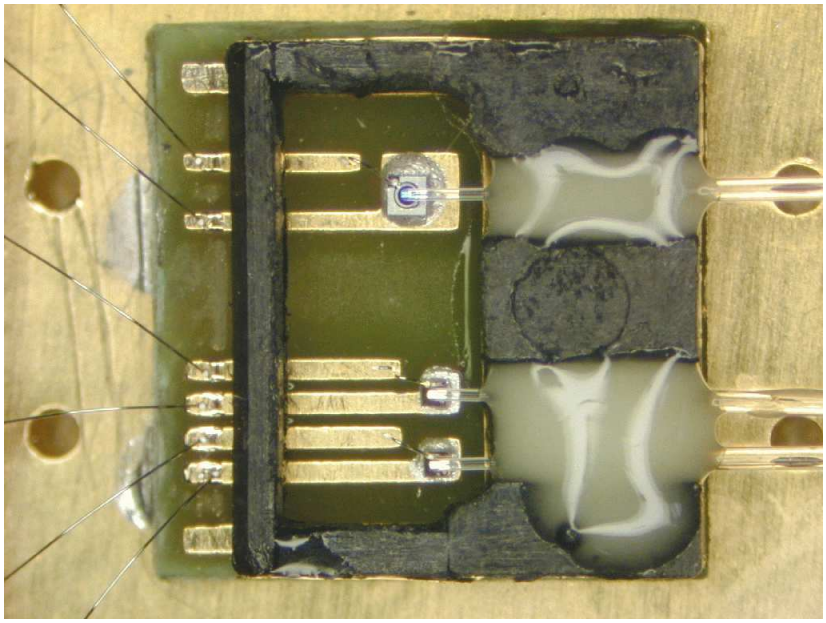

Figure 7.7: *Picture of the "2+1" Taiwan Opto-Package before the cover is placed on.*

For a complete test of a SCT barrel harness, the "doglegs" were mounted on a test structure for mechanical support and connected into a group of six. The single fibres were bundled and ribbonised for better handling. Figure 7.8 depicts this support structure with the doglegs. In order to test the functionality of the Taiwan packages on the dogleg, the bit error rate (BER) versus the optical light input in the packaged PiN photodiode was scanned. Figure 7.9 shows the plot of the scan of all six doglegs. The scans were repeated with the VCSEL directly beside the PiN turned on or off. A difference in these two scans would indicate cross-talk picked up in the package. No cross-talk was observed.

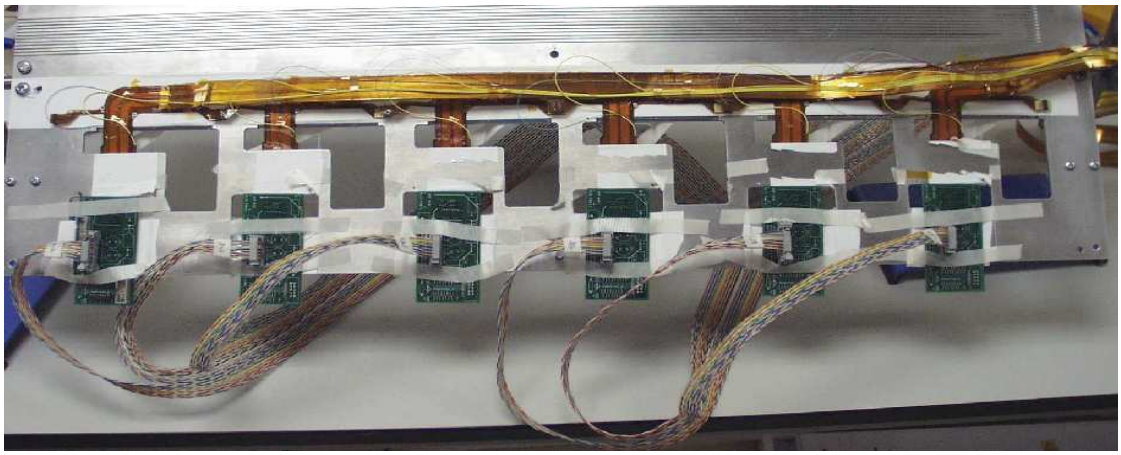

Figure 7.8: *Six doglegs on a test support structure*

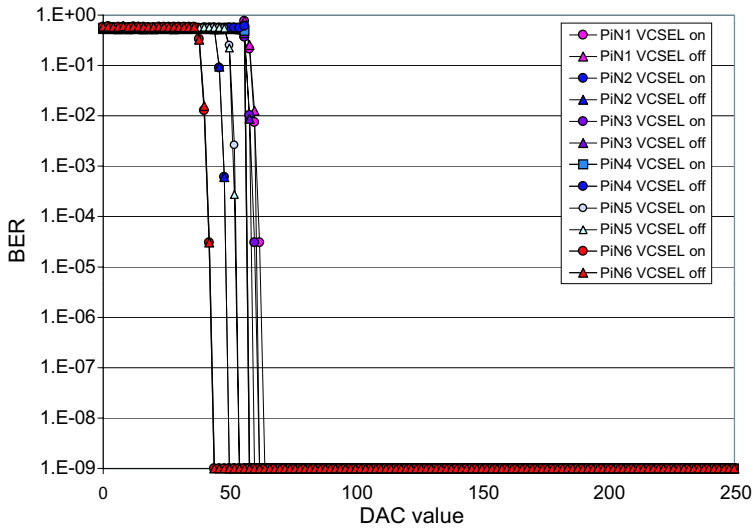

Figure 7.9: *BER versus optical light input for six Taiwan packages in a* SCT *harness.*

Modification Possibilities

The simple design of the Taiwan package allows for modifications on a short time scale. Given this, improvement of the optical link was attempted. Another way to design the optical link to use packages which hold only one kind of optical device in order to separate the TTC link from the data link. If both directions are separate, the routing of the fibres can be simplified and the danger of cross-talk minimised. For this purpose, the "2+1" design had to be modified. The base PCB was widened enough, to hold up to eight optoelectronic devices. Two different plastic molds were necessary in order to meet the different heights of the devices. All other parts are the same for both package types (TTC and data) and can be fabricated in one batch.

This prototype was produced in Taiwan. Figure 7.10 shows a photograph of one prototype with eight VCSELs. The 45° polished fibres are attached as single fibres, but the use of eight way fibre ribbon is also possible. The LI-curves of all VCSELs in one package are shown in Figure 7.11. The light output at 10 mA is greater than 300 μW for all eight VCSELs. This shows that even with a greater number of VCSELs in a package "homogeneous" light output is possible.

7.1.5 Choice of Optical Package

It is essential to have a unified design for all optical links within the ATLAS Pixel Detector, thus only one package type was chosen for use within the ATLAS Pixel Detector. Although all three package types proved to be acceptable by meeting the minimum requirements (Table 7.1), they were not equally easy to use.

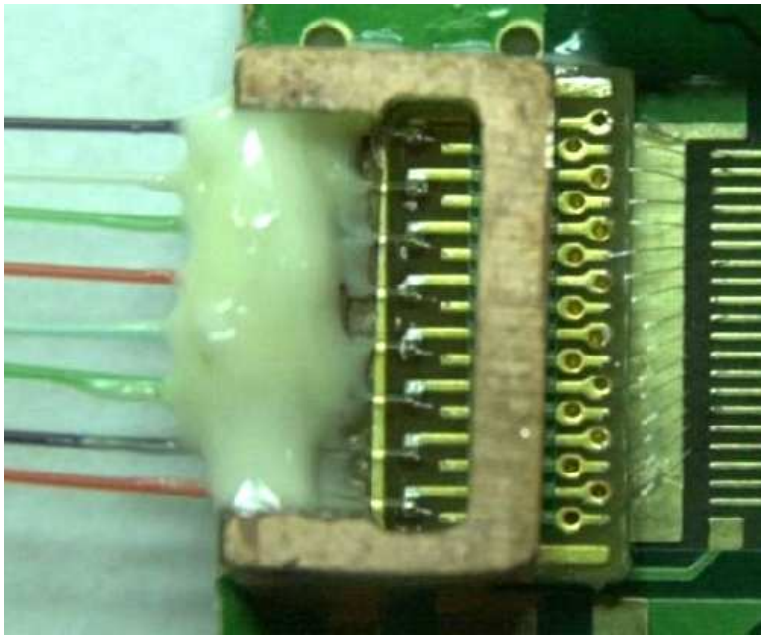

Figure 7.10: *Picture of the "8x1" Taiwan Opto-Package before the cover is placed on.*

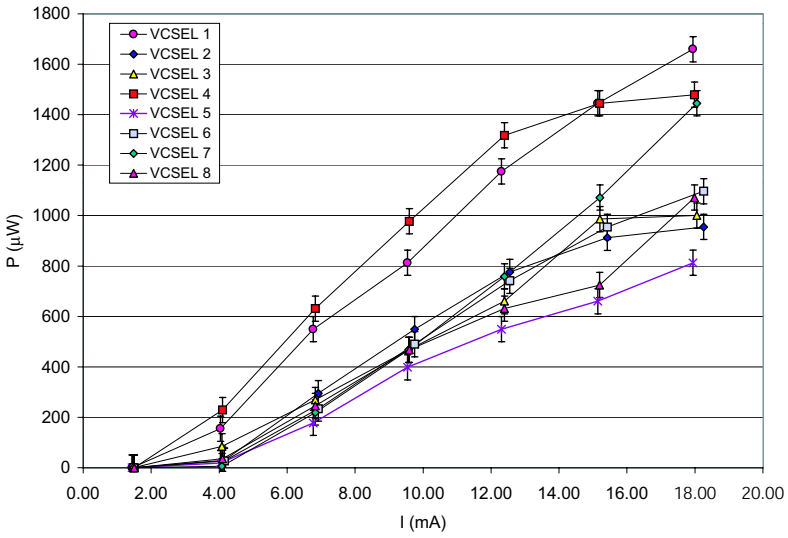

Figure 7.11: *LI-curves of eight* VCSELs *in a "8x1" Taiwan package. All* VCSELs *meet the specifications.*

	Parameter	Min	Typ	Max	Units	Notes
Packaged VCSEL	Wavelength	820	840	860	nm	
	Optical Output	1	2		mW	coupled into 50μm core fibre @20 mA
	Threshold current		3	6	mA	
	Device reliability		500		FIT	
	Temperature Range	10	20	50	°C	
	Rise/fall time		≤ 1	2	ns	
Packaged PiN	Wavelength	820	840	860	nm	
	Input power	3			mW	
	Responsivity	0.4	0.5		A/W	@820 - 860 nm
	Rise/fall time		≤ 1	2	ns	

Table 7.2: *Specification for the off-detector* VCSEL *and PiN photodiodes package in the off-detector optical housing [].*

Use of the Marconi package was discontinued because of the complicated attachment of the lid, and the high price per device. The placement of the cap onto the base of the OSU package proved to be more demanding than expected, whereas the Taiwan package was straightforward in use and active alignment of the fibres resulted in a higher VCSEL light output or PiN responsivity; thus the Taiwan package was chosen as baseline for the Pixel Detector optical link system.

7.2 The Off–Detector Packages

The off-detector receiver and emitter will be positioned on the Read Out Driver (ROD, Section 3.3). The demands on these packages are not as great as on the on-detector packages, for example, they are not in a radiation field and therefore radiation hardness is not a consideration. However, there are strict specifications since the VCSEL and the PiN diode must fit the on-detector emitter and receiver. The output of the TTC signals and the input of the data stream are separated on the ROD, therefore, separate packages with either PiN photodiodes or VCSELs are necessary. Due to space constraints packages with 4, 8 or 12 devices are desired.

The VCSELs work as transmitters of the Timing Triggering and Control Signals (TTC) and the PiN-photodiodes work as receiver of the data. Since they will be one piece in a chain of components, there are some specifications they have to meet. The VCSEL arrays must work at a wavelength of 850 nm. For the transmission of data over a distance of more than 100 m an output power P_0 of more than 1 mW at 20 mA drive current is necessary. Both arrays should have common cathodes and individual anodes. More specifications are listed in Table 7.2

7.2.1 Packaging Specification

Due to space constraints in the RODs it is necessary that the VCSEL and PiN photodiode arrays have an integral MT12 socket with alignment pins. Their packaging should be suitable for surface mounting close to the board edge with the fibre approaching in a plane, parallel to the board and perpendicular to the board edge. The footprint of this package should not exceed 10 mm by 12 mm, where the 10 mm is along the board edge. The height of the package should not exceed 12 mm. There should be adequate means of retaining the mated fibre. The mechanical strength, including the surface mounting, should allow trouble-free installation, with the possibility of at least 10 connect-disconnect cycles. The package should be adequately screened to keep electrical pickup down. Ideally this screening should be separate from the common cathode. Failing this separation, it would be of benefit if the screen were coated with an insulator. Optical cross talk should be less than 13 dB and ideally less than 20 dB. The electrical cross-talk will depend on both the PiN array and the environment in which it is to be used. The inter-stream capacitance of the PiN array should be minimised by design.

An official CERN market survey showed that the market of such devices is very small. Most industrial components include driver electronics which do not meet the ATLAS specifications. A possible solution was prototyped in Taiwan, showing promising results during first tests.

7.3 Conclusions

In this chapter the difficulties of integrating optoelectronic devices in radiation tolerant non-magnetic packages with direct fibre coupling are described. The qualification of three candidate packages showed that different designs are feasible. The better test results of the active alignment led to the choice of the so-called Taiwan package. The off-detector side package also has to be a custom made package since no commercial parts meeting the special requirements are available.

Chapter 8

Driver and Receiver Electronics

A number of electronic chips is required to run the complete optical link. Different ASICs for the on- and off-detector side, introduced in Figure 3.12 are described in this chapter, pointing some of the differences between the Pixel and SCT chips. First studies have been performed on the effect of radiation on the Pixel optical link ASICs.

8.1 The On–Detector Electronics

The VCSEL Driver Chip VDC and the Digital Optical Receiver IC DORIC are the ASICs to drive the on-detector optical link, translating LVDS signals into drive current for the VCSEL (VDC) and small photo-currents into LVDS signals (DORIC). The on-detector ASICs for the SCT have been designed in a nominally radiation-soft process – the AMS 0.8 μm BiCMOS process. Since this process is not a common radiation hard process, special care was taken in both the circuit design and layout to minimise the effects of radiation damage [79, 48]:

- using bipolar npn transistors only,
- operating the transistors with relatively large currents such that the DC current gain β is large and less sensitive to radiation damage,
- using a design in which the circuits are very insensitive to changes in β.

The expected radiation level within the Pixel Detector is much higher than in the SCT (Section 4.3). Therefore the use of the same ASICs is not forseen and the DMILL[1] process was chosen for the first prototypes. This is a BiCMOS process with a radiation hardness of up to 10 MRad total dose, respectively a particle fluence of 10^{14} n_{eq}/cm^2, guaranteed by the manufacturer. The DMILL process allows the use of nmos-, pmos-, npn-bipolar-, and pjfet-transistors. Each unit is isolated from the substrate by a SiO_2-layer (silicon on insulator, SOI) [81]. In order to have all electronics manufactured in the same technology, the opto-electronic chips were also submitted in a Deep Submicron Process (DSM), as the FE-electronics. The design of the Pixel optical chips is a cooperation of the Ohio State University, USA, and the Siegen University in Germany [82].

[1] Durcie Mixte sur Isolant Logico-Lineaire

Nevertheless, the principle functionality of the optical link electronics is the same for both ATLAS subsystems and differs only in details. The following descriptions of the ASICs are valid for both optical links, SCT and Pixel Detector.

8.1.1 The VCSEL Driver Chip

The VCSEL Driver Chip VDC translates LVDS data produced by the front-end output stage (MCC in the case of the Pixel Detector) into the drive current signal required to operate the VCSEL which is directly connected to the chip. The output driver produces a nominal 1 mA DC bias current plus a variable switched current. The amplitude of the switched current $I_{forward}$ can be set via an external control current I_{set} from 0 to 20 mA. The pre-bias current I_{bleed} is used to increase the speed of the VCSEL turn-on[2]. In the case of the SCT VDC the bleed current is produced by an internal 2.5 kΩ resistor close to the laserdiode cathode. The bleed current is independent of the control current I_{set} and measured to be 1 mA ± 0.05 mA. The SCT VDC has two identical circuits constructed on one substrate. The circuits are completely independent (apart from the common substrate) so one failed driver will not affect the other [79].

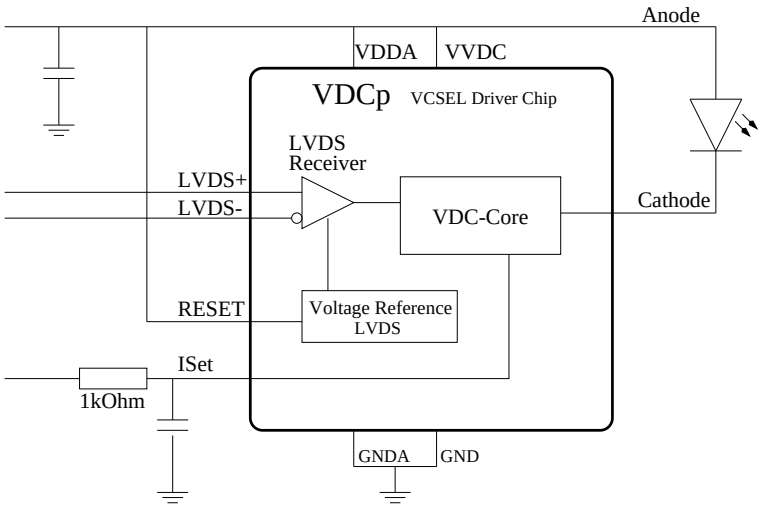

Figure 8.1: *Schematic and external circuitry of the* VCSEL *Driver Chip* VDC.

The Pixel VDC was designed in the radiation tolerant DMILL process to meet the required high radiation hardness. Resistors are not easily implemented in this process. Therefore transistors were used to realise the bleed current described above. In the two DMILL iterations of the VDC the bleed current depends on I_{set} due to imperfect matching in two transistors. With rising control current the bleed current increases. This could lead to problems since the bleed current can become larger than the threshold of the used laserdiode.

[2] $I_{forward}$ and I_{bleed} are also quoted as I_{bright} and I_{dim} respectively

The observed design problems within the DMILL chips were fixed for the DSM submission. Very first tests of this so-called VDC-I in July 2001 showed an independent I_{bleed} for most of the range of I_{set} as illustrated in Figure 8.2. The chip is also able to drive 20 mA through a VCSEL, a feature necessary for annealing sessions (Section 6.3). The rise and fall time of 1.0 ns ± 0.3 ns is also well within the specifications for this chip.

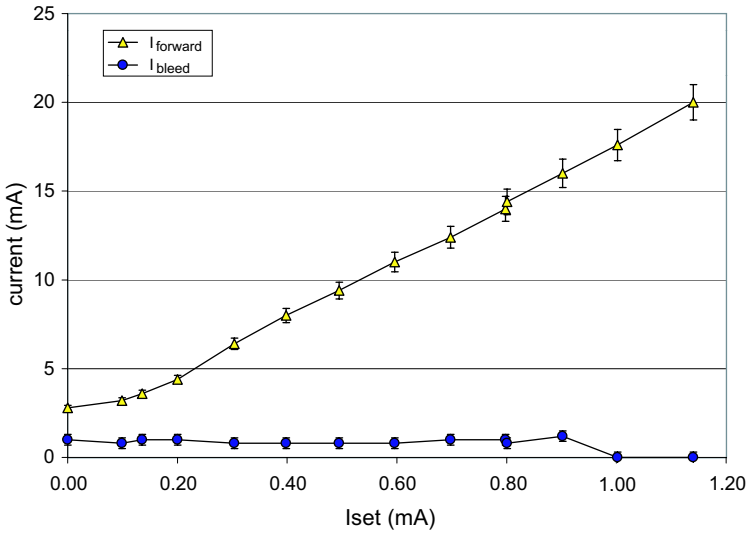

Figure 8.2: $I_{forward}$ *and* I_{bleed} *versus* I_{set} *measured at a* VDC-I *[84].*

8.1.2 The Digital Optical Receiver IC

The Digital Optical Receiver IC (DORIC) decodes the BPM encoded input data stream to recover the 40 MHz clock and 40 Mb/s control data stream (Figure 3.11). The device was designed for the use with a single photodiode receiving a BPM optical input signal. The output is in LVDS format. The DORIC also provides bias for the PiN photodiode. The circuit has been designed to function with an AC-coupled input signal amplitude in the range of 60 μA to 600 μA [86, 85]. The SCT DORIC circuit provides two copies of the output stream for the purpose of driving an additional detector module in case that its DORIC has become non-operational, therefore providing the system with a certain level of redundancy [86]. In the Pixel Detector optical link system it is not possible to integrate a redundancy because this would mean electrically connecting two modules.

The block diagram of the SCT DORIC4 is depicted in Figure 8.3. The according timing diagram of the signals within the DORIC is shown in Figure 8.4. The signal rows depict the timing at the different points in the circuit as marked on the block diagram. The PiN photocurrent is amplified and transfered into a LVDS signal within the input stage. The bandwidth of the amplifier has to be quite large in order to process variable signal sizes. A filter circuitry subtracts the standing current of the signal stream and supplies the PiN-

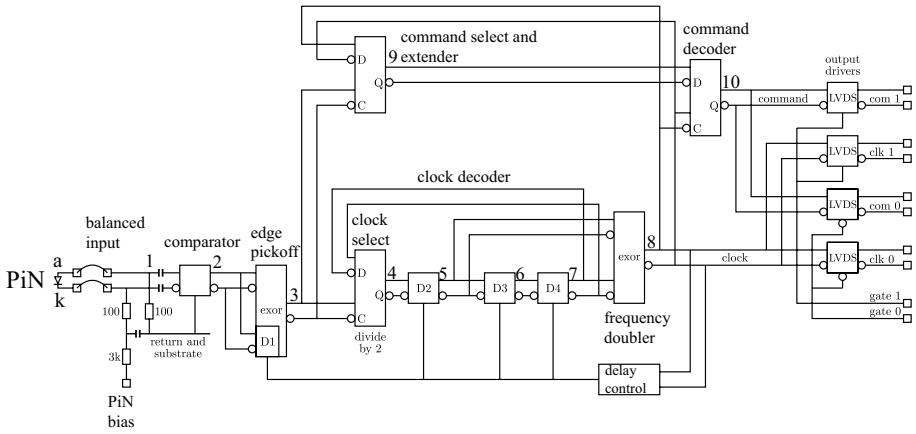

Figure 8.3: *Internal circuitry of the Digital Opto Receiver IC* DORIC*4 for the* SCT *[79].*

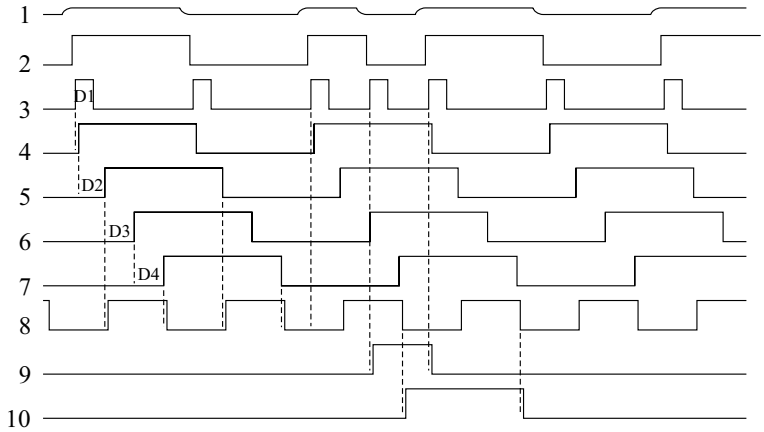

Figure 8.4: DORIC*4 timing diagram. The signals are shown at different points in the circuit as marked on Figure 8.3 [79].*

photodiode with the reverse bias V_{PiN}. An edge detector identifies the edges out of the amplified signal by splitting the wave leaving the comparator and delaying one arm within the edge pickoff by the time D1. Therefore there is always a D1 long signal if an edge within the original signal occurs (row 3).

The clock is decoded first and its duty cycle is adjusted to 50% by a delay-locked-loop (DLL). Three identical delay stages are used to produce the required total delay within the DLL. Outputs from intermediate stages are used for internal timing and gating functions. The frequency of row 7 is doubled within the frequency doubler with the use of the edge of signal 5. The delay between 5 and 7 is exactly 50 % of the duty cycle. The decoded clock is then used to detect and latch command signals. **The signals are delayed in such a**

way, that a positive edge in 3 is always coincidently with a “0” on signal 8. An additional edge on signal 3 simultaneously with a positive clock signal leads to a high output of the command select (row 9). The command decoder is used to prolong and synchronise the signal.

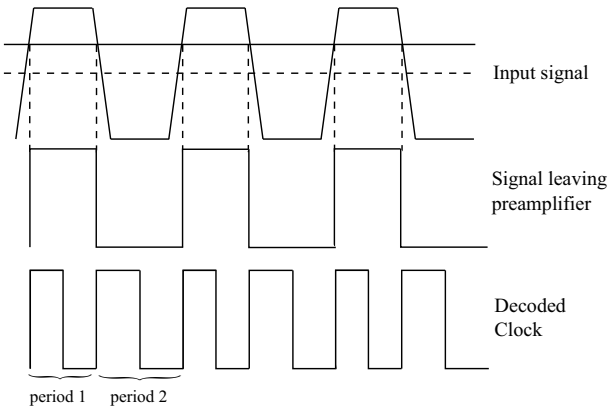

Figure 8.5: Effect of an asymmetric threshold on the signal leaving the preamplifier. The following decoder recovers two different families of periods.

Due to the AC coupling, noise could result in nonsensical signals while sending a zero. In the case of the SCT DORIC this is circumvent by an asymmetric threshold. But this again causes an asymmetric signal leaving the preamplifier and resulting in two families of clock periods after decoding. This effect is illustrated in Figure 8.5. A way to solve this is the introduction of a hysteresis circuitry which effectively sets the threshold to the 50% level of the input signal. The hysteresis current was chosen to be 10 μA. Bit error rate (BER) scans qualify the performance of the DORIC. The BER is defined as the number of corrupted bits per number of transferred bits. It is measured versus the mean current injected into the input stage. The threshold is given by the mean current at which the BER is $< 10^{-9}$. The measured threshold of the DORIC pre-amplifier is in the SCT case about 25 μA and mostly independent of the packaging of the chips and the distance between the chip and the photodiode.

In the case of the DMILL DORIC for the Pixel Detector the threshold varies quite strongly from chip to chip. In some cases the threshold is above the expected photocurrent during the experiment of 75 μA. This is due to a large pre-amplifier offset. It was also shown, that the threshold of this chip version is strongly depending on the distance between the chip and the adjacent photodiode. Best results were achieved when the DORIC and the photodiode were placed without housing directly onto a board. In Figure 8.6 different BER scans illustrate this behaviour. BER scan were performed for a DORICp-D2[3] packaged in a PLCC44 package with the PiN photodiode in a distance of 5 mm and the same DORIC type placed onto a PCB board and directly besides the PiN diode. A significant difference between the performance of both chips is apparent.

[3] 2^{nd} iteration of the DMILL DORIC

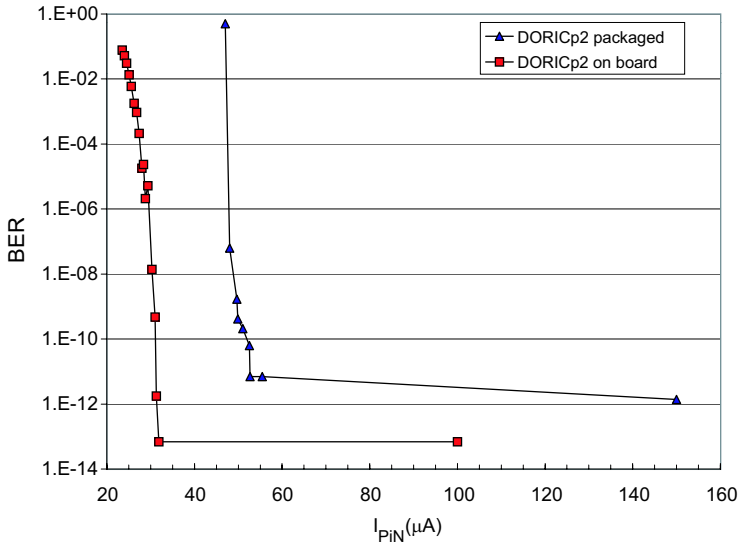

Figure 8.6: *BER versus mean photo-current for two* DORICp*-D2, one packaged in a PLCC44 package and one directly mounted on a PCB.*

Furthermore a clock jitter of 6 ns was observed with packaged DORICs, a problem not appearing when it is mounted directly onto a board and besides the photodiode. In the latter setup the jitter is less than 2 ns, which is within the specifications. This proves again, that the preamplifier is very sensitive to any noise. The DORIC should be placed directly to the PiN photodiode.

The observed design problems were fixed by the designers for the submission of the DSM process. For example a DC-feedback was introduced in the pre-amplifier to cancel the offset.

8.1.3 Radiation Hardness of the On-Detector ASICs

The SCT optical link chips have been proven to be radiation hard for the SCT environment [79]. Radiation hardness studies of the DMILL VDC for the Pixel Detector were performed at the 24 GeV PS proton beam at CERN. In the following the radiation level is expressed in MRad, as the ionisation damage scales with the total energy deposited by irradiation (Section 4.1). $3.6{\cdot}10^{13}$ $p_{24GeV}/cm^2 \simeq 1$ MRad [80]. For the B-Layer the expected total dose is 50 MRad whereas the total dose expected for PP0 is about 20 MRad. In a first radiation hardness study only the VDC was tested. Eight sample chips packaged and on special PCB boards[4] were positioned within a cooled test box, aligned in the PS beam, and powered throughout the test. The laserdiode was replaced by a 50 Ω resistor in order to monitor only the changes within the ASIC. Supply voltage and the control current I_{set} were adjustable. As digital sequence a simple 20 MHz clock was used. The currents $I_{forward}$ and I_{bleed}, and the current consumption were monitored.

[4]designed and prepared at OSU

A dramatical change in the duty cycle was observed at 14 MRad. Hardcopies of the inverted signals of one chip are depicted in Figure 8.7. The lowest waveform was taken before the irradiation, the middle at 14 MRad and the upper waveform at 20.55 MRad. Tests after the irradiation showed, that this behaviour was due to an error in the design of the voltage reference for LVDC receiver [81]. The dependence of $I_{forward}$ and I_{bleed} from

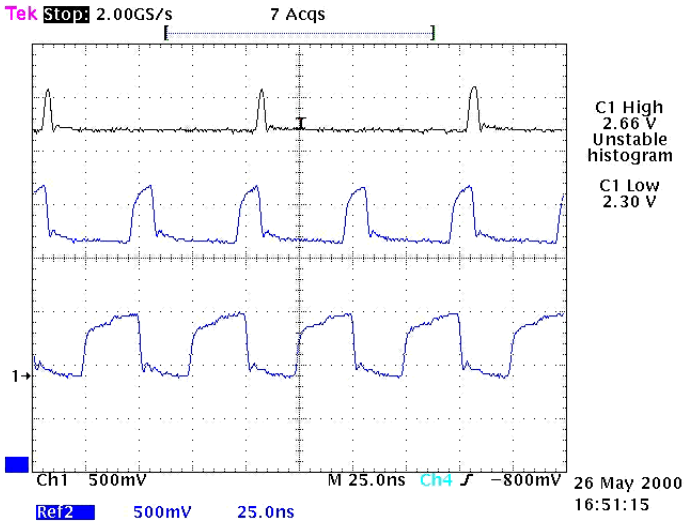

Figure 8.7: *Hardcopy of* VDC*transmitted signal shape taken before irradiation (lowest waveform), after 14 MRad (middle waveform), and 20.55 MRad.*

I_{set} was measured before and after the irradiation, and after an annealing period[5]. This is illustrated for one sample VDC in Figure 8.8. No significant change was observed for the amplitude of $I_{forward}$, whereas the bleed current I_{bleed} was still increased after the annealing period.

A second DMILL iteration of this chip with a different RESET configuration was irradiated at CERN. The overall resistance against the radiation was improved, most chips have sustained their good performance during irradiation. Due to a misalignment in the cold box system the total dose of the chips varied from chip to chip. The lowest dose for a VDC was 39.4 MRad and the highest 50.14 MRad. Figure 8.9 depicts the currents $I_{forward}$ and I_{bleed} versus the total dose measured at I_{set}=2.0 mA. No significant changes were detected up to 10 MRad, as guaranteed by the manufacturer. Above this dose both currents decreased. One chip (OSU2) suddenly stopped transmitting signals at 30 MRad, whereas the other two chips showed relative good performance up to 44.8 and 50.14 MRad. Back in the laboratory it was observed, that the VDC OSU2 has maintained its abilities, even so it stopped transmitting data during the irradiation. This can be explained by a failing commercial LVDS driver which was placed about 3 m beside the beam pipe. This commercial driver was a part of the test setup, enabling the sending of this signal type over the distance of 20 m.

[5]700 h powered at room temperature and 168 h at 100°C

VDC Wupp1, which has received 44.8 MRad, transmitted signals and showed good annealing behaviour. Only the start-up of this chip showed some deterioration. At initial turn-on a constant high level was detected at the output stage, even so a clock signal was send. This high level was adjustable with the control current. A higher supply voltage of 3.8 V was necessary to start the transmission. Afterwards this could be directly reduced to the default value of 3.2 V. This behaviour was reproducible and did not change after 100 h of annealing. The third chip with the highest total dose totally failed to work. All together one can say that the DMILL VDC sustained its abilities up to a total dose of 30 MRad,

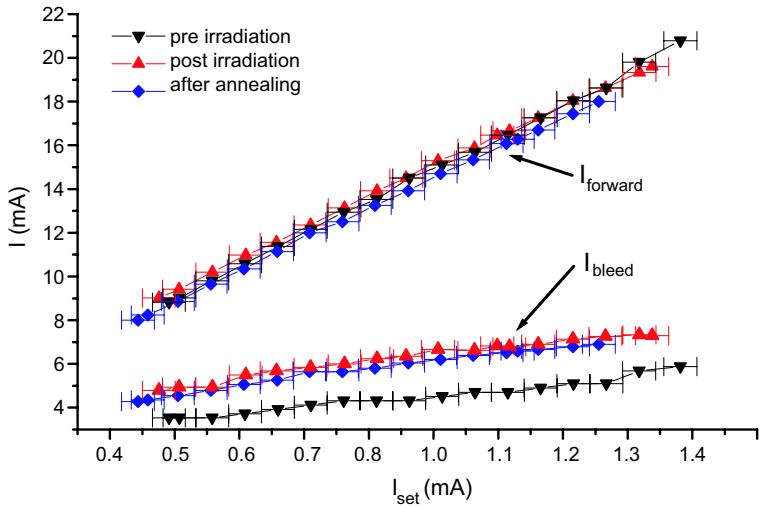

Figure 8.8: $I_{forward}$ *and* I_{bleed} *versus the control current* I_{set}*. The bleed current is after the annealing period still increased.*

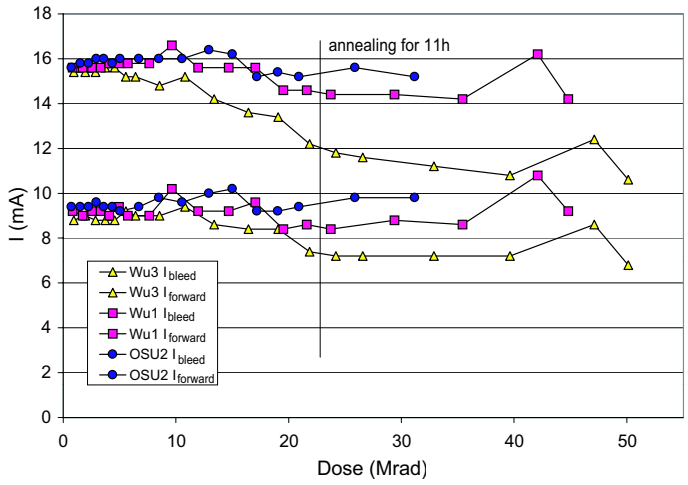

Figure 8.9: $I_{forward}$ *and* I_{bleed} *versus the total dose measured at* I_{set}*=2.0 mA*

which is above the expected dose for PP0. Above this radiation level, the performance is uncertain.

Five DORICs of the second DMILL submission were placed in the same cold-box at the PS beam and irradiated with 24 GeV protons. The chips received total doses between 34 MRad and 52.8 MRad, depending on the position within the box. All chips were supplied with BPM encoded random data, as electrical signals with a fixed mean current of 180 μA and 90 μA. This is high compared to the expected signal size of 75 μA. During the irradiation some functionality of the decoder could be sustained by increasing the supply voltage from the nominal 3.2 V to 5.0 V. Comparison of the threshold before and after irradiation showed an increase of the threshold of up to a factor 4.

8.1.4 Conclusions

The presented results revealed flaws in the current DMILL design of the driver electronics such as extreme sensitivity to noise in the DORIC preamplifier. This suggested a redesign of the circuits in a deep submicron technology. The redesign has already been made and a version has been tested in July 2001.

8.2 The Off-Detector Electronics

The Off-Detector electronics required for the optical link are positioned on the Back of Crate Card integrated in the Read Out Driver (ROD, section 3.3). This device is similar for SCT and Pixel Detector and the optical ASICs will be common for both.

8.2.1 The Bi-Phase Mark Encoder

The Bi-Phase Mark Encoder (BPM) encodes the control data and the timing to one signal, named BiPhase Mark. BPM encoding sends transitions corresponding to clock leading edges only with extra transitions at clock trailing edges to indicate data 1's. The Clock has to be regenerated from leading edge transitions and data from the extra transitions. For fine synchronisation of the clock for different distant modules, the BPM is able to delay the clock in steps of 500 ps. The BPM also translates the signal from LVDS to a current signal to drive the VCSEL. The light signals travel through a fibre to the modules on the detector side [87].

8.2.2 The Driver Receiver IC

The optical signals send from the module to the read-out are translated into LVDS signals by the Driver Receiver IC (DRX). This chip is, as the BPM, a 12 channel device. The expected signal range of the DRX ranges from 57 to 500 μA mean photo-current to allow for the decrease of the optical signals due to radiation damages within the laserdiode and the optical fibre. The Driver Receiver IC (DRX) receives the collected data via a PiN

photodiode and transfers this into LVDS format. The preamplifier is designed in analogy to the preamplifier of the Sct Doric [88].

Chapter 9

Single-Event Upsets

In this chapter the impact of minimum ionising particles, neutrons, and high energy particles directly on the performance of the optical link is described. After a general description of single–event effects (SEE) the experimental procedure is outlined. The results obtained for different particle types and energies with the main focus on fluxes expected in the ATLAS Inner Detector follow. The implications on the optical link of the ATLAS Pixel Detector derived from these studies are given at the end of the chapter.

9.1 General Description of Single–Event Effects

A *single–event effect* (SEE), as the term suggests, results from a single energetic particle. These effects can be classified into three categories, in order of permanency :

1. *Single–event upset* (SEU) is defined by NASA as "radiation–induced errors in microelectronic circuits caused when charged particles (usually from the radiation belts or from cosmic rays) lose energy by ionising the medium through which they pass, leaving behind a wake of electron–hole pairs" [89]. SEUs are soft errors and non-destructive. A reset or rewriting of a microelectronic device results in normal behaviour afterwards. A SEU may occur in analogue, digital or optical components, and also may effect the surrounding interface circuitry. SEUs typically appear as transient pulses, induced by primary and secondary ionisation, in logic or support circuitry, or as bit flips in memory cells or registers.

2. *Single–event latch-up* (SEL) is a condition that causes loss of device functionality due to a single-event induced current state. These are hard errors, and are potentially destructive. The SEL results in a high operating current, above device specifications. The latched condition can destroy the device, drag down the bus voltage or damage the power supply. In very sensitive devices, protons can cause SELs. It is cleared by a power cycle or power strobing of the device. If the power is not removed quickly, catastrophic failure may occur due to excessive heating, metallisation or bond failure.

3. *Single–event burnout* (SEB) is a condition that can cause device destruction due to a high current state in a power transition. SEB causes the device to fail permanently. SEBs include burnout in power MOSFETs, gate rupture, frozen bits and noise in CCDs.

If the Delay Locked Loop (DLL) within the DORIC4a chip mislockes, a possible hard error within the optical link used for the following tests may occur. This is not expected to have a serious effect since the DORIC4a is designed to minimise the possibility of such an error occurring. The ASICs used are also designed with protection resistors so that SEB is not expected to appear. They are designed using only bipolar transistors so effects as latch-up would not be expected to occur. Additionally the ASICs are designed to minimise SEU effects by operating at relatively high signal level.

9.2 Single–Event Upsets

Single–Event Upsets (SEU) have always been a serious concern for space electronics. Solar flare particle events pose the most extreme SEU producing environment, especially for interplanetary space crafts [90]. In the recent years with the forthcoming LHC, single-event effects have also become an important issue for the high–energy physics community.

The parts of the system that are most sensitive to SEU effects are the PiN diode and the amplifier of the receiver chip, as this is the only part of the system which is sensitive to relatively small signals. The active region of the PiN photodiode has a diameter of 350μm and a thickness of 15μm, which is very much larger than the active region of of a pn-node in microelectronic devices as the DORIC4a. In previous studies of optical links in space applications [93, 92] it was also established that the PiN photodiode is the most sensitive element to SEU.

Therefore the following studies concentrate on SEUs in the optical link due to transient pulse within the PiN photodiode. As shown in Figure 9.1, data can be disrupted if a particle-

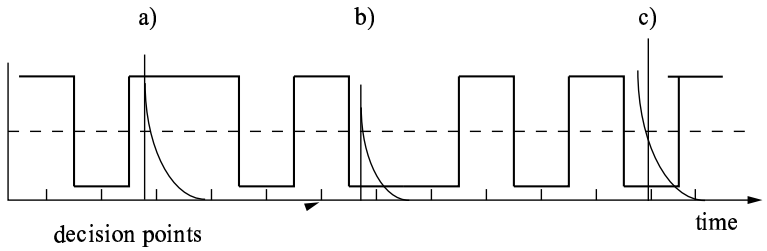

Figure 9.1: *Impact of single particle: resulting current pulses sensed in the receiver circuit which decay with an RC time constant determined by the circuit bandwidth [100]. a) "1" is not corrupted b) this "0" may be corrupted c) this "0" is corrupted.*

induced current exceeding the threshold current is sensed at the critical mid-bit decision, when a zero is transmitted.

In order to create a SEU, a minimum energy deposition in the few MeV range is necessary. This is much larger than the most probable energy deposition by MIPs of 58keV. Therefore MIPs are not expected to create SEU effects [94]. For the optical links in the ATLAS Inner Detector Bit errors in the TTC link can cause an SCT or Pixel module to fail to recognise a first level (LVL1) signal. This will cause subsequent triggers for this module to be out of synchronisation with the rest of the system. The Pixel MCC is designed to tolerate a bit-flip within the LVL1-signal by using a 5-bit long LVL1 command. Furthermore no configuration commands can be taken as a LVL1 trigger when a bit-flip occurs.

However, since exceptional performance is demanded, the optical link system has to be designed in a way to minimise the probability of failure.

9.3 Irradiation Facilities

9.3.1 Birmingham University Cyclotron

Tests with neutrons were performed at the Birmingham University Cyclotron. The neutrons were created by the reaction: $D + Ag \rightarrow n + Y$. The primary D beam energy was 18 MeV and the resulting neutron spectrum had a broad peak at 9 MeV.

9.3.2 National Physics Laboratory

Further tests with neutrons were performed at the National Physical Laboratory in London (NPL) [94]. Neutrons were created from 100 keV D ions by the reaction: $D + T \rightarrow n + \alpha$ A nearly mono–energetic beam of neutrons with an energy of 14 MeV was created with a flux of $5 \cdot 10^7$ cm^{-2}s^{-1}.

9.3.3 Paul Scherrer Institut

The particle spectrum in the ATLAS SCT and Pixel detector will be dominated by pions and protons (see Chapter 4.3). The πM1 beam line at the Paul Scherrer Institut (PSI) is a high resolution pion beam line with a momentum range between 100 and 500 MeV/c. A primary proton beam with a kinetic energy of 590 MeV from the Ring Cyclotron [101] is impinged on a target. The πM1 beam line is attached to the target station at an extraction angle of 22°, which corresponds to the orientation of the target wheel. Figure 9.2 depicts the beam components of the πM1 beam. Figure 9.3 gives the measured particle fluxes for the standard beam-line tune as a function of momentum with an uncertainty of 10% at the peak of the yield curves.

Mixed beams with protons and pions were used to test the optical link. Two dipole magnets (ASM11 and ASM12) were used to select the momenta in the range 300 to 465 MeV/c. Two final quadrupoles (QSL15 and QSL16) were used to focus the particle beam onto the

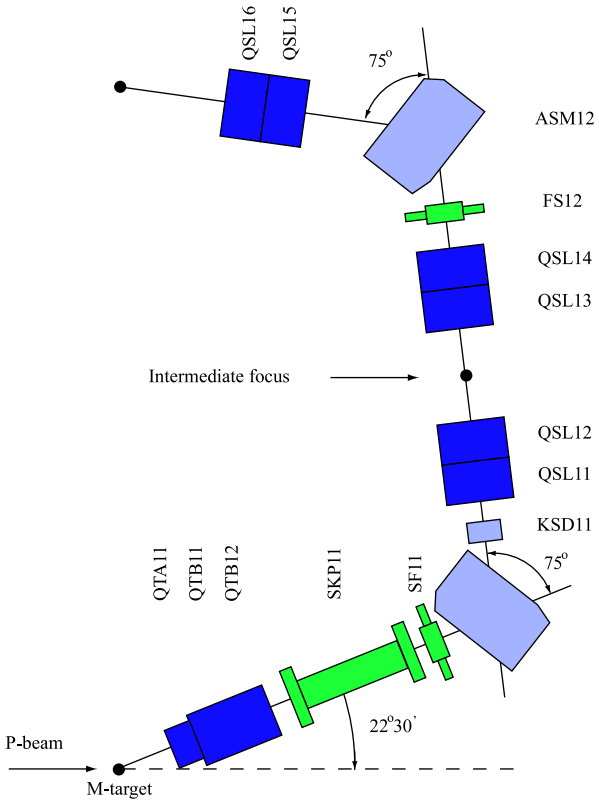

Figure 9.2: *The PSI πM1 beam line.*

optical package. The quadrupole system can be accessed by a computer system. No permanent beam monitor was available at the beam line. Therefore a system was set up using multi-wire proportional chambers (MWPCs) and scintillator counters. Two MWPCs with a wire spacing of 2 mm were used to measure the beam profile. The fluxes were measured with two scintillator counters (S1 and S2). The set-up for this experiment is illustrated in Figure 9.4. The counter S1 was a conventional large area scintillation counter with a light guide to couple the light to a photomultiplier. The counter S2 contained a 1 mm thick circular piece of scintillator with a diameter of 2 mm. This was directly coupled with optical grease to a small photomultiplier[1]. The amplified output of both photo-multipliers is fed into discriminators. The output of the discriminators were fed into scalars to measure the rates. A scan of the discriminator threshold was made and a plateau was found, were the counters were 100% efficient. The outputs were simultaneously viewed on an analogue oscilloscope to check for double pulsing. One MWPC measured the profile in the horizontal direction, the second was used to find the vertical direction. Upstream slits were used to limit the beam flux during the operation of the MWPCs. At low fluxes, the large scintillation counter S1 was used to trigger the MWPCs. Once the beam had been tuned and the profile measured, the high voltage for the MWPCs and counter S1 were switched off.

[1]Hamamatsu R5600

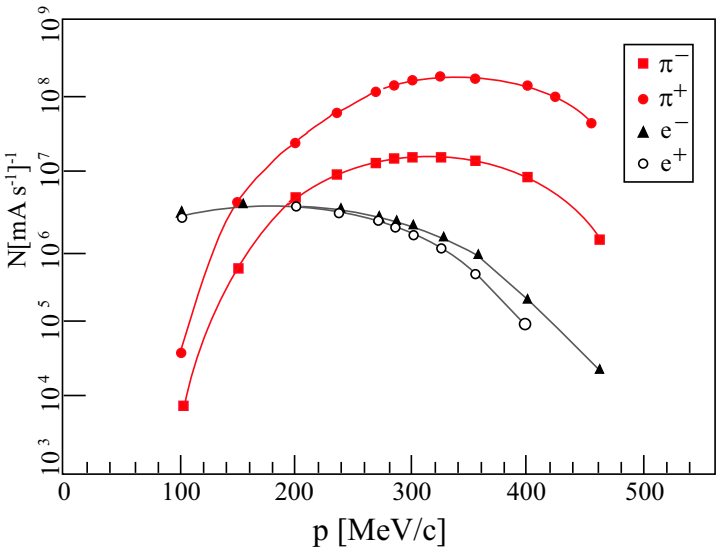

Figure 9.3: *Pion and electron fluxes in πM1 at the PSI.*

The slits were opened up to produce the maximum flux. The small scintillation counter S2 was moved by a computer controlled x-y stage. It was possible to measure the beam profile as a function of horizontal and vertical position. The beam profiles measured with S2 were found to be in good agreement with the profile measured with the MWPCs. The amplified signal from the S2 counter was viewed on an oscilloscope to verify that there are

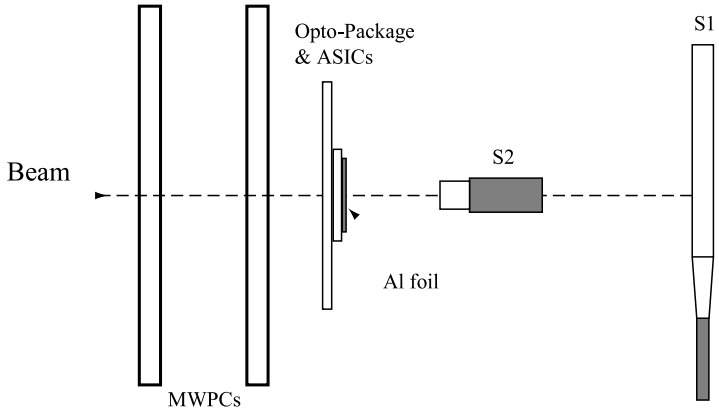

Figure 9.4: *Schematic view of the layout of the scintillation counters, wire chambers and the optical link in the target area of the PSI πM1 beam line*

no saturation effects at the highest fluxes used. From the pulses observed, it was possible to distinguish pions from protons. It has been found, that the beam was dominated by pions for all momenta, except for the highest momentum used (465 MeV/c) where protons were dominant.

Flux measurements

The rate measured with the small scintillation counter S2 determined the flux. To first order it could be simply evaluated by dividing the measured rate by the area of the counter. Two corrections were applied to the raw value of the flux. First a simple program was used to correct for the dead-time of the discriminator which had been set to 100 ns, allowing for the 20 ns bunch structure of the machine. Secondly the flux was noted and a correction was made for the average on-time of the machine which could be evaluated as the primary currents in the machine were continuously recorded.

Two cross checks of this procedure were performed. Firstly the slit has been set in narrow position to limit the flux and the rates in the two counters S1 and S2 were measured. The counter S1 was large enough to fully contain the beam. The predicted ratio of the rates S1 and S2 was calculated by fitting the measured beam profiles to a Gaussian distribution. The predicted ratio agreed with the measured ratio to within 10%. The second cross check of the flux measurements with the small counter S2 was performed using aluminium foil activation measurements. The reaction

$\pi +^{27}\mathrm{Al} \rightarrow^{24}\mathrm{Na} + X$

was used. Small aluminium foils were prepared and weighed. Next the foils were attached to the back of the optical link support. The foils were then exposed in the beam and afterwards removed. The resulting activation of the Al was measured using a Ge(li) counter. The spectrum was analysed and the number of events corresponding to the ^{24}Na was taken from [95]. A small correction was applied to allow for the width of the beam profile. The results of this analysis are summarised in Table 9.1. The agreement between

Flux determined from Al foil (10^6cm^{-2}s-1)	Flux determined from S2 (10^6cm^{-2}s-1)
4.25 ± 0.25 (stat) ± 0.34 (syst)	4.71

Table 9.1: *Comparison of flux measurements from aluminium foils and scintillation counter S2.*

the aluminium foil activation and the scintillation counter for the flux was within 10% and consistent with the expected errors. The difference found between these two cross checks revealed systematic errors on all flux measurements to be ± 10%. The statistical error on the flux measurements with the scintillation counter was negligible in comparison to the systematic error. The beam momenta, flux and dominant particle composition for the different runs are given in Table 9.2.

Momentum (MeV/c)	Flux ($10^6 cm^{-2} s-1$)	Dominant particle type
300	2.9	π
350	56	π
400	102	π
465	120	p

Table 9.2: *Data for the different beams used at PSI*

9.4 Testing Procedure and Results

9.4.1 Experimental Procedure

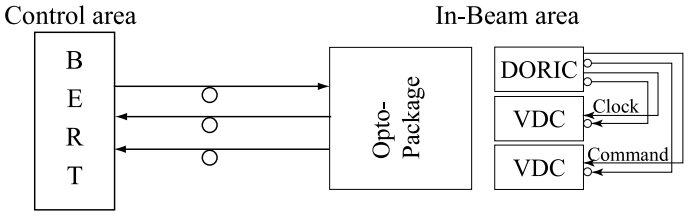

Figure 9.5: *General Test set-up for the different SEU studies.*

For all SEU studies an optical link consisting of a VDC, DORIC4a and a Marconi optical package, containing two VCSELs and one Centronic PiN photodiode[2], was used. The support of the link is realised by a kapton/copper structure, the so-called "dogleg" (Figure 9.6) and a support frame. In each case the link was arranged in a way, with the beam focused perpendicular onto the surface of the Opto–Package. BPM data are generated by the test system and optically send to the PiN diode. The data recovered by the DORIC4a is looped back into the LVDS input of the VDC and send optically back to the Bit Error Rate Tester (BERT). Within the BERT the returned data was compared with the original data and the errors counted. Figure 9.5 depicts a schematic of this set-up. A good indication for the overall performance of this link is the minimal light input required for the TTC link to operate with a negligible Bit Error Rate (BER). The comparison of measurements of this threshold under different environmental conditions gives an indication about the quality of the system.

Different scans of BER vs. optical power were always done, with and without beam. The Bit Error Rate Tester (BERT) was placed outside the beam area in a controlled area. The distance between the BERT and the optical link components (VDC, DORIC VCSEL, PiN) was about 20 m. For the last metre within the experiment radiation hard fibre was used. The set-up itself was not changed between the measurements with and without beam.

[2]same type as described in Chapter 5

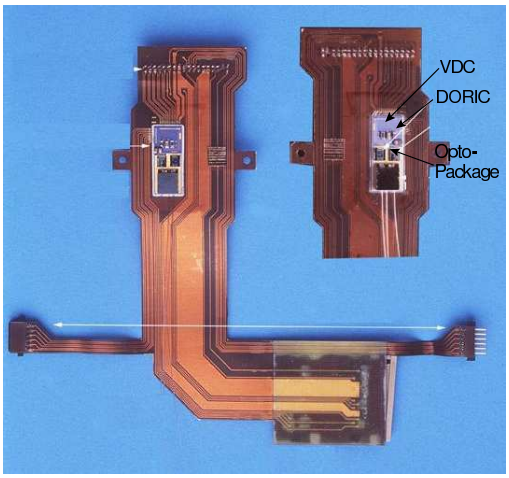

Figure 9.6: *Photograph of the opto-package and ASICs on the copper/kapton cable mounted on the support in the PSI beam line*

9.4.2 Single–Event Upsets with a Beta-Source

The first test of the ATLAS SCT opto-links for Single-Event-Upsets (SEU) was conducted with a 600 Mbq–^{90}Sr–source. This provided electrons with kinetic energies of up to 0.55 MeV to simulate the effect of Minimum Ionising Particles (MIPs). The given particle flux through the PIN diode and DORIC4 was about $4.3 \cdot 10^7$ cm^{-2}s^{-1}, which is comparable with the flux calculated for the B-Layer of the ATLAS Pixel Detector (see chapter 4.3). Sending light pulses with an optical power of 500 μW in the TTC link, zero errors were detected in 12 hours. The resulting 90% confidence level upper limit of the BER was $1.3 \cdot 10^{-12}$. This confirms the expectation that MIPs will not cause a significant SEU rate.

9.4.3 Single–Event Upsets with Neutrons

The result of this test is shown in Figure 9.7. The fluence was measured with aluminium foils and the estimated flux of neutrons was $1.1{\cdot}10^6$n cm^{-2}/s. This is about the expected flux in the ATLAS SCT. No significant difference in the BER with beam on and off was observed from longer runs. At an optical power input of 538 μW, the SEU rate was less than $4.1 \cdot 10^{-11}$ at the 90% confidence level. The measurements performed at NPL with higher energy and higher flux neutrons are illustrated in Figure 9.8. Comparing the BER scans with beam off and beam on, there is clear evidence for significant SEU effects. The value of the PiN currents I_{PiN} were not monitored during these measurements. Therfore these measurements can only be used to give a qualitative indication that SEU effects can occur as the systematic uncertainty is too large to use these measurements for any quantitative analysis. However, these results confirm the hypothesis that low energy neutrons do not produce significant SEU rates.

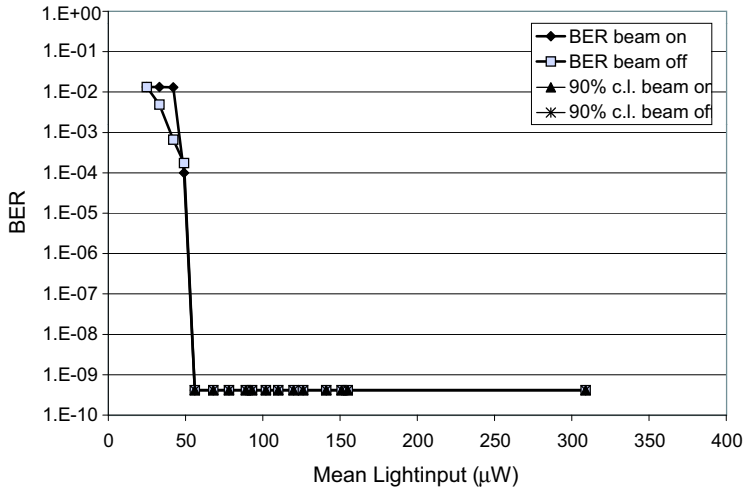

Figure 9.7: *Bit error rate versus the PiN current for different beam conditions at the Birmingham University Cyclotron.*

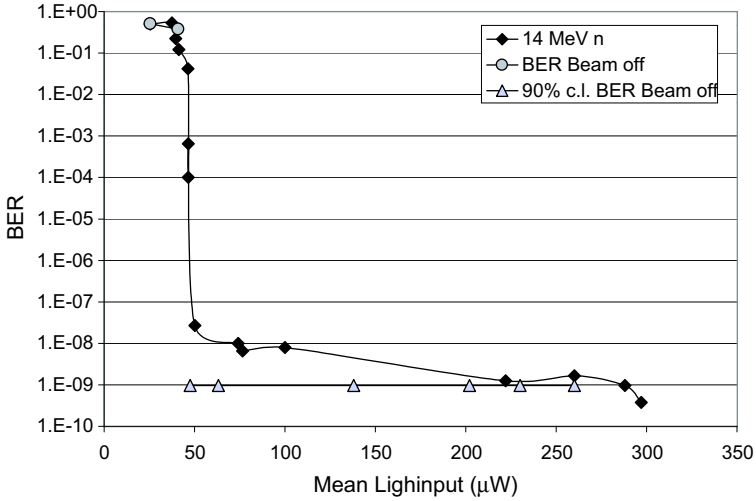

Figure 9.8: *Bit error rate versus the light-input for different beam conditions [94].*

9.4.4 Single–Event Upsets with Pions and Protons

Figure 9.9 depicts different BER scans versus the PiN current I_{PiN} for the beam on and the beam off. During the beam off scan, no errors occurred for values of I_{PiN} greater than 30 μA, whilst there was a measurable BER for this range of I_{PiN} with beam on. This allows the conclusion, that the errors are due to SEU effects. No mis-lock of the DLL in DORIC4a occurred at any time. The BER induced by SEU decreases rapidly with

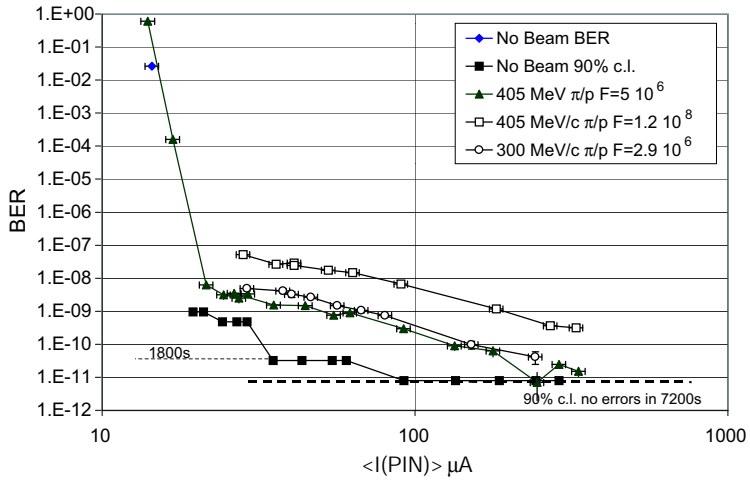

Figure 9.9: *BER scan versus the I_{PIN} for beam off and different beam momenta and fluxes. The square symbols correspond to no errors and are 90% confidence level upper limits.*

increasing I_{PiN}. This confirms the hypothesis that the dominant source of SEU effects is the energy deposition within the PiN photodiode or within the transistors of the amplifier in the DORIC4a. A previous SEU study for the CMS optical link [96] showed, that the dominant SEU effect is occurring in the PiN photodiode instead in the amplifier.

For the further analysis the assumption that the SEU are only occurring in the PiN diode is used. To compare the data for the different beam momenta and fluxes F it is convenient to define the SEU cross section by

$$\sigma_{SEU} = \frac{N_{errors}}{F \times t} \tag{9.1}$$

with N_{errors} the number of errors occurring during the time t. In Figure 9.10 the plot σ_{SEU} versus I_{PiN} is shown. Simulations of SEU [97] predict, that the SEU rate should be proportional to flux. The data of two scans taken at the beam momenta of 405 MeV/c with two different fluxes resulted in the same cross section, which is consistent with the hypthesis. The data for different particle type and momenta all look very similar, except the data of the 300 MeV/c pion beam. One possible explanation for the significant higher σ_{SEU} at the same values of I_{PiN} is the Δ resonance in pion-nucleon scattering which gives rise to an increase in the total pion-proton interaction cross-section [9]. Detailed simulations similar to [97] would be needed to verify this. It is convenient to convert the value I_{PiN} to an equivalent energy deposition in the PiN photodiode E_{MIN}. This is useful to compare this data with any future calculation that may be performed along the lines of [97]. For this conversion the DORIC4 input amplifier is assumed as being equivalent to an RC shaper. The E_{MIN} looks like

$$E_{MIN} = (I_{PIN} + I_h)\frac{E_{eh}}{e\omega_0} \tag{9.2}$$

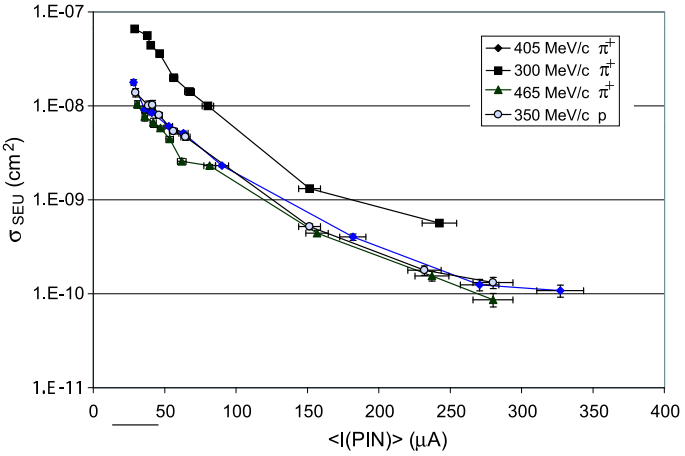

Figure 9.10: *SEU cross section versus the PiN I_{PiN} for different beam momenta.*

with

E_{MIN}	minimum energy deposit required to trigger DORIC,
I_{PiN}	average photocurrent,
I_h	constant representing the hystersis in DORIC,
E_{eh}	mean energy deposition to create an electron–hole pair in Silicon,
e	elementary charge,
ω_0	$\frac{1}{RC}$ time constant of the DORIC input stage.

Quantity	Value	Units
I_h	10.0	μA
E_{eh}	3.6	eV
ω_0	1.0	$(\text{ns})^{-1}$

Table 9.3: *Parameter values in the model of the input amplifier for the* DORIC*4a.*

Table 9.3 summarises the parameter values used for the analysis.

The converted data are shown in Figure 9.11. The data presented here is inconsistent with the hypothesis, that the SEU cross section is constant for energies above 20 MeV, which is the standard procedure for estimating SEU effects in ATLAS. By performing a convolution

$$BER = \frac{1}{D} \int \sigma_{SEU} \frac{dF}{dp} dp \tag{9.3}$$

where F is the flux as a function of momentum p and D the data rate (40 Mbit/s), this data could be used to predict the SEU induced BER of the SCT TTC links during ATLAS operation. This would need a detailed simulation similar to that of the type performed in [97].

A conservative upper limit can be evaluated by using the 300 MeV/c data with the highest values of σ_{SEU}. For an expected value of I_{PiN} a minimum energy deposition $E_{MIN} = 1.91$ MeV is calculated. Reading σ_{SEU} of the data in Figure 9.11, a value of $\sigma_{SEU} = 1.2 \cdot 10^{-8}$ is estimated.

$$BER = \frac{\sigma F}{D} \tag{9.4}$$

and the maximum flux expected for the SCT ($F = 1.2 \cdot 10^6\ 1/cm^2$) gives an upper limit of $BER = 3.6 \cdot 10^{-10}$, which is below the ATLAS SCT specification of 10^{-9}.

9.5 Implications for the ATLAS Pixel Detector

The previous SEU studies were performed with optical links of the SCT collaboration. Since a SEU corresponds to a given size signal in the PiN photodiode being larger than the corresponding optical signal from the fibre, the SEU calculation is almost independent of the DORIC version [99]. Therefore it is possible to use the studies performed at the SCT link to estimate a worst case SEU rate for the Pixel system. The major impact on the error rate is given by the much higher flux within the Pixel Detector. The minimum energy E_{MIN} is calculated for the DORICp-D2 with the data collected at PSI (Figure 9.10) and the values given in Table 9.4. This gives the possibility to derive the BER expected with

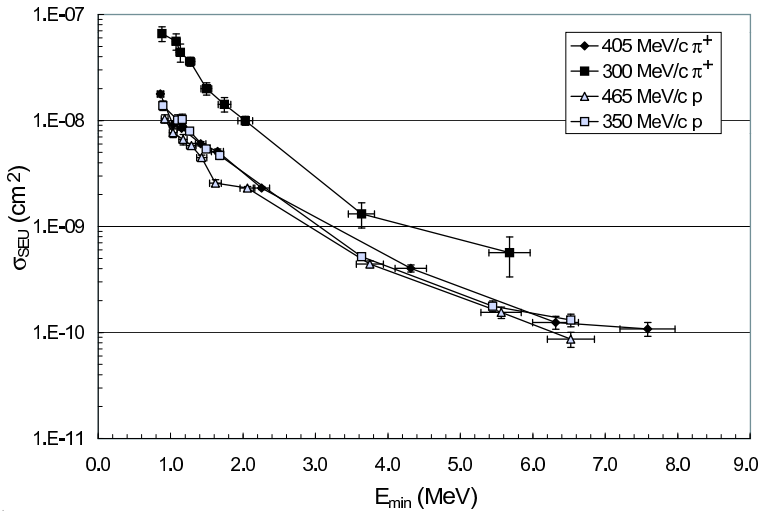

Figure 9.11: *SEU cross section versus minimum energy deposition in the PiN photodiode for different beam momenta.*

Quantity	Value	Units
I_h	0.0	μA
E_{eh}	3.6	eV
ω_0	2.5	$(ns)^{-1}$

Table 9.4: *Parameter values in the model of the input amplifier for the* DORIC*p-D2.*

a photo-current of $I_{PiN} = 75$ μA for all three barrel layers and the patch panel PP0, and to calculate the necessary photo-current in order to get a BER less than 10^{-9}.

The results listed in Table 9.5 show that it is difficult to establish an optical link in the inner region of the Pixel barrel detector. In order to reach a BER better than 10^{-9} for the B-layer an average photo current of ≥ 200 μA is necessary, whereas a reasonable photo current of 65μA should be sufficient to reduce the BER below 10^{-9}. Taking into account the responsivity of the PiN photodiode (0.3 A/W post-irradiation), a loss of $\sim$ 3dB from ROD to detector-side and an additional $\sim$ 2dB due to the transition from GRIN fibres to SIMM fibres at patch panel PP2 a light pulse of 4.2 mW would be necessary. This is a value rarely reached by a common 840 nm VCSEL in an array. Using a brighter optical signal appears to be viable for the outer layers. For a 65 μA photocurrent, a light pulse of 1.4 mW would be necessary.

As mentioned above, the Pixel MCC is designed to tolerate a bit-flip within the LVL1-signal by using a 5-bit long LVL1 command. Therefore as long as there are not two flips in a Trigger command it will be transmitted without problems. The probability of a corrupt

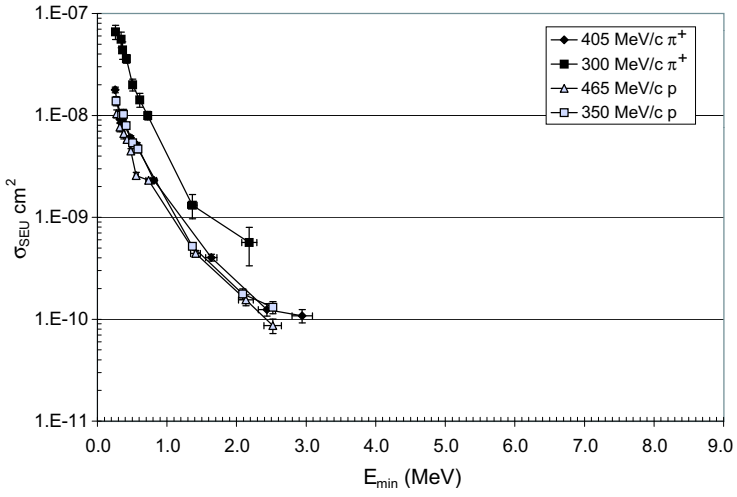

Figure 9.12: *SEU cross section versus minimum energy deposition in the PiN photodiode for different beam momenta. E_{MIN} is calculated for the different input stage of the* DORIC*p-D2.*

	BER @ I_{PiN}=75μA	I_{PiN} for BER $l10^{-9}$
B-Layer	$1.1 \cdot 10^{-8}$	>200μA
1st–Layer	$1.7 \cdot 10^{-9}$	≈100μA
2nd–Layer	$8.8 \cdot 10^{-10}$	75μA
PP0	$6.4 \cdot 10^{-10}$	65μA

Table 9.5: *Estimated BERs for I_{Pin} =75μA and the estimated light power needed for BER< 10^{-9} for all three Pixel layer and the patch panel PP0.*

LVL1 is of the order of 10^{-17}. This is not the case for Fast and Slow commands. Additional programming ensures, that in the case of a single bit flip a Fast Command can never be interpreted as a LVL1 or Slow command. This ensures that no Trigger commands are added or lost, even while issuing Fast Commands with one bit flip[3]. Regarding the Slow (configuration) Commands the MCC is programmed that in case of a single bit flip no Trigger commands are produced in the 13 bit long Slow Command Header transmitted from the MCC to the FE-chips. For the Data part such a programming is not possible since this can be more than 3.000 bits long. By reading it back, one can make sure it has been transmitted correctly. However, for an elaborated testing of the impact of the high particle rate on the optical link performance, the assessment of the effect of SEU on the module setting by a simulation is suggested.

9.6 Conclusions

When finalising the layout of the optical link of the ATLAS Pixel Detector the effects of the SEU have to be taken into account. The analysis of data taken at PSI imply, that a position of the link into a detector area with a lower flux is preferable. At the position of the patch panel PP0 a mean photo-current of 65 μA should be sufficient for a BER of less than 10^{-9}. Furthermore the use of a brighter 840 nm laser on the ROD side is recommended. Instead of VCSEL arrays, which can only be driven up to 18 mA, single packaged VCSELs could be chosen. These can be driven up to 25 mA due to the better cooling in a single package. This would have the additional advantage that in case of a necessary replacement, only one VCSEL would have to be exchanged. In [90, 100] it is recommended to use a III-IV direct bandgap detector since the depletion depth need only about 2-3 microns for > 80% quantum efficiency, in contrast to the indirect bandgap silicon detectors chosen for the presented study. But due to the very good radiation hardness of these devices, which cannot be achieved by GaAs photodetectors, and the possibility to minimise SEU by using a brighter signal, these silicon devices should be used for the ATLAS Pixel detector optical link.

[3]Fast Commands can be issued while DataTaking is active

Chapter 10

Implications for the Atlas Pixel Detector Optical Link System

The results of the studies presented in the previous chapters reflect the difficulty of designing a radiation tolerant optical link for the Atlas Pixel Detector. In this chapter the reasons for the chosen position are given and a final design for the optical link is presented.

10.1 Optical Link Location and Cooling

The original plan of placing the optical link directly onto the Pixel modules can not be realised due to severe space constraints, mainly in the barrel section. The optical package with a minimum height of 1.5 mm can not be fitted into the envelope of the layers. Furthermore a routing of the fibres into the barrel section without violating the minimal

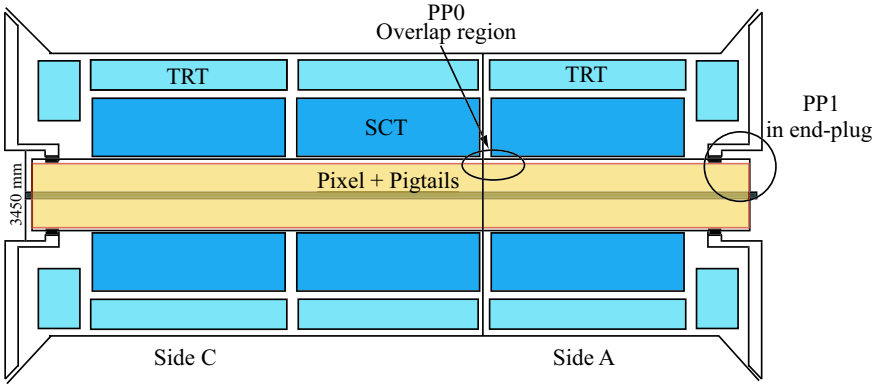

Figure 10.1: *Cross section of the Atlas Inner Detector showing the subdetectors and patch panel positions PP0 and PP1. Pigtails will ensure the transmission of the electrical signals from each module to its belonging optical link.*

bending radius of the optical fibres (Chapter 5.3) is not feasible. An adaptable position for the optical link is the patch panel PP0 at the ends of the pixel barrel near the outer radius ($\sim$ 18 cm), marked in the cross section of the ATLAS Inner Detector in Figure 10.1. The electrical signals will be transmitted over narrow kapton cabels, the so-called pigtails.

An advantages of the PP0 position is the much lower flux and the resulting fluence. The radiation damage (Chapter 8 and 6) and single event effects (Chapter 9) within the devices can be kept at a relative low level. However, there are also disadvantages, such as the risk of cross talk due to the transmission of electrical signals over a distance of up to 1.2 m. First measurements with prototype pigtails showed promising results.

In the case of an optical link directly on the module cooling was guaranteed by the cooling system placed within the stave. The radiation hardness and accelerated lifetime studies of VCSELs and PiN photodiodes have proven, that cooling is essential for these devices. To avoid loosing more than 1 % of the laserdiodes or PiN photodiodes, the cooling has to be designed in such a way, that the opto-electronic devices will have a temperature below 20°C. Best performance is expected at a temperature of (0 ± 5)°C. The cooling system is integrated in the PP0 support. A critical issue is the thermal connection between the boards and the cooling pipes.

10.2 Opto-board containing seven Optical Links

The space allocated for the optical link within the patch panel is also constrained. An integration of the optical links for one half stave (six, respectively seven modules) or six disks on one electrical board, including the VCSELs and PiN photodiodes packaged in "8x1" Taiwan packages (Chapter 7) saves space and simplifies the handling. This so-called opto-board will be plugged into the patch panel support via a standard 80-pin connector, routing all signal and power traces to the module and the outer world. The width of the board is limited to 20 mm. Figure 10.2 illustrates the top and bottom side of such an opto-board.

The implementation of the VCSEL driver chips VDC and the decoding chip DORIC in a deep submicron technology will relax the space constrains due to the smaller physical size of chips processed in such a technology. The usage of 4 channel arrays of the chips is recommended to ease handling during production. Only seven of these eight channels per optical package will be routed to the module. The wire bond connection of the driver electronics and opto-electronics gives the freedom to connect a chip to the adjacent VCSEL in the case of a damaged VCSEL or vice versa. A fibre fan-out can be integrated in the optical package which enables the use of ribbon fibre and serves as strain relief at the same time.

Since the optical package does not exceed 1 cm, the two VCSEL packages can be positioned on one side, for example the top side, to supply the board with 16 VCSELs. On the opposite side the PiN package is positioned in the centre, leaving sufficient space for the larger DORICs and the passive components required for the RC filter on the input stage. This separation of the TTC and data link results in an easier fibre routing and less cross-talk.

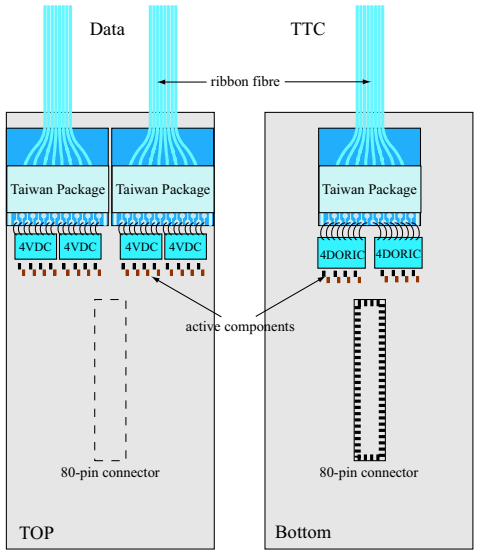

Figure 10.2: *Opto-board for patch panel PP0 containing opto-electronic devices and drivers to serve a B-Layer half-stave.*

Such an opto-board is common for all detector areas, including the B-Layer, which requires two VCSELs and VDCs per module due to the required higher data rate of 160 Mbit/s. In the case of the outer layers and the disks the same board can be used, but less optical packages and VDCs will be mounted. This unified board for the whole Pixel Detector simplifies the production of about 400 boards.

10.3 Production Issues

Coming closer to the commissioning of the LHC in 2006, all ATLAS detector subsystems have to start production. The separation of the optical link from the Pixel modules enables a completely independent production line. The opto-board production is in parallel to the module production. In Figure 10.3 the production steps of the optical board are illustrated. Each active component necessary for one opto-board has to be tested before the mounting process. In the following an overview of these tests is given.

The test of the VCSEL and PiN photodiode optical packages (test 1) includes the LIV curves from 0 to 25 mA drive current for the VCSELs and the measurement of the responsivity of the PiN diode at 5 V bias and 840 nm incident light. Irradiation tests of a small number per batch are generally required. Since the batches of the PiN diodes and VCSELs are already reserved and radiation hardness studies have been performed, this subject is already covered.

The second test is concerning the ASICs VDC and DORIC. Wafer tests should be forseen for this test. Tests after dicing might be unfeasible due to the smallness of these chips. The wafer tests of the DORIC should include basic functionality checks as a power check, LVDS level check, and a test if the clock and data recovery are correct. The VDC wafer test

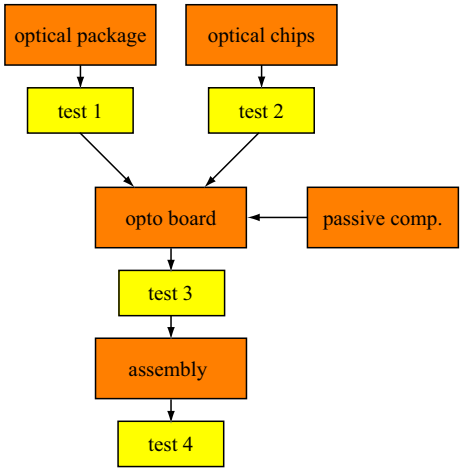

Figure 10.3: *Production sequence for the optical link indicating required tests at different points during production to ensure a high yield.*

should include a measurement of the switch current $I_{forward}$ and the bleed current I_{bleed} as a function of the control current I_{set}.

All passive and tested active components are mounted onto the opto board. Test 3 is a test of the complete opto-board and includes quality assurance and series testing. The quality assurance test will be done with about 5 % of the required boards. To ensure a constant quality during the production the boards will be inspected optically, the ESD sensitivity will be monitored, and power and temperature cycles will be applied. The series testing, performed with all boards, should include a BER scan for the TTC link and a measurement of the optical power as a function of the control current I_{set} for the data link. A commercial 16 channel bit error rate tester (BERT)[1] could be appropriate for this third test. The 16 channels of this tester enable an automated test of the opto boards within a short time. All boards for the production can be tested within a few month. The test results could directly be uploaded to the production data base. An interface board containing the Driver Receiver IC (DRX) and the BiPhase Mark Encoder (BPM) (Chapter 8) and 12 way VCSEL and PiN arrays is required to perform the complete link test. This ensures testing conditions similar to the experiment.

After the assembly of the patch panel at CERN a further test of the opto-board is required (test 4). For this purpose a simple functionality test is sufficient. The general performance of TTC and data links can be tested with BER scans at defined settings for one minute. Since the off-detector side is not easily accessible, the link has to be tested by sending configuration commands to the module controller chip and reading them directly back.

In conclusion a board containing seven optical links common for all areas is feasible and relaxes the production.

[1] Anritsu MP1630

Chapter 11

Summary

Optical links will be used for the subdetectors of the LHC ATLAS Detector SCT and Pixel Detector. In the framework of this thesis all essential parts for a radiation tolerant Pixel Detector optical link were studied, radiation tests were performed, and a design was proposed.

The expected fluxes and fluences of charged and neutral particles have been calculated for different positions in the ATLAS Inner Detector. The highest flux within the barrel is $2.75 \cdot 10^7$ $1/\mathrm{cm}^2\mathrm{sec}$ at the B-Layer radius. The highest total fluences within the barrel layers are $1.1 \cdot 10^{15} \mathrm{n}_{eq}/\mathrm{cm}^2$ for the Silicon and $7.8 \cdot 10^{15} \mathrm{n}_{eq}/\mathrm{cm}^2$ for GaAs for 10 LHC years. This extremely harsh environment makes radiation damage studies to the core of device evaluation.

Proton implanted VCSELs were irradiated at different radiation facilities. The VCSELs will degrade during LHC runtime due to normal operation and irradiation induced damages. The radiation tolerance studies of similar proton implanted VCSELs showed that the optical output of devices will decrease while the laser threshold will increase with rising fluence. VCSELs which were irradiated with intermediate annealing periods showed good recovery behaviour if an annealing current of at least 10 mA was applied. In case of a higher current the annealing is faster and a higher light output can be achieved. However, a maximum of 20 mA should not be exceeded to avoid damaging the laserdiode. During LHC operation intermediate annealing sessions, for example during shut-downs, would help to keep the radiation induced damages at a tolerable level. The highest accumulated fluence was about a factor 3 higher than the expected fluence at the radius forseen for the positioning of the on-detector optical link components. Light versus current-curves measured during this irradiation showed that, after a fluence comparable to the expected PP0 fluence, the VCSELs were operating with an increased laser threshold exhibiting a significant light output. This indicates that the VCSELs can survive this radiation level. A comparison of the behaviour of VCSELs irradiated up to the same fluence with protons of different energies (expressed in 1 MeV equivalent neutrons) proves that the NIEL scaling is also applicable to VCSELs. Accelerated lifetime tests of Mitel VCSELs predict a loss of VCSELs between 0.1% and 35%, strongly depending on the ambient temperature in the experiment cavity assumed to be -5 to +40°C. In order to get a tolerable failure rate, a temperature of (0 ± 5)°C is desirable.

The environmental conditions and space constrains make a custom made package with

fibres directly attached to the optoelectronic devices necessary. The difficulties of integrating optoelectronic devices in radiation tolerant non-magnetic packages with direct fibre coupling are described. The qualification of three candidate packages showed that different designs are feasible. The better results of the active alignment led to the choice of the so-called Taiwan package. The results collected within the framework of this thesis contributed to the selection of this baseline optical package.

Tests of the driver electronics for the pixel optical link revealed flaws in the current designs and suggested a redesign of the circuits in a deep submicron technology.

An extensive study of single event upsets (SEU) occurring within the analog part of the receiver indicated that the effects of the SEU have to be taken into account. The analysis of data taken at the Paul Scherrer Institut indicate that a position of the link into a detector area with a lower flux is highly desirable. At the position of the PP0 a mean photo-current of 65 μA should be sufficient for a bit error rate of less than 10^{-9}. Furthermore the use of a brighter 840 nm laser on the ROD side is recommended to get more safety during operation.

As a result an integration of seven optical links on one board, including optical package, 4-way deep submicron driver chips, and ribbon fibre as a solution for the Atlas Pixel Detector is proposed. A common solution for all barrel layers and disk sector is feasible and would relax production. This board will be positioned at the patch panel PP0 at the end of the Pixel barrel close to the outer radius. This results in a more relaxed routing and the minimal bending radius of the optical fibres allows not to be violated.

For the completion of the optical link design the development of the driver chips has to be finished including radiation damage studies. As indicated in this thesis simulation studies of SEU on the module setting procedure should be performed. As a byproduct of the studies the cross-talk on the electrical connection between module and optical link revealed no significance, but systematic studies of this field seem to be necessary.

In future hadron collider experiments the data links might have to transmit much higher data rates while being more radiation tolerant than necessary for the Lhc experiment. Since optical links are the best solution for such systems, this will increase the demands on radiation tolerant optical links. New developments could open a window for this sector. A viable solution within the next few years is a hybrid approach where silicon microelectronics is coupled with III-V optoelectronics. This would minimise the space consumption and handling while maximising the bandwidth.

Furthermore the use of Silicon instead of Gallium Arsenide as main emitter material will improve the radiation hardness of the systems. Even though Silicon is a poor emitter, first studies showed improvement in the light emitting of Silicon. Recently light emission has been demonstrated to be possible in Si when it is turned into a low dimensional system or when selected impurities were inserted in the lattice. Porous silicon showed room temperature luminescence with high quantum efficiencies.

Another compelling innovation would be the use of free space optoelectronics in Pixel systems, by incorporating a waveguide plane in a MCM-D structure. A BCB layer could serve as plane for the bus system between the read-out chips.

Bibliography

[1] D. Boussard et al., *The Large Hadron Collider conceptual design*, CERN/AC/95–05 (1995)

[2] The Atlas collaboration, *The Inner Detector Design Report*, ATLAS TDR 4, CERN/LHCC/97-16, and CERN/LHCC/97-17, April 1997

[3] Cern *The ATLAS Technical Proposal for a General Purpose pp Experiment at the Large Hadron Collider at* Cern, LHCC, 94–43, December 1994

[4] The Atlas collaboration, Atlas *Pixel Detector*, Technical Design Report, CERN/LHCC/98–13 ATLAS TDR 11, May 1998

[5] The Atlas collaboration, Atlas *Detector and Physics Performance*, Technical Design Report, CERN/LHCC/99–14 (vol.I) and CERN/LHCC/99–15 (vol.II), May 1999

[6] F. Gianotti, *Collider Physics:* Lhc, Lectures given at the European School of High–Energy Physics, Atlas Note ATL-CONF–2000–001, 2000

[7] The Delphi Collaboration, *Search for the Standard Model Higgs boson at* Lep *in the year 2000*, CERN-EP/2001-004, 10 January 2000

[8] D.E. Groom, *Particle Data Book*, The European Physical Journal C15 (2000)1

[9] D. Griffith, *Introduction to Elementary Particles*, John Wiley and Sons, New York 1987

[10] P.W. Higgs Phys. Rev. Lett. 12 (1964) 132 and Phys. Rev. 145 (1966)

[11] J.F. Gunion et al., *The Higgs Hunter's Guide*, Frontiers in Physics, Addison Wesley Publishing Company, 1990

[12] M. Siebel *Das Standardmodell–Higgs bei* Lep*?*, Seminar zur experimentellen Teilchenphysik, Talk January 2001

[13] ATLAS-Japan Collaboration, *Physics Potential*, 28 March 1998

[14] The Aleph collaboration *Observation of an Excess in the Search for the Standard Model Higgs Boson at* Aleph , CERN-EP/2000-138, November 13, 2000

[15] The LEP Higgs Working Group, *Standard Model Higgs Boson at* LEP*: Results with the 2000 Data, Request for Running in 2001*, Submitted to the CERN Research Board and to the CERN Directorate, 03-Nov-2000

[16] LEP Electroweak Working Group, `http://lepewwg.web.cern.ch/LEPEWWG/`

[17] D. Zeppenfeld, *Collider Physics*, MADPH–99–1100, Februar 1999

[18] K. Münich et al., *Determination of* A_{FB}^b *using inclusive charge reconstruction and lifetime tagging at* LEP*1*, DELPHI 2001-027 MORIO CONF 468, Moriond March 2001

[19] G. Altarelli, G. Isidori, *Lower limit on the Higgs mass in the Standard Model: an update*, Phys. Lett. B337 (1994) 141;

[20] J. Ellis *The 115 GeV Higgs Odyssey*, Invited contribution to the CMS Bulletin of December 2000, CERN–TH/2000–307, Nov. 2000

[21] B. Osculati, *Higgs search at* ATLAS*:* $H \rightarrow b\bar{b}$, XIth Recontres de Blois, Blois, France, 1999

[22] D. Ferrere *Silicon Vertex Detectors in HEP and in Semiconductor Tracker of* ATLAS, ATL-CONF-99-007, Belarus 1999

[23] S. Tapprogge, *Physics at* LHC*:* ATLAS *performance*, Atlas note ATL-CONF–99–004, October 1999

[24] W. Witzeling, *The* ATLAS *Detector – a Status Report*, Atlas note ATL-CONF–99–006, June 2000

[25] S. Gadomski, *ATLAS Inner Detector Performance*, ATL-CONF-2000-009, presented at BEAUTY 2000, Israel September 2000

[26] R. Wunstorf *Radiation tolerant sensors for the* ATLAS *Pixel Detector* Nucl. Instr. and Meth. in Phys. Res. A 466 (2001) 308-326, presented at the Hiroshima conference, 2000

[27] Oliver Bäsken, *Messungen an* ATLAS*-Pixeldetektor-Modulen in MCM-D Technologie*, WU-D 00-06 April 2000

[28] Christian Grah, *Testmessungen Auslesechips für den* ATLAS*-Pixeldetektor*, WU-D 00-02 Februar 2000

[29] O. Bäsken, K.-H. Becks, O. Ehrmann, P. Gerlach, Ch. Grah, I.M. Gregor, Ch. Linder, S. Meuser, J. Richardson, M. Toepper, J. Wolf, *First MCM-D Modules for the B-Physics Layer of the* ATLAS *Pixel Detector*, IEEE Trans. Nucl. Sci. 47 (2000) 745

[30] K.-H. Becks, O. Ehrmann, P. Gerlach, Ch. Grah, I.M. Gregor, M. Toepper, J. Wolf, *A MCM–D type module for the* ATLAS *Pixel Detector*, Proc. of IEEE Nuclear Science Symposium, Toronto, Canada Nov. 1998

[31] R. Wunstorf et al., *Radiation of Silicon Detectors by Monoenergetic Neutrons between 1 and 14 MeV and 1.8 MeV Electrons*, Nuclear Physics B (Proc. Suppl.) 23A. 1991

[32] S.I. Meuser, *Pixel Readout Chip for the* ATLAS *Experiment*, Proc. of IEEE Nuclear Science Symposium, Toronto, Canada Nov. 1998

[33] R. Becherle, *The Module Controller Chip (MCC) of the* ATLAS *Pixel Detector*, Proc. of IEEE Nuclear Science Symposium, Toronto, Canada Nov. 1998

[34] P. Sicho, L. Blanquart, P. Breugnon, *Analysis of Input and Output Characteristics of NMOS and PMOS Bipolar Transistors after Irradiation*, `http://www-hep.fzu.cz/pixpage/IRR/Reports/pmbar.pdf`, Pixel Electronics Meeting, September 2000

[35] Fabian Hügging, *Der ATLAS Pixelsensor – Der state-of-the-art Pixelsensor für teilchenphysikalische Anwendungen mit extrem hohen Strahlungsfeldern*, Dissertation am Fachbereich Physik der Universität Dortmund, Juni 2001

[36] Michael Moll, *Radiation Damage in Silicon Particle Detectors*, Dissertation, Hamburg 1999

[37] R. Wunstorf, *Systematische Untersuchungen zur Strahlenresistenz von Silizium-Detektoren für die Verwendung in Hochenergiephysik-Experimenten*, DESY FH1K-92-01, Dissertation (1992)

[38] A. Vasilescu *The NIEL scaling hypothesis applied to neutron spectra of irradiation facilities and in the* ATLAS *and CMS*, ROSE/TN/97-2, December 1999

[39] ASTM E772-93 *Standard practise for characterizing neutron fluence spectra in terms of an equivalent monoenergetic neutron fluence for radiation hardness testing of electronics*, revised version 1993

[40] A. Chilingarov et al, *Radiation Damage due to NIEL in GaAs Particle Detectors*, INDET-NO-134, June 1996

[41] A. Vasilescu *Notes on the fluence normalisation based on the NIEL scaling hypothesis*, ROSE/TN/2000-02, June 2000

[42] J. Lindhard et al; Mat. Fys. Medd. Dan. Vid Selsk 33 (1963) Number 14

[43] A. Ferrari *Radiation calculation for the* ATLAS*Detector and Experimental Hall*, CERN-EST/96-01 (LEA), February 1996

[44] P. Aurenche et al., Comp. Phys. Commun. 83 (1994) 107.

[45] Y. Baconnier, G. Brianti, P. Lebrun, A.G. Mathewson, R. Perin, LHC *: the Large Hadron Collider accelerator project*, CERN, Geneva LHC Study Group 1993

[46] A.R. Weidberg *Expected Fluences*, SCT-links talk, SCT-week May 1997

[47] R. Ramaswami, K.N. Sivarajan, *Optical Networks – A Practical Perspective*, Morgan Kaufman Publishers, Inc. San Francisco, 1998

[48] G. Mahout, J.D. Dowell, A.R. Weidberg, R. Wastie, R.J. Homer, R.B. Nickerson, I.M. Gregor, *Radiation Hardness and Lifetime of VCSELs and PIN photodiodes for use in the* Atlas *SCT*, Proc. SPIE Vol.4134, p. 206-213, Photonics for Space Environments

[49] DG Charlton et al., *Radiation Hard Optical Links for the* Atlas *SCT and Pixel Detectors*, 5th workshop on electronics for Lhc experiment, Snowmass Colorado, september 20-24, 1999 p.185

[50] J.D. Dowell et al, *Irradiation Tests of Photodiodes for the* Atlas *SCT Readout*, Atlas Internal Note, INDET-99-200, February 1998

[51] D.G. Charlton et al, *Radiation Hardness and Lifetime Studies of Photodiodes for the Optical Readout of the* Atlas *Semiconductor Tracker*, Atlas Internal Note, INDET-99-022, November 1999

[52] A. Kootz, *Lebensdauertests an bestrahlten VCSELn fur den* Atlas *Pixel Detektor*, Diploma Thesis, WU-D-18 December 1999

[53] B.H. Rose et al, *Proton damage effects on light emitting diodes*, J.Appl.Phys. 53(3) March 1982

[54] Laboratorium für Hochenergiephysik, Universität Bern, *Studies for the Inner Detector of the* Atlas *Experiment at the Large Hadron Collider*, Dissertation von J. Beringer, (1996)

[55] T.E. Sale, *Vertical Cavitiy Surfaces Emitting Lasers*, John Wiley and Sons Inc., New York 1995]

[56] K.J. Ebeling et al., *Efficient Vertical Cavity Surface Emitting Laser Diodes for High Bit Rate Optical Data Transmission*, Int. J. Electron. Commun. 100 (1996) No. 9, 1-11

[57] J. Beringer et al, *Radiation hardness and lifetime tests of irradiated LEDs and VCSELs*, NIM A435(1999) 375.

[58] T. Wipienski et al., *VCSELs for datacom applications*, Osram Semiconductors,

[59] P. V. Mena, J. J. Morikuni, S.-M. Kang, A. V. Harton, and K. W. Wyatt, *A Simple Rate-Equation-Based Thermal VCSEL Model*, J. of Lightwave Technology, Vol. 17, No. 5, May 1999 p. 865

[60] H. Henschel et al., *Optical Fibres for High Radiation Environments*, IEEE Transactions on Nuclear Science Vol.41, No.3, June 1994

[61] K. Tsunemi et al., *Radiation Resistance Characteristics of Optical Fibres*, Fujikura Techniacal Review 1995,

[62] K. Gill et al., *Gamma and Neutron Radiation Damage Studies of Optical Fibres*, CERN-ECP/96-13, October 1996

[63] D.G. Charlton et al., *Irradiation Studies of Multimode Optical Fibres for use in ATLAS front-end links*, Nucl. Instr. Meth. A446 (2000)

[64] Private communication with Keith Wanser, California State University, Fullerton, USA

[65] J. Beringer et al, *Radiation Hardness and Life Time Studies of LEDs and VCSELs for the Optical Readout of the* Atlas *SCT*, Atlas Internal Note, INDET No-183, September 1997

[66] B.H. Rose, C.E. Barnes, *Proton damage effects on light emitting diodes*, J.Appl.Phys.53(3), March 1982

[67] R.W. Herrick et al., *Analysis of VCSEL degradation modes*, SPIE Vol.2683 p.123

[68] R.A. Morgan et al., *Vertical–cavity surface–emitting lasers come of age*, SPIE Vol.2683 p.18

[69] P.M. Petroff, *Physics and material issues behind lifetime problem in semiconductor lasers and light emitting diodes*, SPIE Vol.2683 p.52

[70] P.K. Teng *Gamma Irradiation of Truelight* Vcsels report available at `http://hepmail.phys.sinica.edu.tw/ atlas/radiation.html`

[71] B. Hawthorne *Honeywell Optoelectronics Reliability Study, 850nm VCSEL Products*, (1997)

[72] MIL-STD-883B *Test Methods and Procedure for Microelectronics*

[73] MITEL Semiconductor *Introduction to VCSELs*, J. Jönsson, J. Isaksson, Presentation at the Second Workshop in Optical Readout Technologies for ATLAS (1999).

[74] N. Wermes, I.M. Gregor, Pixel Opto-Package Design Review, ATL-IP-ET-0001v.1, February 2001

[75] I.M. Gregor, M. Pearce, J.D. Dowell, P. Jovanovich, A. Kootz, G. Mahout, I. Mandic, A.R. Weidberg, *VCSEL-based Custom Radiation Tolerant Optical Data Links*, Proceedings of the Photonics West 2000 Conference, Jan. 2000, San-Jose, USA

[76] D.G. Charlton, J.D. Dowell, R.J. Homer, G. Mahout, P. Jovanovic, R.L. Wastie, A.R. Weidberg, S. Galagedera, M.C. Morrissey, J.K. Troska, D.J. White, A. Rudge, I.M. Gregor, M.L. Chu, S.C. Lee, P.K. Teng, *Radiation Hard Optical Links for the* Atlas Sct *and Pixel Detector*, presented at LEB2000 in Cracow

[77] K.K. Gan *A Novel Optical Package for the* Atlas *Pixel Detector*, International Journal of Physics A, DPF2000

[78] I.M. Gregor et al, *Optical Data Links for the* Atlas Sct *and Pixel Detector* Proc. Pixel 2000, Genua, Italy NIM A 465 (2001) 131-134

[79] D.J. White, J.D. Dowell, G. Mahout, P. Jovanovic, I. Mandic, A.R. Weidberg, *Radiation Hardness Studies of the Front-end ASICs of the Optical Links of the* Atlas *SemiConductor Tracker*, NIM A 456 (2000) 292

[80] private communication with Jens Wüstenfeld, Dortmund University

[81] W. Wagner, *Untersuchungen zur optischen Datenubertragung des* Atlas-*Pixeldetektors*, WU-D-2001-2 Diploma Thesis January 2001

[82] K.E. Arms et al.,*Radiation-hard ASICs for optical data transmission in the* Atlas *Pixel detector*, accepted for presentation at the Seventh Workshop on Electronics for LHC Experiments, Stockholm, September 2001

[83] D.J. White, *VDC - Project Specification*, Rutherford Appleton Laboratories, RAL 22 V 1.00

[84] private communication with K.E. Arms, Ohio State University, USA

[85] D.J. White, *DORIC4 - Project Specification*, Rutherford Appleton Laboratories, RAL 220 V 1.02

[86] J. Troska, J.D. Dowell, I.M. Gregor, R.J. Homer, P. Jovanovich, G. Mahout, I. Mandic, R. Wastie, A.R. Weidberg, D.J. White, *Radiation-hard Optoelectronic Data Readout for the* Atlas Sct, Proc. SPIE Vol.4134, p. 214-221, Photonics for Space Environments

[87] University of Oxford, *Biphase Mark Encodernand VCSEL Drive Control BPM* Project Specification, NP–ATL–ROD–BIP HASE–001–PRSV2.00

[88] D.J. White, *Data Receiver Integrated Circuit DRX*, Project Specification, Rutherford Appleton Laboratories RAL 232 DRX12 V 1.03

[89] M. OBryan et a., *Single Event Effect And Radiation Damage Results For Candidate Spacecraft Electronics*, presented at IEEE NSREC 98.

[90] A. Kenneth, *SEDS MIL-STD-1773 Fiber Optic Data Bus: Proton Irradiation Test Results and Spaceflight SEU Data*, IEEE Transaction on Nuclear Sience, Vol. 40, No.6, December 1993

[91] K. Gill et al., *Aging test of optoelectronic components for the* Cms *Tracker optical links* Cern, High Energy Physics - Imperial College London,(1998)

[92] P.W Marshall et al., *System Level Radiation Response of a High Performance Fiber Optic Data Bus*, IEEE Transaction on Nuclear Sience, Vol. 43, No.3, June 1996

[93] P.W. Marshall et al., *Space Radiation Effects in High Performance Fiber Optic Datat Links for Satellite Data Management*, IEEE Transaction on Nuclear Sience, Vol. 43, No.2, April 1996

[94] J.D. Dowell, R.J. Homer, G. Mahout, P. Jovanovic, I.M. Gregor, R.L. Wastie, A.R. Weidberg, J.K. Troska, D.J. White, *Single Event Upset Studies with the Optical Links of the* ATLAS *SemiConductor Tracker*, submitted to NIM

[95] B.J. Dropesky et al., *Excitations functions for the production of ^{18}F and ^{24}Na from Al and Si with fast pions*, Phys. Rev. C 32 (1985) 1305

[96] F. Faccio et al., *SEU tests of an 80Mbit/s Optical Receiver for the CMS Tracker Digital Optical Link*, preprint

[97] M. Huhtinen, F. Faccio, *Computational method to estimate Single Event Upset rates in an accelerator environment*, preprint submitted to NIM, October 1999

[98] M.L. Andrieux et al., *Single Event Upsets of a High Speed Digital Optical Data Link*, Preprint submitted to Elsevier Preprint

[99] Private communication with A.R. Weidberg, University of Oxford, UK

[100] P.W. Marshall et al., *Particle Induced Bit Errors in High Performance Fibre Optic Data Links for Satellite Data Management*, IEEE Transaction on Nuclear Sience, Vol. 41, No.6, December 1994

[101] Information on the PSI ring cyclotron is available on WWW at url: www1.psi.ch/WWW.gfs_ hn/abe.ringcycl.html

[102] `http://www.psi.ch/ltp/ltpprop.html`

[103] B. Dinkespiler et al., *Neutron Irradiation of Optical Link Components*, ATLAS Internal Note, LARG No-002, December 1994

[104] M. Dentan *Radiation Effects on Elctronics Components and Circuit*, CERN, ATLAS

List of Figures

List of Tables

Glossary

ASICs Application specific ICs.

ATLAS A Toroidal LHC Apparatus

Attenuation The optical power loss per unit of fibre length caused by adsorption and scattering. Expressed in decibels per kilometre (dB/km) or decibels per meter (dB/m).

B-Layer Innermost Layer of the ATLAS Pixel Detector.

BCB Benzocyclobutene; dielectric material used for the MCM-D technology.

Bend Radius The radius taken by the axis of the fibre cable when it is bent. A minimum bend radius is the minimum radius to which a fibre cable can be bent without exceeding maximum stress in its fibre.

BERT Bit error rate tester.

Bi-Phase Code A transmission code in which each bit interval begins with either a low-to-high or a high-to-lowlevel transition. If the data bit to be encoded is a logical 1 then another transition must occur before the end of the bit interval. If the data bit is a 0 there is no transition until the beginning of the next bit interval.

Bit Error Rate (BER) In an actual transmission system, various electronic noise sources can change or corrupt the stream of data bits. The number of these corrupted bits divided by the total number of received bits within an arbitrary time period is the bit error rate (BER). The lower the BER value, the fewer the number of errors in the transmission.

BPM BiPhase Mark Encode: chip which encodes the control data and 40 MHz clock to one waveform, drivong the off-detector VCSELs

CERN Conseil Europeénne Pour la Recherche Nucleaire; European Organisation for Nuclear Research in Geneva, Switzerland

Cladding Silica or plastic that surrounds the core of an optical fibre to minimise surface scattering losses and establish the NA (Numerical Aperture) for Total Internal Reflection to occur.

CMS The Compact Muon Solenoid; Experiment at LHC.

DBR Distributed Bragg Reflector; layer structure within a VCSEL serving as a mirror.

Dispersion The increase in rise/fall time of the optical signal at the far end of long fibreoptic cables. It is expressed in nanoseconds per kilometre. Dispersion is linearly related to the inverse of the bandwidth-times-length constant. It results from either modal or material effects.

DMILL Durcie Mixte sur Isolant Logico-Lineaire, radiation tolerant process

Doping Adding impurities to a substance to change its electrical properties.

DORIC Digital optical receiver IC: receiver chip which decodes the BiPhase Mark encoded Control data and 40 MHz clock

DRx Driver Receiver IC: receiver chip an the off-detector side

DSM Deep submicron; radiation tolerant 0.25 μm process

DTUJET A Monte Carlo Program for hadronic multi-paxticle production.

Duty Cycle The ratio of an time to off time in repetitive operation, generally expressed as the an percentage of total cycle time.

Fall Time On the trailing edge of a pulse, the time it takes for the instantaneous power to decrease from 90 percent of the peak pulse power level to 10 percent of the peak pulse power level.

Fluence Particels per cm² weighted with a particle- and material specific factor and integrated over a certain time, e.g 10 years LHC.

FLUKA Particle transport code.

Flux Number of particles per second and and square cm

GaAs Gallium-Arsenide, III-V semiconductor

Graded-Index Fiber An optical fibre whose index of refraction decreases as a function of the distance from the centner of the core, until it reaches the cladding index of refraction at the core radius. Graded-index fibres offer multi-mode (large NA) characteristics along with low dispersion and are used in all fibre applications. It is one of the two most popular fibres, the other being Step-Index Fibres.

Index of Refraction (n) The ratio of the velocity of light in a vacuum (such as the fibre core, n, or cladding, n) to the velocity of light in a given medium.

Index Profile The index of refraction through the fibre core as a function of the distance from the centre of the core. A sharp reduction of the index at the boundary between core and cladding results in a step-index fibre. A gradual lowering of the index in the core areas approaching the cladding results in a graded-index fibre.

Infrared (IR) Wavelengths that extend beyond 770 nanometres.

ERMA Kinetic energy in matter.

LHC Large Hadron Collider.

LI-curve Luminosity versus drive current.

LVDS Low Voltage Differential Signal.

LVL1 Level 1 trigger.

MCC Module Controller Chip coordinates the transfer to and from the 16 front-end chips an a Pixel module.

MCM-D Multi chip Module - Deposited; module concept which incorporates the signal and power busses of one module between front-end chips and sensor.

MIP Minimal ionising particle.

MOCVD Metal-Organic Chemical Vapor Deposition; process for growing VCSELs.

Modal Dispersion The expansion of the rise and fall times of the signal as it travels along the fibre, expressed in ns/km. The time of arrival of simultaneously transmitted flux (optical radiation) depends an the path length travelled. Since reflections of the flux rays occur at different angles, path lengths will vary, causing dispersion. Also referred to as spreading. Modal dispersion is greatly reduced by use of fully graded fibre and reduced to zero in single-mode fibre.

Modes of Propagation Optical rays may propagate at various angles with respect to the fibre axis. The smaller angles are called low-order modes and the larger angles are called high-order modes. Both classes of modes are totally reflected within the core.

MOS metal-oxide-semiconductor; process for growing ICs

MSSM Minimal Supersymmetric Standard Model.

MT12 Standard fibre connector housing 12 fibres.

Multi-mode Fibers Single firers that can accommodate both high-order and low-order propagation modes. Such fibres have large NA.

NIEL Non ionising energy loss - the total energy loss due to non-ionising interactions.

Non-Return-to-Zero (NRZ) A transmission code or data format in which the signal level does not periodically return to zero between a succession of high or 1 bits. A clock signal at the receiving end is required to define the point at which each bit of data is valid. A separate channel is required to transmit the clock signal.

Numerical Aperture (NA) A number that expresses the angular light-gathering characteristic of an optical fibre. It is expressed by the sine of the acceptance angle, the maximum angle with respect to the fibre axis at which an entering ray will experience total internal reflection (TIR).

OSU The Ohio State University

PCB Printed circuit board.

Pigtail Kapton structure for the electrical connection of the module and the optical link.

PiN Photodiode In this semiconductor type, the p-doped and n-doped regions are separated by a lightly doped intrinsic region in which the absorbed photons generate an electric current. Hence the acronym PiN. PiNs have the advantage of broad spectral response, wide dynamic range, high speed and low noise, but no internal gain.

PPO Patch panel 0 at the end of the pixel barrel close to the outer radius.

PSI Paul Scherrer Institut, Brugg, Switzerland.

Responsivity The measure of a photo-detector's performance. The unit of measure is signal current divided by optical power, A/W.

ROD Read Out Driver: contains the primary functions for the readout and control of the SCT/Pixel subsystem and interfaces with the ATLAS-wide systems. It is positioned in 100 m distance from the Pixel Detector.

SCT SemiConductor Tracker; Semiconductor Strip Detector in the ATLASDetector surrounding the Pixel Detector

SEE Single event effect.

SEU Single event upset.

SM Standard Model.

Step-Index Fibers Fibres whose index of refraction is reduced sharply at the boundary between the core and the cladding. They are useful for multi-mode operation over short distances up to one kilometre.

TRT Transition Radiation Tracker - outer detector of the ATLAS Inner Detector.

TTC Timing, Triggering and Control

VCSEL Vertical Cavity Surface Emitting Laser

VDC on-detector VCSEL Driver Chip

Acknowledgements

I am indebted to a number of important contributors, some of whom are detailed below. First, I want to thank Tony Weidberg. He was of invaluable help during the last years in finding weak points in the described system and giving impulses how to solve these ... and keeping the sense of humor alive while problems appeared.

If there are two persons I must thank most, these are Professor Karl-Heinz Becks and Professor Jürgen Drees. I would like to thank them for their continuous and unrelenting support during all phases of this research project.

I also feel grateful to all my colleagues within the collaborations I participated (ATLAS Pixel Detector and SCT) and my dear colleagues in the high energy physics group in Wuppertal.

To my family go special thanks for bearing with me and not disturbing me during the long hours in front of the computer. Especially, I would like to thank my spouse Marshall for waiting for me to come back from the many, many trips abroad. To my family, Thank you very much !!!

I am sure I am forgetting someone here... Sorry. I am certain they know I am grateful to them too ... :-)